Flexibility and Sensitivity Enhancement in Optical Electric-Field Sensor with Bulk Electro-Optic Crystal

Graduate School of Systems and Information Engineering

University of Tsukuba

March 2010

Hiroyoshi Togo

Summary

In the 1980s, ultrashort-pulse lasers, of which the mode-locked laser is a common example, became available for laboratory use. Since then, Optical electric-field sensors based on bulk electro-optic (EO) crystal have attracted much attention for electric-field measurement because of their extremely large detectable bandwidth (ranging from DC to terahertz) and small invasiveness of electric fields. Electric-field measurement above a planar resonator and a microstrip patch antenna has been demonstrated by using an external probing technique, in which a free-space-propagating beam was focused into a miniature EO crystal. The demonstration showed that EO-based near-field mapping in amplitude and phase is a powerful tool for the analysis and design of microwave-radiating structures. One drawback, however, was that the free-space optics for controlling and the polarization of the light wave was mounted on an optical table and a bread board, which meant that only points on the table and board were accessible to the sensor. To expand the accessibility, the free-space optics was integrated into a hand-held cylindrical probe. The probe proved to be useful for the non-contact measurement of free-space electric fields in, for example, electromagnetic compatibility (EMC) and electromagnetic interference (EMI) applications, but the cylinder and the internal optics would disturb the near field of a device under test (DUT). To minimize disturbance and make it easy to position the sensor tip over any point to be probed, an optical fiber was connected to an EO-based electric-field measurement system, and the first near-field mapping was demonstrated by using a fiber-mounted sensor fixed on the x-y stage of a microscope. Afterward, near-field mapping over a microstrip line and antenna with the fiber-mounted sensor was used for diagnoses of monolithic microwave integrated circuits (MMIC) and evaluations of electromagnetic interference. Since the EO crystal was mounted on the edge of an optical fiber, the fiber-mounted sensor made it possible to map the electric field in an enclosed miniature structure with negligibly small invasiveness. In the conventional fiber-mounted sensor, the DUT was moved or the sensor was scanned in a small area over a portion of the DUT to stabilize the polarization of the light wave propagating in the fiber. Unfortunately, in practical EMC and EMI applications, the DUT cannot be moved and the scanning area is several times the size of the DUT.

In response to this situation, this dissertation mainly deals with the fiber-mounted optical electric-field sensor to be flexibly scanned in the whole area required for characterizing and designing devices and antennas. Coherent optical fiber communications technologies have matured and transferred into optical sensor applications. The passive polarization compensation techniques developed in coherent optical fiber communications is spontaneously conducted into the fiber-mounted sensor. The passive polarization compensation technique enables the fiber-mounted sensor to flexibly bend until the bending radius is smaller than 3 mm with a

sensitivity change of less than 1 dB. Moreover, this technique does not affect other properties, such as dynamic range, detectable directivity, and frequency response characteristics.

Another major issue addressed in this dissertation is the sensitivity enhancement of the fiber-mounted sensor. The main application of the fiber-mounted sensor is specific absorption rate (SAR) measurement of mobile phones, which is a kind of EMC test. The fiber-mounted sensor has been practically used in the SAR measurement for the second generation (2G) of mobile telecommunications. Recently, technologies have been phasing into third generation (3G) of telecommunications, which has an occupied bandwidth 30 dB wider than that for 2G. In frequency-domain measurements, since the resolution bandwidth is inversely proportional to the signal-to-ratio (SNR) and frequency sweeping time, the SAR measurement for a 3G mobile phone takes 1000 times as long as that for a 2G one. To reduce measurement cost, the resolution bandwidth has to be increased; that is, the detection sensitivity of the electric-field sensor must be enhanced 30 dB or more.

A promising material for improving the detection sensitivity of the fiber-mounted sensor is 4-dimethylamino-N-methylstilbazolium tosylate (DAST) because of its large electrical contribution to the EO effects and low dielectric constant. Recently, the growth of large-aperture DAST crystal has been achieved with high quality and reproducibility. DAST crystal has been formed to a size of one cubic millimeter, which is as small as the CdTe crystal conventionally mounted on the fiber-mounted sensor. The fiber-mounted sensor with DAST crystal offers a sensitivity 6 dB higher than that with CdTe crystal without affecting other properties such a directivity and stability in practical use. Moreover, DAST is a good insulator, which makes it promising for electric-field detection in the extremely low frequency (ELF) band, where the CdTe crystal cannot detect electric field.

In this dissertation, I describe the configurations and the basic properties of the flexible fiber-mounted sensor based on the passive polarization compensation technique and a highly sensitive fiber-mounted sensor with the DAST crystal. I also demonstrate applications of the flexible and highly sensitive fiber-mounted sensor to electric-field measurements are demonstrated. The flexible sensor is applied to near-field measurements, which strictly require less invasiveness into electric fields and sensor-sensitivity stability, and accomplishes the two-dimensional measurement with three-axis electric-field components, which agrees well with simulations. Moreover, in an SAR measurement for a mobile phone, the highly sensitive sensor achieves higher performance than the CdTe-based sensor. The highly sensitive sensor also has potential for practical use in EMC measurements in the ELF band, where the CdTe-based sensor cannot detect any electric field.

Table of contents

Chapter 1

Introduction

1.1 Background

1.1.1 Application of radio waves

In 1888, Heinrich Rudolf Hertz, a German physicist, who clarified and expanded the electromagnetic theory of light that had been put forth by James Clerk Maxwell, a Scottish theoretical physicist and mathematician, in 1864, satisfactorily demonstrated the existence of electromagnetic waves by building an apparatus to produce and detect very high-frequency (VHF: 30 – 300 MHz) or ultrahigh-frequency (UHF: 300 M – 3 GHz) radio waves. In 1895, Marchese Guglielmo Marconi, an Italian inventor, best known for developing radiotelegraph systems, successfully transmitted signals outdoors over a distance of approximately 1.5 km as shown in Fig. 1-1, and in 1901, transmitted signals completely across the Atlantic Ocean from Poldhu, Cornwall of England in the United Kingdom to Signal Hill in St. John's, Newfoundland (now part of Canada) using a 152.4-m kite-supported antenna at approximately 300 kHz. In those days, radio waves were used only for radiotelegraphs or for radio communications between ships and harbors. Over time, audio (sound) broadcasting service expanded into our everyday life. Today, radio waves are widely used in various applications, including broadcast television, mobile telecommunications, wireless local area networks (LANs), remote sensors, radars, spectroscopy for machine control and security, and bioengineering as shown in Fig. 1-2 [1-1].

Fig. 1-1. Marconi and associations raising a kite-supported antenna at St. John’s in 1901.

The millimeter and terahertz radio-frequency (RF) bands, which had been difficult to generate and detect until a few decades ago and so remained undeveloped, have now become intimately linked to technological innovation. The 60- and 76-GHz bands are used for license-free commercial broadband, in-home wireless transmission for high-definition TV and other data, and vehicle radar for automobiles [1.2]-[1.4]. NTT Microsystem Integration Laboratories has used 76-GHz band signals to detect cracks in concrete surfaces covered with wallpaper or paint [1.5], [1.6]. They are also aiming at the practical development of the millimeter and terahertz RF bands with a 10-Gbps fixed wireless access (FWA) system that uses the 120-GHz band [1.7]-[1.9]. Radio-frequency resources are both limited by law and scarce, so developing the millimeter and terahertz radio frequency bands in this should open the way to new applications. For effective use of radio waves, it is important to understand their propagation and radiation characteristics in practical use. Characterization of radio waves requires accurate measurement of the antenna, which is the interface between the radio signal and the circuitry.

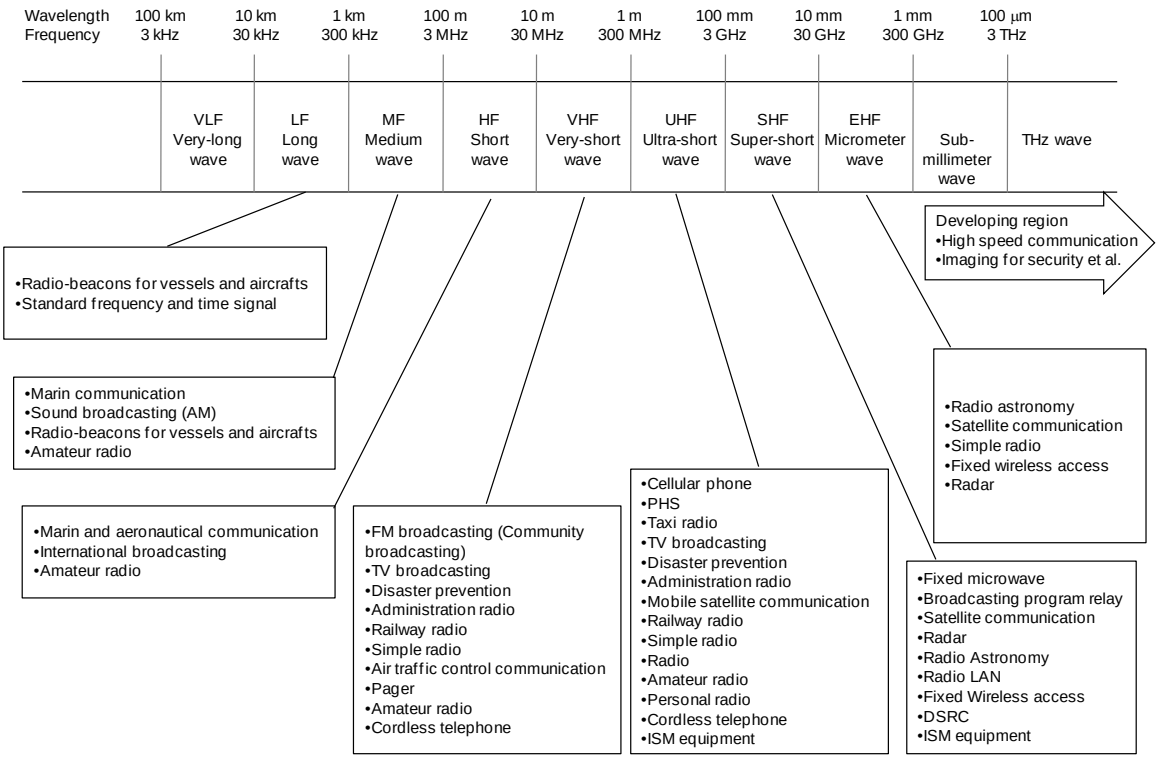

Fig. 1-2. Principal uses of radio waves in Japan.

1.1.2 Antenna measurement

An antenna is generally characterized in terms of input impedance, directionality, and gain. When measuring any of those characteristics, accuracy is decreased by external sources of radio waves and waves scattered by surrounding structures. The ideal situation, then, is to perform the measurements in a free space where there are no external radio waves or in an electromagnetic shield room. At the same time, the electric-field sensor for detecting the signal from the antenna should not affect that signal. Currently, a standard dipole antenna {Fig. 1-3(a)} or a horn antenna is used as the electric-field sensor, and electrical cable carries the detected signal to the measurement instrument. The electric-field sensor and the electrical cable are made of metal and therefore scatter the signal emitted by the antenna being measured, which may make it impossible to know the original state of the signal. In particular, if the electric-field sensor is placed near the antenna under test (AUT), electrical coupling occurs and radio waves other than the free-space propagating signal arise. An ideal measurement setup requires the use of an electric-field sensor that does not contain metal and an optical fiber lead-out [Fig. 1-3(b)] for accurate measurement of the radio signal.

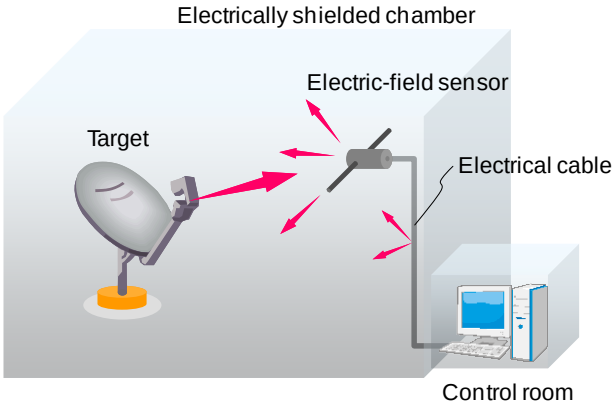

(a)

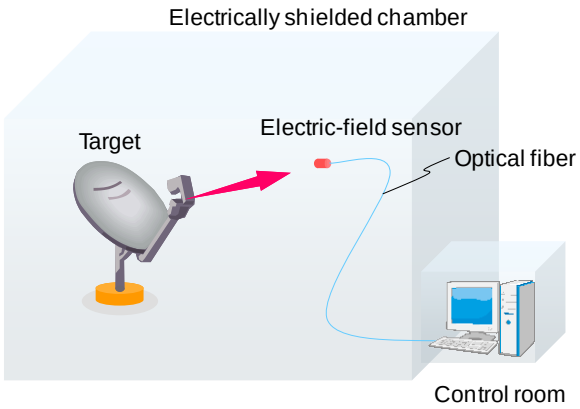

(b)

Fig. 1-3. Conventional (a) and proposed antenna measurement system (b)

In mobile telecommunications, the specific absorption rate (SAR) is the primary dosimetric parameter of RF energy absorbed by the human body and is determined from the electric-field distribution in the human body. For mobile phones, since the SAR has to be less than the lower limit stipulated in the guidelines for human exposure to electromagnetic fields [1.10]-[1.12], measuring the electric-field distribution in a tissue-equivalent phantom (TEP) is a very important process in the development of antenna in a complete handset with circuit boards, a battery, a camera, and other components. . In the SAR measurement, a small dipole antenna connected with a diode into an electric instrument using a high-impedance electrode has been standardized for use in measuring the electric-field distribution in the TEP near a handset as shown in Fig. 1-4 [1.13].

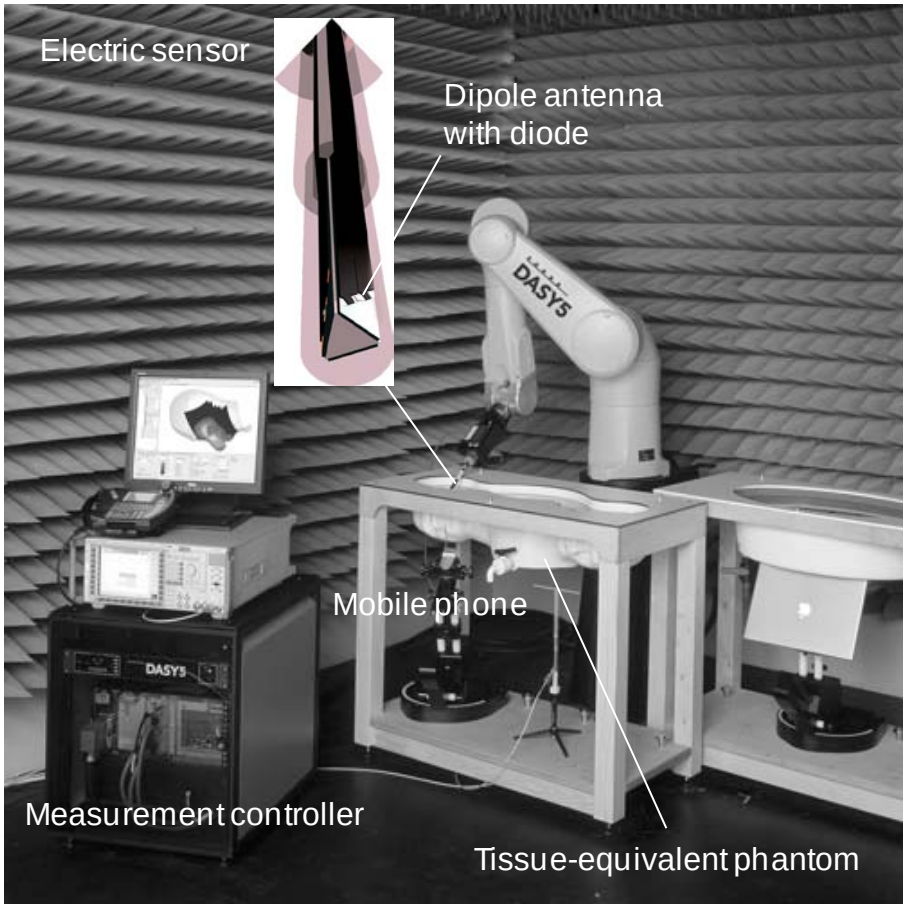

Fig. 1-4. Setup of commercially available SAR measurement system with dipole antenna.

1.2 Electric-field measurement with photonics

The antenna is one of the most important parts of systems that use microwave and millimeter-wave electromagnetic fields for wireless communications, sensing, or processing because its characteristics greatly influence system performance. Therefore, for wireless system development it is very important to establish a method that enables us to precisely characterize antennas. Antenna characterization is performed in various ranges under various circumstances (Table 1-1). In far-field ranges, the characteristics are directly obtained from measured data. However, these ranges require a huge measurement environment in order to avoid electric-field disturbances due to reflections from objects other than the AUT. In near-field ranges, measurements are performed in an anechoic chamber and the data is converted to far-field characteristics by numerical calculation.

In a near-field measurement, it is common to scan the AUT with a metallic sensor, such as a horn antenna, a dipole antenna, or the edge of a waveguide [1.14]-[1.16]. However, errors are caused by electric field disturbances due to reflection from the probe and by electrical coupling between the probe and AUT. To solve this problem, photonics-based electric-field sensors have been proposed [1.17], [1.18]. In those sensors, a Mach-Zehnder interferometer (MZI) is formed with a waveguide on a $LiNbO_3$ (LN) substrate and a small dipole antenna is fabricated above one of the branches of the MZI as shown in Fig. 1-5. The electric field detected at the dipole antenna is converted to an optical-intensity-modulated signal and transmitted to a receiver through an optical fiber. Therefore, waveguide-based electric-field sensors are less invasive than the conventional metallic ones. However, at frequencies in the gigahertz region, the invasiveness of the dipole antenna may not be negligible. To reduce it by removing the dipole antenna, the birefringence in a bulk electro-optic (EO) crystal was used, which was proportional to applied electric-field intensity, which is called the Pockels effect, or the Pockels EO effect. The applied electric field is converted to intensity-modulated signal with an analyzer connected to an output port as shown in Fig. 1-6. There are no metal components in the sensor tip. To make the bulk-EO-based sensor accessible near the AUT, I developed a pen-shaped optical electric-field sensor based on a bulk EO crystal has been developed [1.19]. The bulk EO crystal is fixed on the tip of the pen-shaped cylinder housing the optical components. An input light is reflected on the dielectric mirror coated on the EO crystal and then returned to the optical instruments through an input path. This sensor has flat sensitivity from several megahertz to several hundred gigahertz. However, invasiveness due to reflection from the cylinder and the optical components in the cylinder still affected measurement accuracy. To solve this problem, the EO crystal was connected to the optical components with an optical fiber fixed inside of a 20-cm-long glass tube as shown in Fig. 1-7 [1.21]-[1.24]. In 2005, Onishi et

al. demonstrated that this bulk-EO-based optical electric-field sensor measured electric-field distribution in a TEP more accurately than the commercially available sensor with a small dipole antenna [1-20], and reported the feasibility of constructing a high-speed SAR measurement system by combining the electric-field measurement system with eight arrayed sensors connected to an optical switch and an algorithm that calculates from two- to three-dimensional electric-field distribution [1-25].

Table 1-1. Characteristics of antenna-measurement methods.

Range type	**Site type**	**Description**	**Advantages**	**Disadvantages**
Far-field	Open	・ Source and test antenna are placed on tower, building, hills, etc. ・ Either the source or test antenna is elevated.	Low cost	・ Requires real estate. ・ May require towers. ・ Weather.
	Inside anechoic chamber	A room is lined with absorber material to suppress reflections.	Indoors	・ Absorber and large room are costly.
Near-field	Inside anechoic chamber	The magnitude and phase of the near field of test antenna are sampled and the far field is computed.	Very small space	・ Accurate probe positioning is required. ・ Accurate amplitude and phase are required. ・ Time-consuming measurements. ・ Computer-intensive.

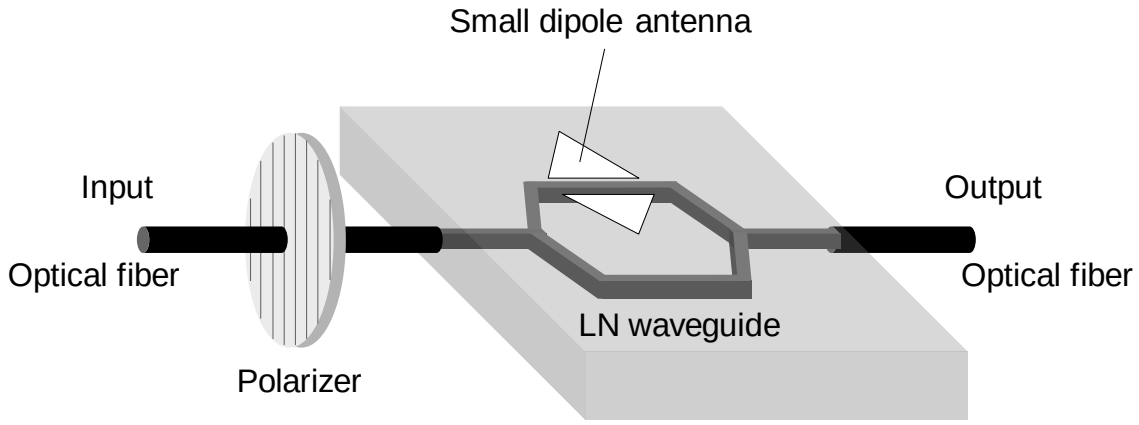

Fig. 1-5. Optical electric-field sensor based on MZI of LN waveguide.

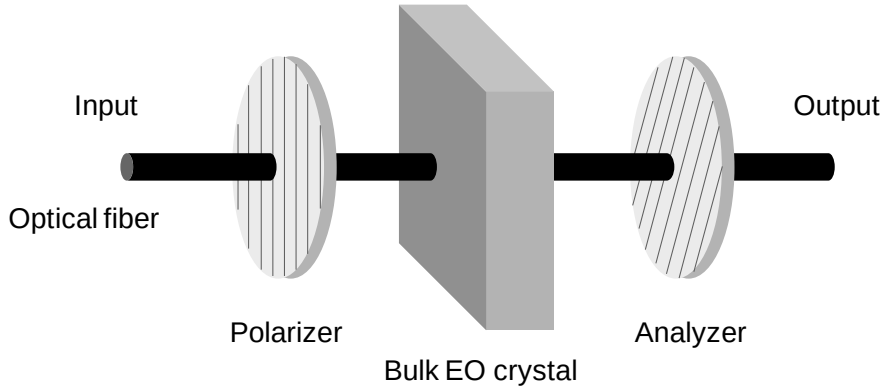

Fig. 1.6. Through-type optical electric-field sensor based on balk-EO crystal.

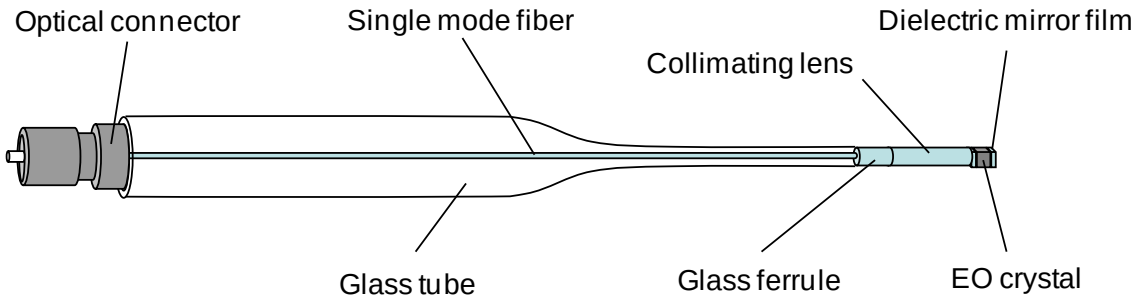

Fig. 1-7. Tip of reflection-type optical electric-field sensor based on bulk EO crystal mounted on optical fiber fixed inside of glass tube.

1.3 Issues in optical electric-field sensor with bulk EO crystal

1.3.1 Flexibility enhancement

Optical electric-field sensors based on bulk-EO crystal mounted on an optical fiber are used for characterizing antennas and circuits because of their small electro-magnetic invasiveness [1-26]-[1-30]. Since fiber-mounted sensors are free from disturbances created by metal components such cables and antennas around a detection area, the distribution of the near field radiated from a microstrip antenna and a line can be precisely measured. However, since the polarization plane of light transmitted through an optical fiber changes when the fiber is bent and because of temperature fluctuation, the sensitivity of the fiber-mounted sensor changes during long-term measurements with large scanning areas. In previous experiments, the AUT was scanned with the fiber-mounted sensor, and the scanning area was smaller than ten square millimeters even though the EO probe could be scanned over the antennas as shown in Fig. 1-8 (a). To stabilize the sensitivity, I have developed a fiber-mounted sensor where the optical fiber is fixed inside a thin glass tube. We scanned the developed sensor near a 2-GHz-band dipole antenna and precisely measured the electric-field distributions in an area larger than a twenty cubic centimeters, which is necessary if we are to evaluate the antenna. However, the length of the fixed optical fiber was only several ten centimeters as shown in Fig. 1-8 (b). In an ideal measurement as shown in Fig. 1-3 (b), high stability is needed for the electric-field sensor mounted on the tip of a flexible optical fiber with a length as long as several meters.

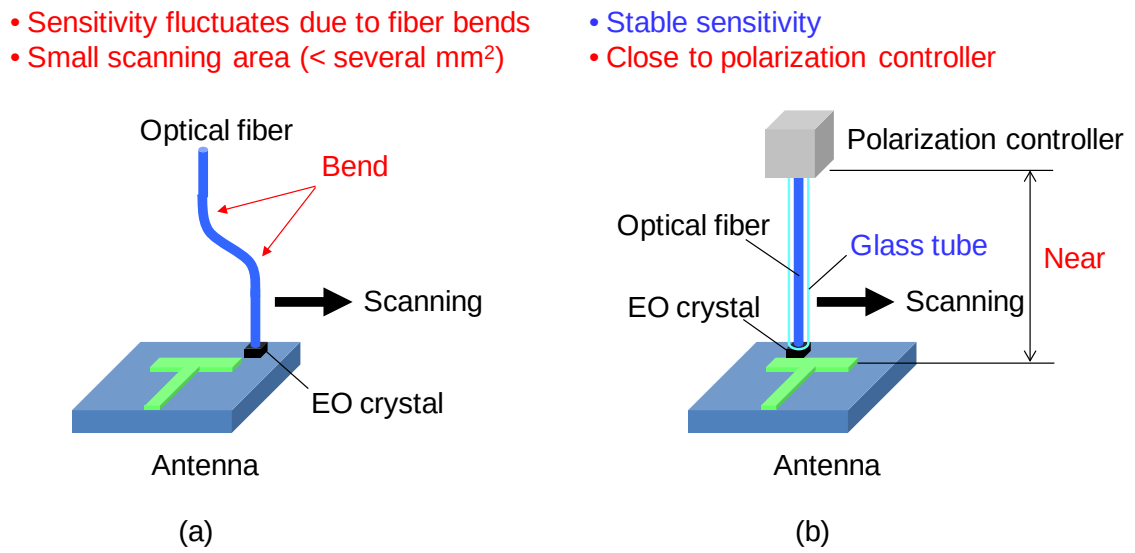

Fig. 1-8. Sensitivity-unstable sensor with flexible fiber (a) and less-flexible sensor with short fiber fixed in thin-glass tube (b).

1.3.2 Sensitivity enhancement

Optical electric-field sensors based on the EO effect have been attracting much interest in electromagnetic compatibility (EMC) testing because of their small electromagnetic invasiveness. Since a fiber-mounted sensor does not contain metal components, such as antenna and electrode, around a detecting area, the sensor is free from the disturbances created by them. This means that near-field distribution adjacent to radiation sources can be precisely measured. I have demonstrated the potential of the fiber-mounted sensor in SAR measurements using a TEP. In the demonstration, I used a fiber-mounted sensor with a CdTe crystal, which has the highest sensitivity coefficient among inorganic EO crystals. The sensitivity of the CdTe-based sensor is 40-dB lower than that of conventional metal sensors because the fiber-mounted sensor does not contain any metal that could apply and induce an electric field inside the crystal and because the electro-optic conversion coefficient based on the Pockels effect is very small. It takes several hours to map an electric-field distribution in the human head and full-body phantom for the SAR measurement due to the huge acquisition time for enhancing the output signal from a measurement system with the fiber-mounted sensor. Since the measuring time is reduced in inverse proportion to the detection sensitivity, a highly sensitive sensor is required in order to improve the throughput of the SAR measurement.

Moreover, sensitivity enhancement is required in the bulk-EO crystal based sensors for mobile telecommunications system. The standard was defined by the RCR (later became ARIB) in April 1991, and NTT DoCoMo launched its Digital mova service in March 1993. Like the Global System for Mobile communications (GSM), personal digital cellular (PDC) uses time division multiple access (TDMA), which is the second generation (2G) of telecommunications. PDC uses 25 kHz-wide carrier and is implemented in the 800-MHz (downlink 810-888 MHz; uplink 893-958 MHz) and 1.5-GHz (downlink 1477-1501 MHz; uplink 1429-1453 MHz) bands. After a peak of nearly 80 million subscribers to PDC, it had 46 million subscribers in December 2005, and is slowly being phased out in favor of third-generation (3G) technologies. In metropolitan areas, Freedom of Mobile Multimedia Access (FOMA) offered by NTT DoCoMo uses the Universal Mobile Telecommunications System (UMTS) band I around 2100 MHz with 5 MHz-wide radio channels. The occupied bandwidth for 3G mobile telecommunications is 30-dB wider than that for 2G telecommunications. Since, in frequency-domain measurement, the resolution bandwidth is inversely proportional to the signal-to-ratio (SNR) and frequency sweeping time, the SAR measurement for a 3G mobile phone takes 1000 times as long as that for a 2G phone. To reduce measurement cost, the resolution bandwidth has to be increased,; that is, the detection sensitivity of the electric-field sensor must be enhanced 30-dB or more as shown in Fig. 1-9.

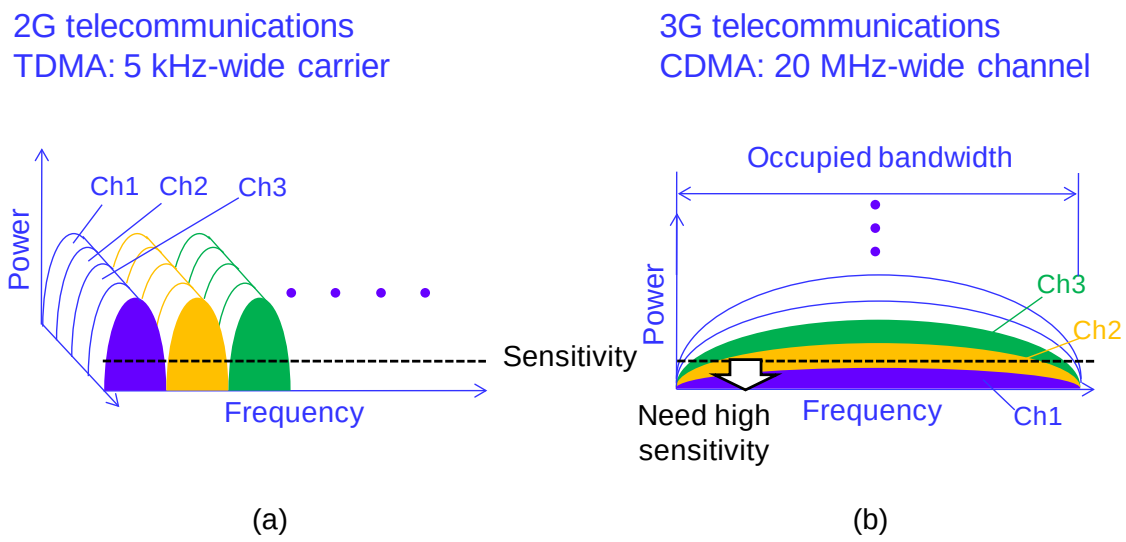

Fig. 1-9. (a) Occupied bandwidth of 2G with TDMA and (b) 3G mobile telecommunications system with CDMA.

1.4 Motivation and Objectives

The main purposes of this study are to develop (i) a flexibility enhancement method for accurately measuring electric field with less invasiveness and high accessibility of the sensor and (ii) a sensitivity enhancement method for adapting the sensor to the next generation of mobile telecommunications techniques. For the flexibility enhancement, a passive sensitivity stabilization scheme matured in an optical coherent communications is used to optically design the sensor in consideration of the polarization of light waves in the EO crystal, optical fibers, and other optical components. The scheme is theoretically and experimentally investigated in terms of its effects on the basic properties of sensitivity, directivity, and so on. For the sensitivity enhancement, organic crystal with a high EO coefficient is applied to the fiber-mounted sensor for the first time. Micro-fabrication techniques are developed for decreasing the insertion loss in the crystal and the orientation crystal is designed for optimizing the properties of sensitivity, stability, and directivity. The potential of the sensor is examined in practical SAR measurements and EMC tests in the extremely low frequency (ELF) band.

This dissertation mainly covers three topics: the flexible fiber-mounted sensor with the passive sensitivity stabilization scheme (chapters 3); the highly sensitive fiber-mounted sensor with the organic crystal (chapter 4), and practical uses of those sensors in near-field, SAR, and EMC measurement (chapter 5). The contents and organization of this dissertation are summarized as follows and outlined in Fig. 1-10.

Chapter 2 describes the features and the principles of electric field measurement with the EO effect and shows the configurations and basic properties of the developed handy-held sensor, where all free-space optics is integrated. It also covers the application of the sensor to millimeter-wave antenna measurements. Moreover, this chapter explains our fiber-mounted sensor developed in consideration of its use in practical applications and demonstrates the potential of near-field mapping around a dipole antenna in free space and electric-field mapping in an absorptive liquid used as the TEP to assess the SAR. Those demonstrations involve simultaneous mapping of amplitude and phase distribution, which has been impossible with a conventional probe.

Chapter 3 describes the theoretical mechanism of sensitivity fluctuation of the fiber-mounted sensor and the operating mechanism of the fiber-mounted sensor with the passive sensitivity stabilization method. It also explains how the developed fiber-mounted sensor with the CdTe crystal achieves stable sensitivity without degrading other basic properties of linearity, directivity, and so on.

Chapter 4 describes the theoretical mechanism of the electric-field detection with the organic crystal and the configuration of the fiber-mounted sensor with the organic crystal fabricated with specified techniques and presents the sensitivity enhancement in free-space electric-field detection.

Chapter 5 describes an application of the flexible and highly sensitive fiber-mounted sensor described in chapters 3 and 4 to electric-field measurements. The flexible sensor is applied to near-field measurements strictly require less invasiveness into the electric field and the sensitivity stability of the sensor and accomplishes the two-dimensional measurement with three-axis electric-field components, which agree wells with simulations. Moreover, this chapter shows that the highly sensitive sensor in achieves better performance in a SAR measurement for a mobile phone than the CdTe-based sensor. The highly sensitive sensor also has the potential for practical use in EMC measurements in the ELF band, where the CdTe-based sensor cannot detect any electric field.

Chapter 6 summarizes the results and important findings of this study.

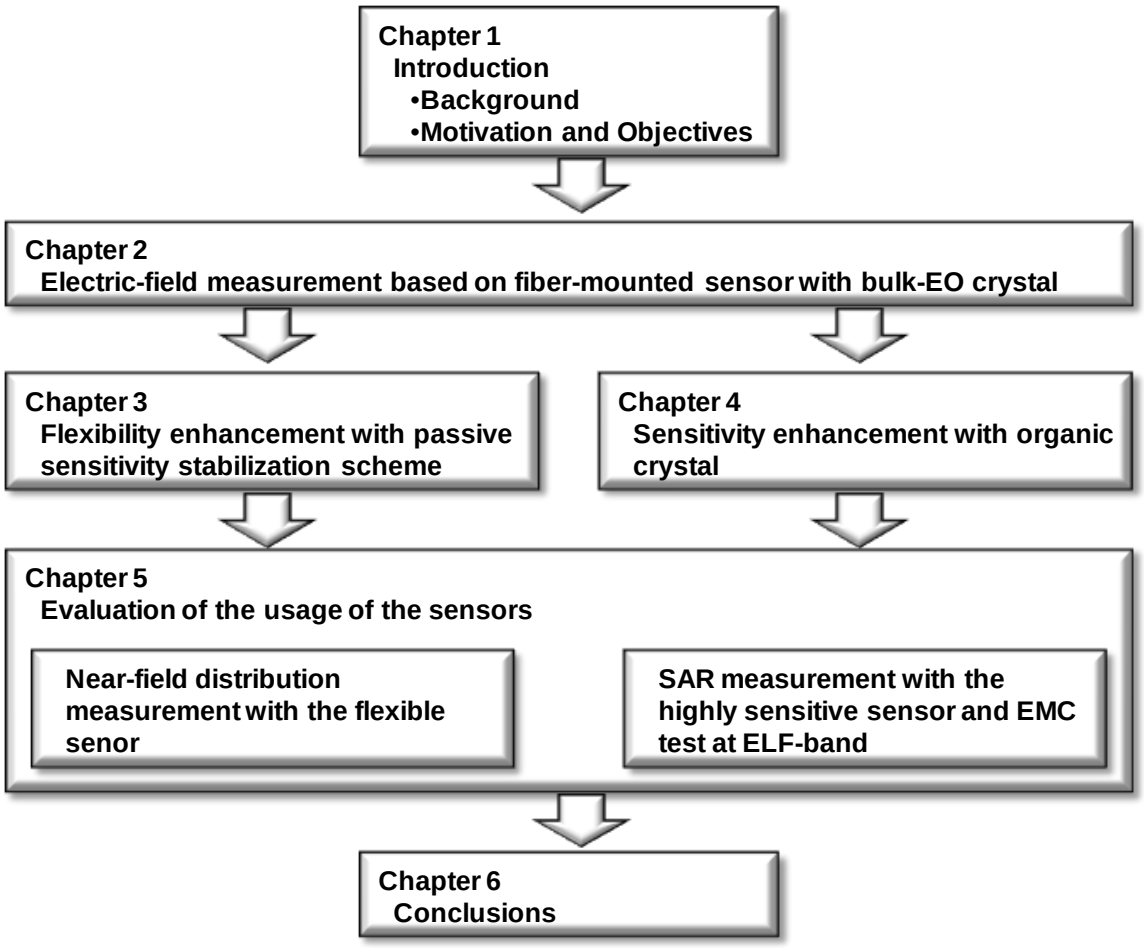

Fig. 1-10. Organization of the dissertation.

References

[1.1] The radio use web site of Ministry of Internal Affaires and Communication, http://www.tele.soumu.go.jp/e/adm/freq/search/myuse/summary/index.htm.

[1.2] M. Inoue, G. Wu, Y. Hase, A. Sugitani, E. Kawakami, S. Shimizu, and K. Tokuda, “An IP-over-Ethernet-based ultrahigh-speed wireless LAN prototype operating in the 60-GHz band,” IEICT Trans. Commun., vol. E83-B, no. 8, pp. 1720-1730, 2000.

[1.3] K. Ohata, K. Maruhashi, M. Ito, S. Kishimoto, K. Ikuina, T. Hashiguchi, N. Takahashi, and S. Iwanaga, Wireless 1.25Gb/s Transceiver Module at 60GHz-band, 2002 IEEE International Solid State Circuits Conference, 2002, pp. 298-299.

[1.4] http://www.adc.com/us/en/Library/Literature/104681AE.pdf

[1.5] S. Oka, H. Togo, N. Kukutsu, and T. Nagatsuma, "Latest trends in millimeter-wave imaging technology," Progress In Electromagnetics Research Letters, vol. 1, pp. 197-204, 2008.

[1.6] S. Oka, S. Mochizuki, H. Togo, and N. Kukutsu, “Inspection of Concrete Structures Using Millimeter-wave Imaging Technology,” NTT Technical Review, vol. 7, no. 3, pp. 1-6, 2009.

[1.7] A. Hirata, T. Minotani, and T. Nagatsuma, “Millimeter-wave photonics for 10-Gb/s wireless link,” in IEEE LEOS Tech. Dig., pp. 477-478, 2002.

[1.8] A. Hirata, H. Togo, N. Shimizu, H. Takahashi, K. Okamoto, and T. Nagatsuma, “Low-phase noise photonic millimeter-wave generator using an AWG integrated with a 3-dB combiner,” IEICE Trans. Electron., vol. E88-C, no. 7, pp. 1458–1464, 2005.

[1.9] A. Hirata, H. Takahashi, R. Yamaguchi, T. Kosugi, K. Murata, T. Nagatsuma, N. Kukutsu, and Y. Kado, “Transmission characteristics of 120-GHz-band wireless link using radio-on-fiber technologies,” Journal of Lightwave Technology, vol. 26, no. 15, pp. 2338-234, 2008.

[1.10] ICNIRP, “Guidelines for limiting exposure to time-varying electric, magnetic, and electromagnetic fields (up to 300 GHz),” Health Physics, vol. 74, no. 4, pp. 494 -522, 1998.

[1.11] IEEE standard for safety levels with respect to human exposure to radio frequency electromagnetic fields, 3 kHz to 300 GHz, ANSI/IEEE Standard C95.1-1991, 1992.

[1.12] “Radio-radiation protection guidelines for human exposure to electromagnetic

fields," Telecommunication Technology Council, Ministry Posts Telecommunication, Deliberation Rep. 89, Tokyo, Japan, 1997 (in Japanese).

[1.13] http://www.speag.com/measurement/dasy5/dasy5_sar.php

[1.14] E. B. Joy, W. M. Leach, G. P. Rodrigue, and D. T. Paris, "Applications of probe-compensated near-field measurements," IEEE Trans. Antennas Propag., vol. 26, no. 3, pp. 379 – 389, 1978.

[1.15] H. I. Bassen and G. S. Smith, "Electric field probes – A review, " IEEE Trans. Antennas and Propag., vol. 31, no. 5, pp. 710 – 718, 1983.

[1.16] K. Pokovic, "Advanced electromagnetic probes for near-field evaluations," Dissertation of Swiss Federal Institute of Tech., Zurich, Switzerland, 1999.

[1.17] N. Kuwabara, K. Tajima, R. Kobayashi, and F. Amemiya, "Development and analysis of electric field sensor using LiNbO3 optical modulator," IEEE Trans. Electromagnetic Compatibility, vol. 34, no. 4, pp. 391 – 396, 1992.

[1.18] B. G. Loader, M. J. Alexander, W. Liang, and S Torihata, "An Optical Electric Field Probe for Specific Absorption Rate Measurements," 15th International Zurich Symposium on Electromagnetic Compatibility, 12C3, pp.57-60, Zurich, Switzerland, 2003.

[1.19] H. Togo, A. Sasaki, A. Hirata, and T. Nagatsuma, "Characterization of millimeter-wave antenna using photonic measurement techniques," Int. J. RF and Microwave CAS, vol. 14, pp. 290-297, 2004.

[1.20] T. Onishi, H. Togo, N. Shimizu, K. Kiminami, S. Uebayashi, and T. Nagatsuma, "SAR measurement employing electro-optic (EO) probe without using metal," in A joint meeting of the Bioelectromagnetics Society and the European Bioelectromagnetics Association (BioEM2005), Dublin, 2005.

[1.21] H. Togo, T. Onishi, K. Kiminami, N. Shimizu, T. Nagatsuma, and S. Uebayashi, "Tip-on-fiber electro-optic probe for specific absorption rate measurement," 2006 Asia-Pacific Microwave Photonics Conference, pp. 238-241, Kobe, 2006.

[1.22] H. Togo, N. Shimizu, and T. Nagatsuma, "Tip-on-fiber electro-optic probe for near-field measurement," NTT Technical Review, vol. 4, no. 1, pp. 12-20, 2006.

[1.23] H. Togo, N. Shimizu, and T. Nagatusma, "Near-field mapping system using fiber-based electro-optic probe for antenna characterization," IEICE Trans. Electron., vol.E-90-C, no. 2, pp. 436-442, 2007.

[1.24] T. Iyama, K. Kmiminami, and T. Onishi, "Applicability of three-axis electro-optic (EO) probe for specific absorption rate (SAR) measurement," IEICE Transactions on Communications, vol. E92.B, no.4, pp. 1414-1417, 2009.

[1.25] K. Kiminami, T. Iyama, T. Onishi, and S. Uebayashi, "Novel specific absorption rate (SAR) estimation method based on 2-D scanned electric fields," IEEE Trans.

Electromagn. Compat., vol. 50, no. 4, pp.828-836, Nov. 2008.

[1-26] K. Kamogawa, I. Toyoda, K. Nishikawa, and T. Tokumitsu, “Characterization of a monolithic slot antenna using an electro-optic sampling technique,” IEEE Microwave and Guided Wave Lett., vol. 4, pp. 414–416, 1994.

[1-27] T. Pfeifer, T. Loffler, H. G. Roskos, H. Kurz, M. Singer, and E. M. Biebl, “Electro-optic near-field mapping of planar resonators,” IEEE Trans. Antennas Propag., vol. 46, no. 2, pp. 284–291, 1998.

[1-28] S. Wakana, T. Ohara, M. Abe, E. Yamazaki, M. Kishi, and M. Tsuchiya, “Fiber-edge electrooptic/magnetooptic probe for spectral-domain analysis of electromagnetic field,” IEEE Trans. Microw. Theory Tech., vol. 48, no. 12, pp. 2611–2616, 2000.

[1-29] K. Yang, G. David, J. G. Yook, I. Papapolymerou, L. P. B. Katehi, and J. F. Whitaker, “Electrooptic mapping and finite-element modeling of the near-field pattern of a microstrip patch antenna,” IEEE Trans. Microw. Theory Tech., vol. 48, no. 2, pp. 288–294, 2002.

[1-30] N. Hidaka, K. Kobayashi, H. Sugama, R. Usui, Y. Tanabe, and O. Hashimoto, “Log-periodic dipole antenna array-type optical electric field sensor,” IEICE Trans. Electron., vol. E88-C, no. 1, pp. 98–104, 2005.

Chapter 2

Measurement with optical electric-field sensor

2.1 Introduction

Electric-field measurement using the optical electric-field sensor based on the bulk EO crystal has been attracting much attention because of its extremely large detectable bandwidth ranging from DC to THz. Near-field mapping above a planar resonator and a microstrip patch antenna has been demonstrated using an external probing technique, in which a free-space-propagating beam is focused into a miniature EO crystal [2.1], [2.2]. The demonstrations showed that the EO-based near-field mapping in amplitude and phase is powerful tool for the analysis and design of microwave-radiating structures. To shorten mapping time, two-dimensional-beam scanning on a large-aperture EO crystal has been employed [2.3]. Recently, a real-time mapping system with a parallel EO heterodyne detection scheme has been developed, in which 10,000 pixel data can be simultaneously acquired at the highest frame rate of 30 Hz [2.4]. In these measurement systems, free-space optics to control and arrange the polarization of light is fixed on an optical table and a bread board. An accessible point of the sensor is limited on the table and board. To expand the accessibility of the sensor, Shinagawa et al. integrated the free-space optics in the handy-held cylinder [2.5]. Their results demonstrate that the probe is useful for the noncontact measurement of free-space electric fields, for example, in electromagnetic interference (EMI) applications. In the head of the handy sensor, a distributed feedback laser (DFB-LD) is integrated to stabilize the polarization of input light. To detach the DFB-LD from the sensor head, the polarization maintaining fiber (PMF) was connected with DFB-LD [2.6]. However, the cylinder and the inside optics can disturb near field of DUT. To minimize disturbances and easily position the bulk-EO-based sensor tip over any point to be probed, Nagatsuma et al. introduced an optical fiber to an EO-based electric-field measurement system [2.7]. Ohara et al. demonstrated the first near-field mapping using a fiber-mounted sensor fixed on the x-y stage equipped in a microscope [2.8]. Afterward, near-field mapping to diagnose monolithic microwave integrated circuits and evaluate electromagnetic interference was successively accomplished over a microstrip line and antenna with the fiber-mounted sensor [2.9]-[2.11]. Since the EO crystal was mounted on the edge of an optical fiber, the fiber-mounted sensor makes it possible to map out the electric-field in an enclosed miniature structure with negligibly small invasiveness.

This chapter describes the features and the principles of electric-field measurement with EO

effect, and then shows the configurations and the basic properties of our developed handy-held sensor where all free-space optics is integrated, and the application of the sensor to MMW antenna measurements. Moreover, this chapter explains our fiber-mounted sensor developed in consideration of its use in practical applications, and demonstrates the potential of near-field mapping around a dipole antenna in free space and electric-field mapping in an absorptive liquid used as a tissue-equivalent phantom (TEP) to assess the SAR [2.12], [2.13]. Those demonstrations involve simultaneous mapping of amplitude and phase distribution, which was impossible with a conventional probe.

2.2 Electric-field detection based on EO effect

2.2.1 EO effect

An EO effect is a change in the optical properties of a material in response to an electric field that varies slowly compared with the frequency of light. The term encompasses a number of distinct phenomena, which can be subdivided into

a) Change of the refractive index

Pockels effect (or linear EO effect):

Change in the refractive index linearly proportional to the electric field. Only certain crystalline solids show the Pockels effect, as it requires lack of inversion symmetry, such as lithium niobate ($LiNbO_3$) or gallium arsenide (GaAs) and in other noncentrosymmetric media such as electric-field poled polymers or glasses. [2.14]

Kerr effect (or quadratic EO effect, QEO effect):

Change in the refractive index proportional to the square of the electric field. All materials display the Kerr effect, with varying magnitudes, but it is generally much weaker than the Pockels effect [2.15], [2.16]

Electro-gyration:

Change in the optical activity [2.17]

b) Change of the absorption

Franz-Keldysh effect:

Change in the absorption shown in some bulk semiconductors [2.18]

Quantum-confined Stark effect:

Change in the absorption in some semiconductor quantum wells [2.19]

Electro-chromatic effect:

Creation of an absorption band at some wavelengths, which gives rise to a change in

color [2.19].

It should be noted that changes in absorption can have a strong effect on refractive index for wavelengths near the absorption edge, due to the Kramers–Kronig relation [2.20].

In the optical electric-field sensor, the Pockels effect is preferred to be used because of its ultra-wide bandwidth ranging from DC to several terahertz (THz), its relatively high coefficient depending on applied electric-field and input light intensity comparing with the other EO effects. With the advance and the popularity of laser technology in the latter half of 1960, a lot of studies had been reported about the materials with the Pockels effects and some applications occurred as a voltage-controlled wave plate or Pockels cell, a light modulator [2.21], and optical electric-field sensor. With the appearance of ultra-fast lasers in 1980, the sampling techniques based on the EO effect, or EO sampling, has the highest temporal resolution of any method used to characterize electric signals on account of the short duration of the laser pulses, which behave as sampling gates. For example, a guided electric transient with a rise time of less than 300 fs had been measured using the EO sampling with a 100 fs full width at half-maximum (FWHM) amplitude laser pulse [2.22], [2.23]. Free-space-radiated THz beam transients had been detected using the EO sampling with a 12 fs duration laser pulse [2.24].

2.2.2 Principles of electric-field detection with EO effect

Fig. 2-1 shows the basic structure of the optical electric-field sensor based on EO effect with a bulk crystal [2.6]. It comprises polarizing-beam splitters (PBSs), a quarter wavelength plate (QWP), a Faraday rotator (FR), and an EO crystal of Cadmium Telluride (CdTe) with a zinc-blende crystal lattice, which has the highest sensitivity factor for free-space detection in inorganic crystals and no static birefringence as shown in Table 2-1. The optical pulses for EO sampling pass through the PBS2, the FR, the PBS1, the QWP, and then, penetrate the (-110) plane perpendicularly and are reflected by the dielectric mirror coating the (110) plane of the EO crystal. The electric-field signal to be measured enters the crystal through the mirror and propagates together with the reflected pulses. The polarization of the pulses is modulated by the transient electric field parallel to the (110) plane and perpendicular to the (1-10) plane. The polarization component parallel to the reflection axis of the PBS1 is extracted from the polarization-modulated pulses as intensity-modulated pulses. The orthogonal component is rotated an additional 45 degree by the FR and reflected by the PBS2. The components are respectively delivered to photo-detectors (PDs), where they are converted into electrical signals. The signals are inputted to a differential amplifier. The output signal from the amplifier is processed by a spectrum analyzer or an oscilloscope.

Table 2-1. Properties of typical EO crystals for transverse detection.

Material	Point group	Pockels coefficient r (pm/V)	Relative index n	Dielectric constant ε	Sensitivity factor
CdTe	43m	$r_{41} = 4.5$ (1000 nm)	$n_o = 2.84$ (1000 nm)	9.4	$n_o^3 r_{41}/\varepsilon = 11.0$
ZnTe	43m	$r_{41} = 3.94$ (690 nm)	$n_o = 2.93$ (690 nm)	10.1	$n_o^3 r_{41}/\varepsilon = 9.8$
GaAs	43m	$r_{41} = 1.43$ (1150 nm)	$n_o = 3.43$ (1150 nm)	12.3	$n_o^3 r_{41}/\varepsilon = 4.7$
KH_2PO_4 (KD*P)	42m	$r_{63} = 24.1$ (633 nm)	$n_o = 1.502$ $n_e = 1.462$ (633 nm)	58	$n_o^3 r_{63}/\varepsilon = 1.4$
$LiNbO_3$	3m	$r_{33} = 30.8$ $r_{13} = 8.6$ (633 nm)	$n_o = 2.286$ $n_e = 2.200$ (633 nm)	43	$(n_e^3 r_{33} - n_o^3 r_{13})/\varepsilon = 4.7$
$LiTaO_3$	3m	$r_{33} = 33$ $r_{13} = 7.5$ (633 nm)	$n_o = 2.176$ $n_e = 2.180$ (633 nm)	41	$(n_e^3 r_{33} - n_o^3 r_{13})/\varepsilon = 6.4$

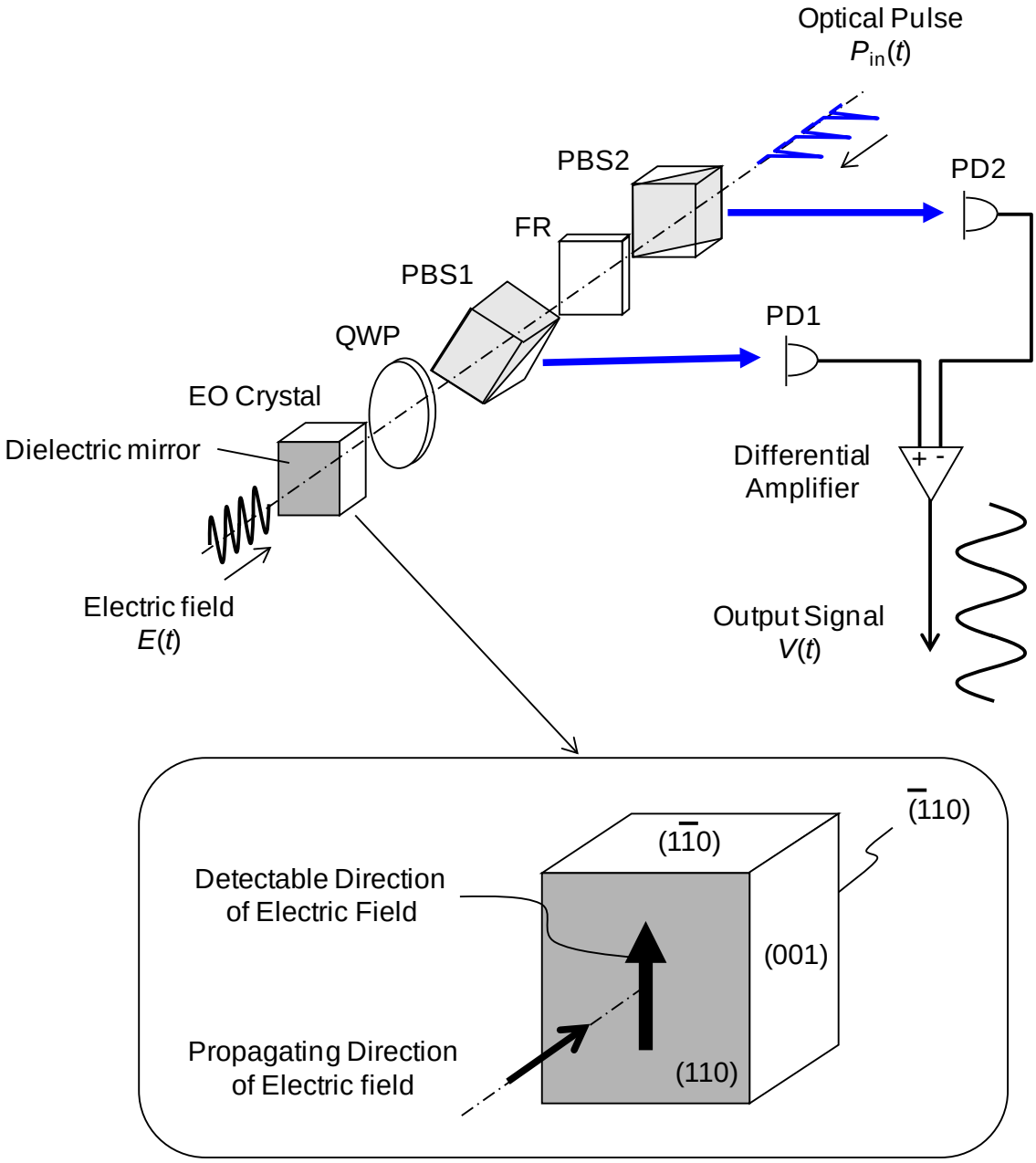

Fig. 2-1. Schematic diagram of optical electric-field sensor based on bulk EO crystal.

This bulk-crystal-based optical electric-field sensor can be considered to be a photonic mixer [2.25]. The intensities of the optical beams reflected by PBS1 and 2 are

$$P_{\text{out1}}(t) = \frac{1}{2}\{1 + \alpha E(t)\}P_{\text{in}}(t) \tag{2.1}$$

$$P_{\text{out2}}(t) = \frac{1}{2}\{1 - \alpha E(t)\}P_{\text{in}}(t) \tag{2.2}$$

$$\alpha \equiv \frac{2\pi l}{\lambda} n^3 r_{41}, \tag{2.3}$$

where $P_{\text{in}}(t)$, $E(t)$, l, λ, n, and r_{41} represent the power of the input optical pulses, the intensity of the electric-field signal to be measured, the interaction distance of the input optical pulses within the crystal, the wavelength of the input optical pulses, the refractive index, and the electro-optic coefficient of the crystal, respectively. When the repetition frequency and average power of the input optical pulses are f_0 and P_{av}, $P_{\text{in}}(t)$ is expressed as follows.

$$P_{\text{in}}(t) = \sum_{m=-\infty}^{\infty} \frac{P_{\text{av}}}{f_0}\delta\left(t - \frac{m}{f_0}\right) = P_{\text{av}}\left(1 + 2\sum_{m=1}^{\infty}\cos 2\pi m f_0 t\right). \tag{2.4}$$

To sample the electric-field signal by using the optical pulses, the repetition frequency of the electric-field signal, f_{ef}, must be equal to $Nf_0 + \Delta f$, where N and Δf are an integer and a small frequency shift, respectively [2-6]. Then, electric field of the electric-field signal, $E(t)$, is written as

$$E(t) = \sum_{k=-\infty}^{\infty} c_k \exp[j2\pi k(Nf_0 t + \Delta f)], \tag{2.5}$$

where c_k are complex coefficients. Substituting (2.4) and (2.5) into (2.1) and (2.2), one obtains

$$P_{\text{out1}}(t) = \frac{P_{\text{av}}}{2}\{1 + \alpha E_{\text{IF}}(t)\} \tag{2.6}$$

$$P_{\text{out2}}(t) = \frac{P_{\text{av}}}{2}\{1 - \alpha E_{\text{IF}}(t)\} \tag{2.7}$$

$$E_{\mathrm{IF}}(t) \equiv \sum_{k=-\infty}^{\infty} c_k \exp[j 2\pi k \Delta f\, t] \,. \tag{2.8}$$

To derive the above results, frequency components higher than f_0 are neglected, because the PDs cannot respond to high-frequency components.

Comparing (2.5) and (2.8), it is clear that $E_{\mathrm{IF}}(t)$ is a time-stretched replica of $E(t)$. In other words, the frequency components of $E(t)$, $Nf_0 + \Delta f$, $2Nf_0 + 2\Delta f$, $3Nf_0 + 3\Delta f$,…, are down-converted to Δf, $2\Delta f$, $3\Delta f$,…, respectively. The phase relations between the components of $E(t)$ are also conserved when the frequency components are down-converted. The electrical output signals of PD1 and 2 are thus

$$v_1(t) = \frac{v_{\mathrm{av}}}{2}\{1 + \alpha E_{\mathrm{IF}}(t)\} \tag{2.9}$$

$$v_2(t) = \frac{v_{\mathrm{av}}}{2}\{1 - \alpha E_{\mathrm{IF}}(t)\}, \tag{2.10}$$

where v_{av} is the DC output voltage corresponding to P_{av}. The DC component is cancelled by differential detection as follows.

$$v(t) \equiv v_1(t) - v_2(t) = \alpha v_{\mathrm{av}} E_{\mathrm{IF}}(t) \,. \tag{2.11}$$

Thus, I can obtain an electrical signal proportional to $E_{\mathrm{IF}}(t)$. Since a slow signal $E_{\mathrm{IF}}(t)$ is a replica of $E(t)$, it is easy to extract information about the electric-field signal by using conventional instruments.

2.3 Compact optical electric-field sensor

2.3.1 Sensor configurations

Fig. 2-2 shows a photograph of the compact optical electric-field sensor where all optical components described in the chapter 2.1.2 are integrated inside the cylinder and are fixed to maintain optimum conditions [2.6]. The EO crystal with a dielectric mirror is attached to the cylinder head. The probe is connected to a set of cords containing a polarization-maintaining fiber (PMF) and two single-mode fibers (SMFs). The PMF is used to deliver sampling optical pulses from the optical source to the probe. Since the polarization state of the incident optical pulses are maintained, stable measurement is possible even when the probe is moved to map electric-field patterns. The SMFs transmit optical pulses containing information about the measured electric field.

Figure 2-3 shows a schematic diagram of the EO sampling (EOS) system for measuring the free-space electric-field radiated from the antenna. The electric-field signals are sent to the antenna and mixer after being generated by a synthesizer (frequency $Nf_0 + \Delta f$ of f_{ef} + 98 kHz). An actively mode-locked fiber laser was the source of the optical pulses for sampling. The pulses transmitted through the PMF to the sensor had a width of about 400 fs and were generated at a repetition frequency f_0 of 1 GHz and wavelength of 1.55 μm. The down-converted electric-field signals $v(t)$ were detected with a spectrum analyzer so that the electric field could be numerically evaluated at any point. A reference signal Δf of 98 kHz was generated by the mixer and injected into the spectrum analyzer. The antenna was fixed during the measurement and the EO probe moved in order to scan the electric field. The frequency bandwidth (time resolution) of the EOS was determined from the optical pulse width and the thickness of the EO crystal. The bandwidth was limited by the group velocity mismatch (GVM), defined as the difference in the time it takes the MMW signal and the optical pulses to go through the EO crystal [2.26]. The thickness of the EO crystal was optimized for frequencies higher than 150 GHz. The dependence of the EO sensitivity on the temperature was negligible during the measurement, because the change in the optical path length through the crystal and the refractive index of the crystal are very small (linear expansion coefficient: 5.0×10^{-6}, temperature dependence of the refractive index: 3.0×10^{-6}). Moreover, pyro-electric phenomena do not exist in the crystal used by the measurement system.

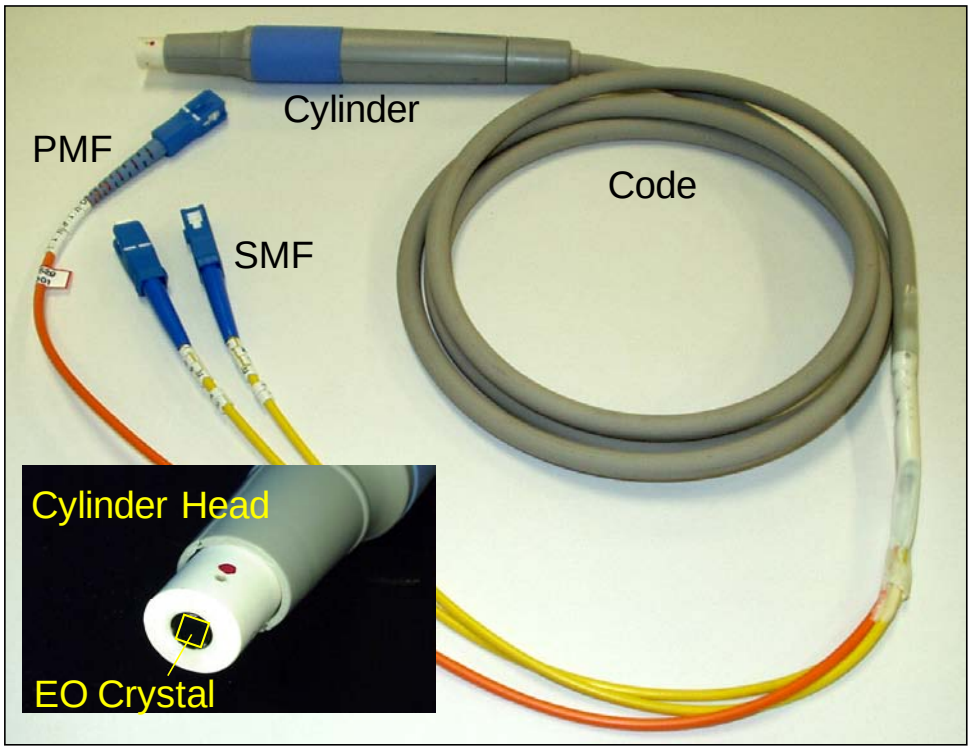

Fig. 2-2. Photograph of compact optical electric-field sensor where all optical components are integrated inside of the cylinder.

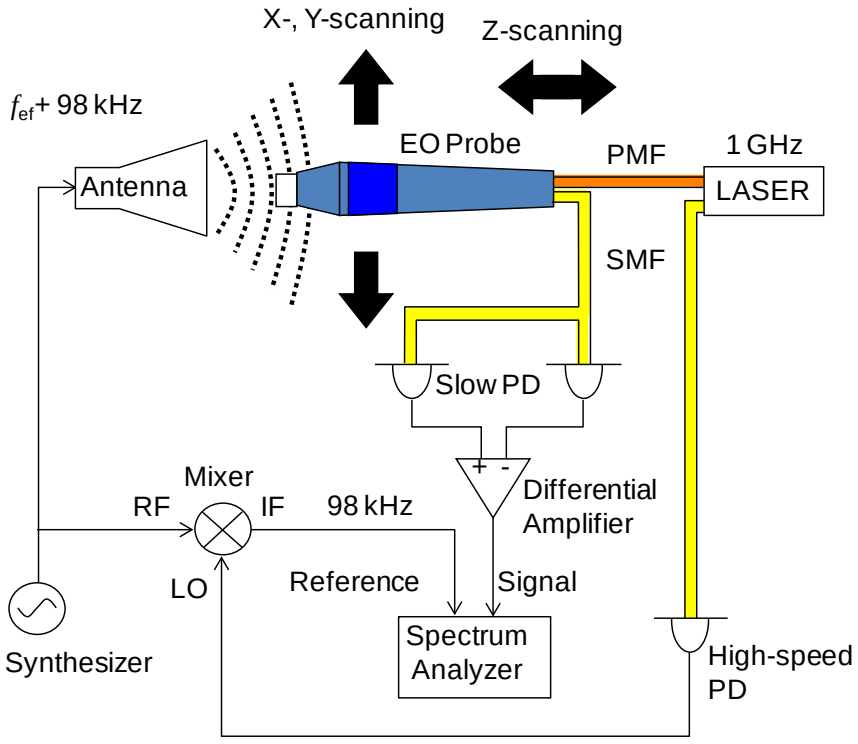

Fig. 2-3. Configuration of electric-field measurement system with EO sampling techniques.

2.3.2 Electric-field measurements

A. Electric-field distribution measurements

The CW MMW electric field radiated from a pyramidal horn antenna was measured to obtain near and far-field patterns. The electric field excited by the TE_{10}-mode was radiated from a standard-gain horn antenna for WR-15. The size of the antenna aperture was 36.2 mm x 27.7 mm, and the length of the horn was 63.1 mm. The direction parallel to the longer side, the orthogonal direction, and the propagating direction of the MMW are assumed to be the x-, y-, and z-axes, respectively. Fig.2-4 shows the dependence of EO signal intensity on the MMW electric field at the center of the antenna aperture. The electric fields are estimated from the power injected into the antenna and are shown as diamonds in the figure. The solid and broken lines represent the electric field estimated from Equation (2.11) and the noise level in the EOS system, respectively. The EO signal is linearly proportional to the electric field at the electric field of more than 100 V/m, and the minimum detectable MMW electric field is less than 1.0 V/m, which is less than a tenth of the electric field reported in [2.27].

Fig. 2-5 shows the electric field measured at the center of the traveling MMW, that is, the z-axis, where the position at the antenna aperture is the origin and the traveling direction is positive. In the figure, the diamonds represent the electric field measured by the EOS system. We calculated the near field using the FEM simulator (Agilent Tech.: HFSS) to compare the measured results. In the calculated model, the TE_{10} mode is excited at the input port. The antenna is surrounded by an air box whose surface is specified as having absorbing boundary conditions in order to eliminate artificial reflections. The solid line represents the electric field calculated by FEM. The electric field continuously falls as the distance from the connection between waveguide and antenna increases, and outside the aperture, the electric field increases due to radiation interference from any position on the plane of the aperture. The measured electric field closely resembles the calculated one.

Figures 2-6 and 2-7 show the measured electric field parallel to the x- and y-axes. The distance from the antenna aperture is 5 mm, which is equal to the wavelength of the MMW and corresponds to the near-field region. These results represent the near-field patterns complicated by the radiation interferences from any positions on the plane of the aperture. The agreement between the measured and the FEM-calculated electric fields parallel to the x-axis is excellent. A slight deference between the measured and calculated electric fields parallel to the y-axis is observed, because the spatial resolution of the sensor is larger than the minimum distance with the variation of the electric field. The spatial resolution is limited by the size of the optical beam spot in the EO crystal. A spatial resolution of less than 1 mm will be possible by downsizing the spot size.

Figures 2-8 and 2-9 show the E- and H-plane radiation patterns of the pyramidal horn antenna at 60 GHz. The distance from the antenna to the probe is 300 mm for these measurements, corresponding to 60 wavelengths in the far-field region. Broken and solid lines represent the

measured pattern at the distance from the antenna aperture to EOS probe and the one calculated by FEM. The measured pattern is similar to the calculated one, demonstrating that the sensitivity of EOS probe is stable while the probe is being moved.

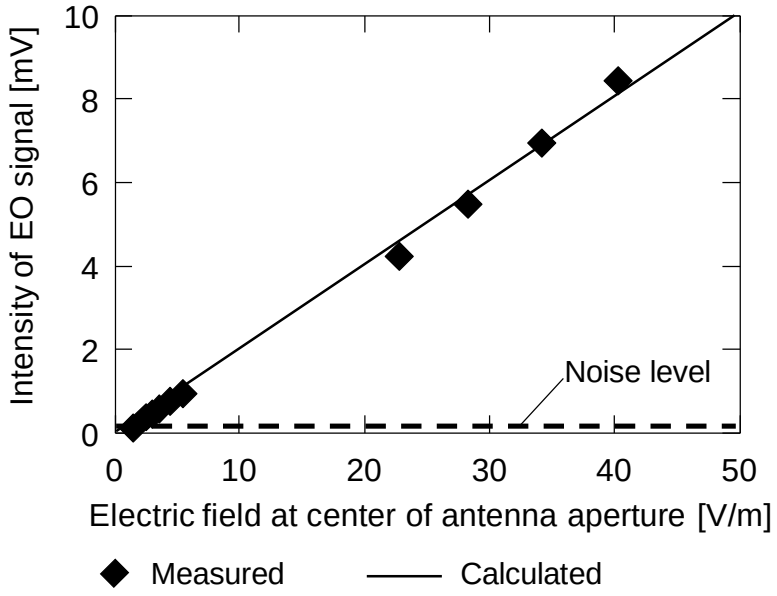

Fig. 2-4. Relationship between electric-field intensity at center of antenna aperture and EOS signal.

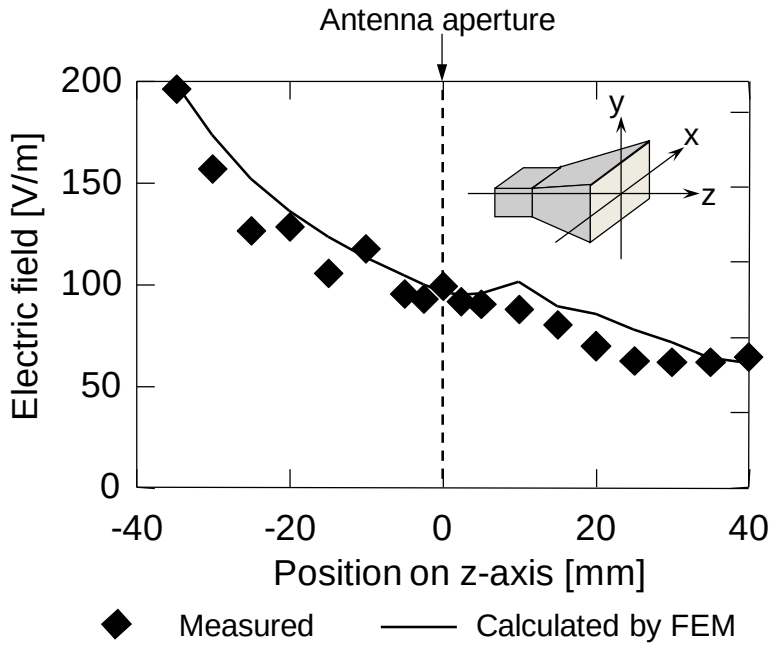

Fig. 2-5. Electric-field distribution along MMW propagation axis (Z-axis).

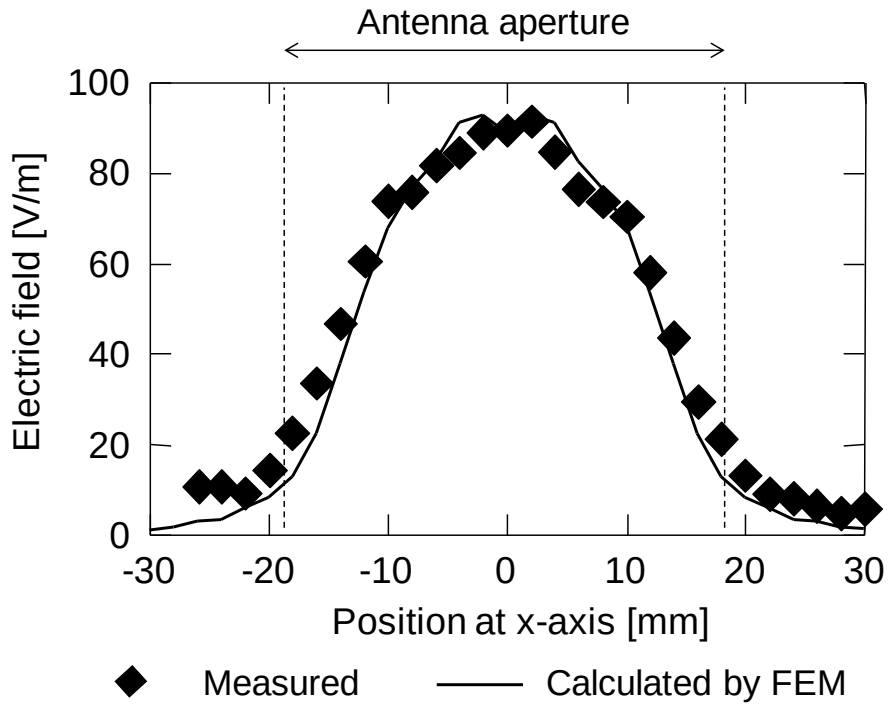

Fig. 2-6. Electric-field distribution along x-axis with a distance of 5 mm from antenna aperture.

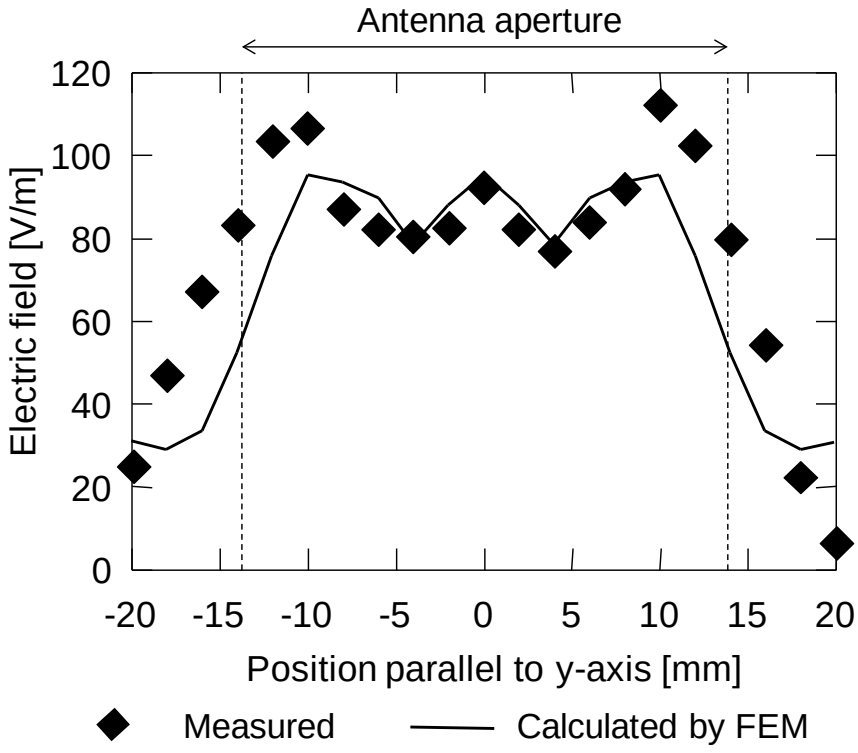

Fig. 2-7. Electric-field distribution along y-axis with a distance of 5 mm from antenna aperture.

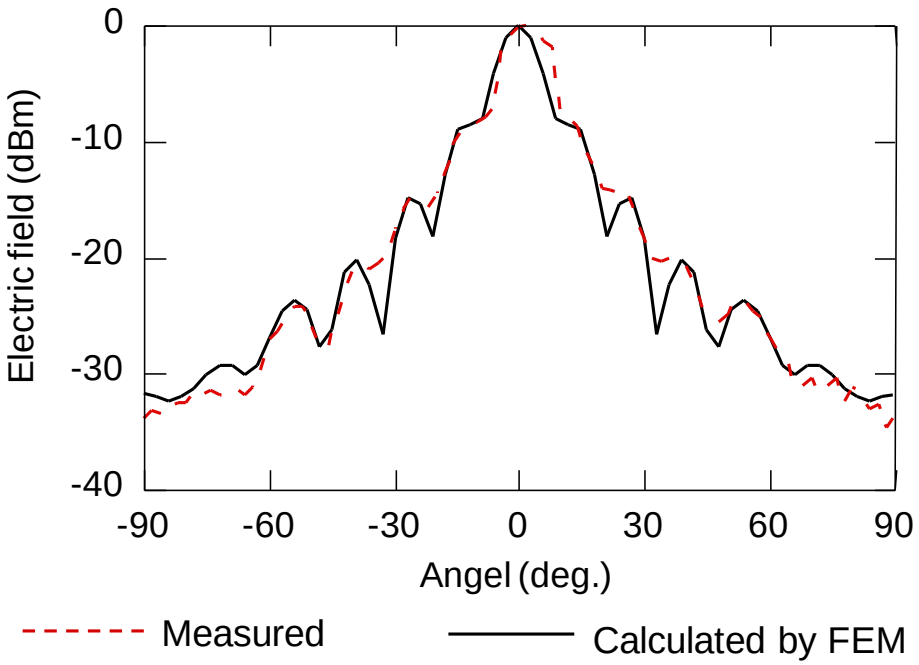

Fig. 2-8. Antenna pattern in E-plane along y-axis.

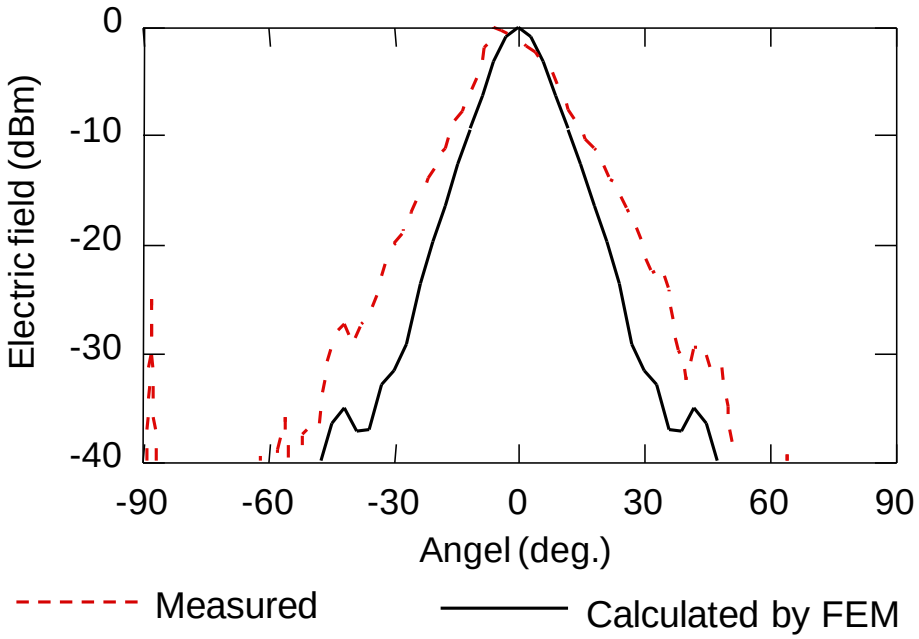

Fig. 2-9. Antenna pattern in H-plane along x-axis.

B. Time-domain waveform measurements

The time domain waveform was measured with the handy senor. The pulse signal was radiated from a photonic emitter, in which a uni-traveling carrier photodiode (UTC-PD) and MMW antenna with a bandwidth of 49 GHz at the center frequency of 120 GHz were integrated [2.28]. Figure 2-10 shows a simplified drawing of the measurement system. The UTC-PD was flip-chip-bonded on the transmission line of a slot antenna formed on the Si substrate. The size of the Si substrate was 4 mm x 2mm x 0.4 mm. A hemispherical Si lens with a radius of 5 mm was bonded to the bottom of the Si substrate. The 400-fs-wide optical pulses were generated by a gain-switched laser at a repetition frequency f_0 of 1 GHz and converted into electric pulses with a full width of half maximum (FWHM) of 5.4 ps by the UTC-PD, before being radiated from the MMW antenna. The frequency shift Δf was set to 4 kHz. We calculated the near field in the time domain be using the FIM simulator (CST GmbH: MW-Studio) for comparison with the measured results. In the calculated model, the photonic emitter is surrounded by an air box whose surface is specified as having a perfectly matched layer (PML) absorbing boundary.

In Figure 2-11, the solid line represents the time-domain waveforms of the electrical pulses propagating on the transmission line from the UTC-PD, which were measured by the EO system for the internal-mode measurement [2.29]. The broken line represents the FIM simulation's time-domain waveform fitted to the measured one. It is an approximate Gaussian pulse with an FWHM of 5.4 ps.

Figure 2-12 shows the time-domain waveforms of the pulse radiated from the photonic emitter as measured by the EOS system (represented by the line) and as calculated by FIM (represented by the broken line). The distance between the photonic emitter and the EO crystal was 20 mm, and the position of the EO crystal was in the maximum radiation direction. At an earlier half duration, the measured waveform agreed with the calculated one. However, after about 20 ps from the first peak, the oscillation period of the measured waveform gradually got larger than the calculated one. This ringing continued for about 50 ps and was caused by multiple reflections at the connection, where the UTC-PD was flip-chip mounted on the antenna chip.

Figure 2-13 shows the frequency spectra calculated by fast fourier transform (FFT) from the time-domain waveforms. The frequency of maximum intensity of the measured pulse agrees with the calculated one of about 75 GHz. The measured bandwidth is smaller than the calculated one because of the ringing. The first peak represents the later oscillating frequency caused by the multiple reflections. These results indicate that the compact optical electric-field sensor is less invasive and has a large bandwidth of 150 GHz.

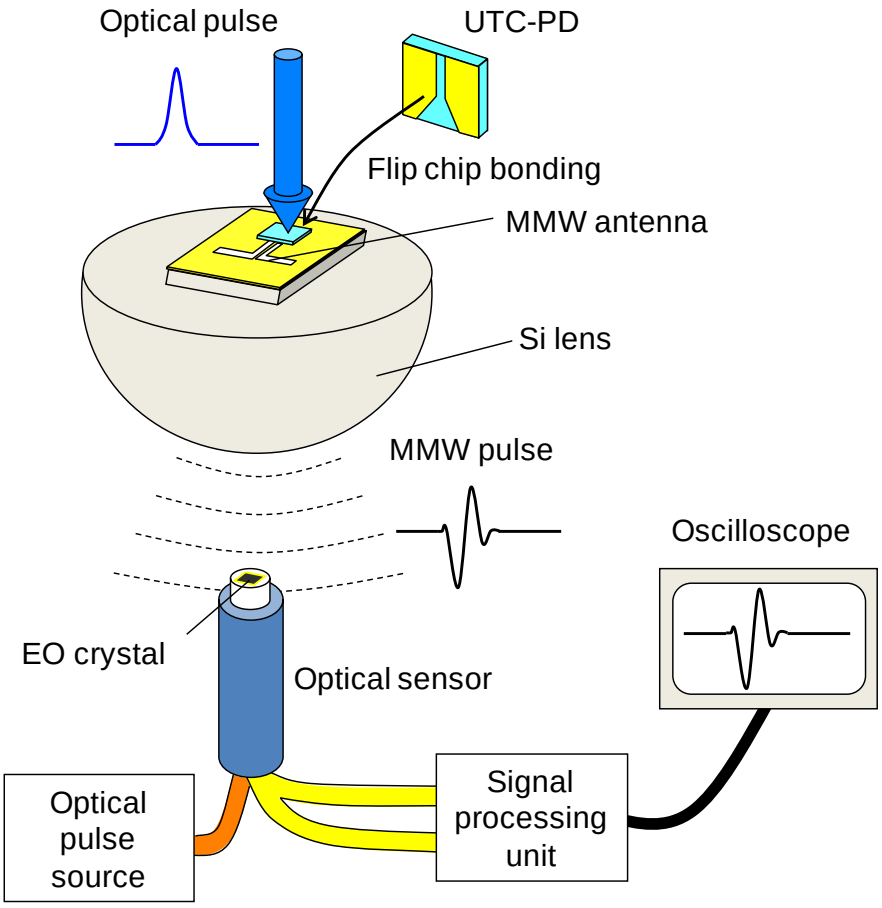

Fig. 2-10. Time-domain waveform measurement system with EOS techniques.

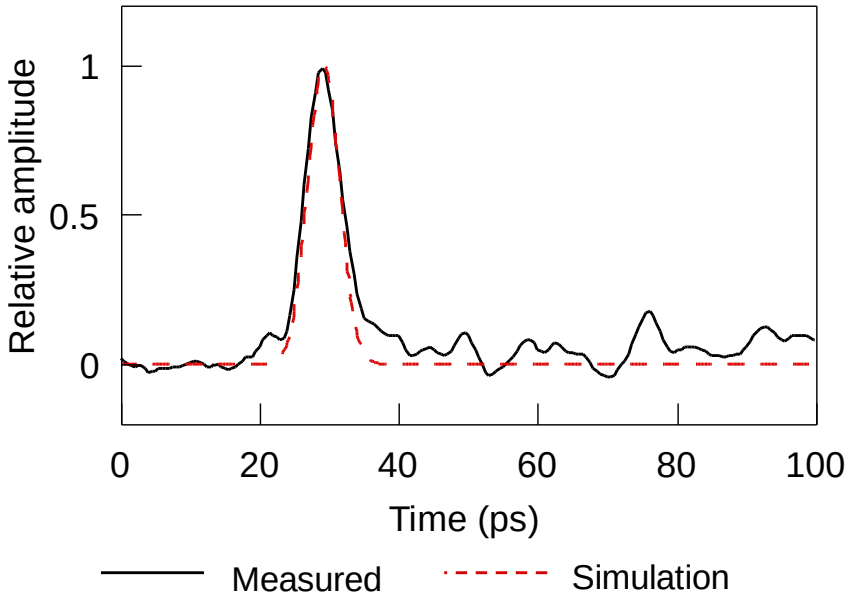

Fig. 2-11. Transient signal on transmission line in UTC-PD.

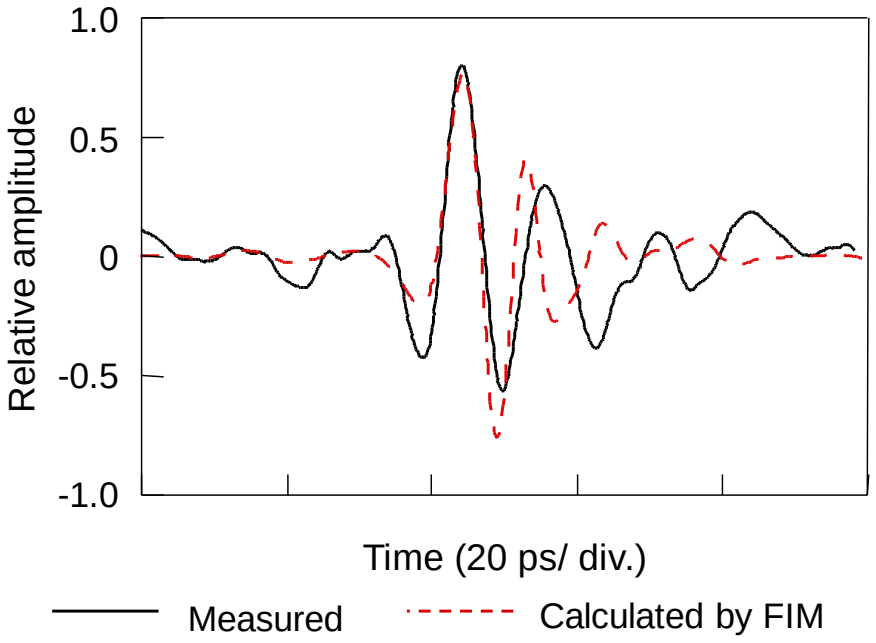

Fig. 2-12. Transient signal radiated from photonic emitter.

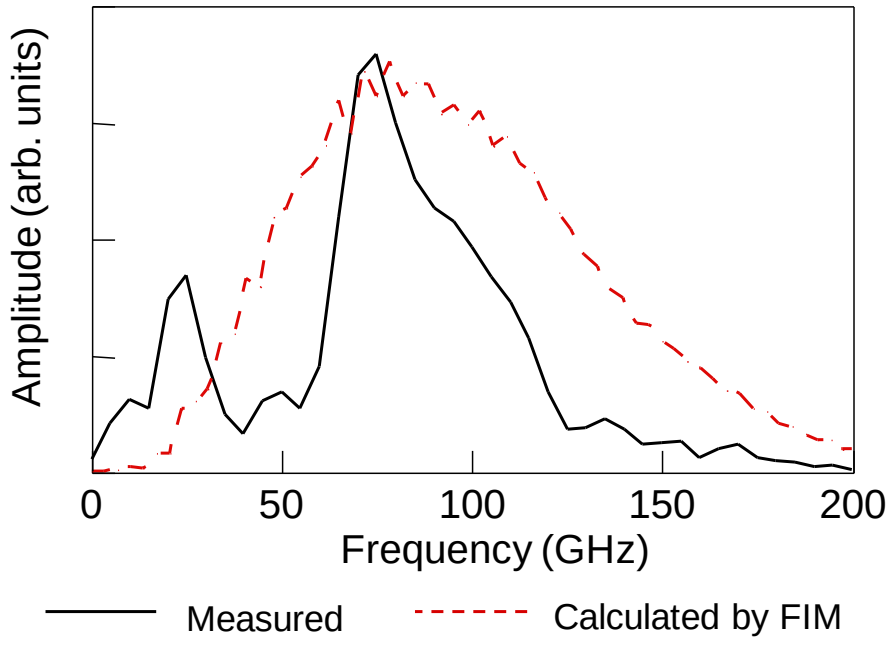

Fig. 2-13. Frequency spectrum of pulse signal radiated from photonic emitter with FFT.

2.4 Less-invasive optaical electric-field sensor

2.4.1 Sensor configurations

The compact optical electric-field sensor as described in the chapter 2.2 shows the flat sensitivity from several megahertz to several hundred gigahertz. However, invasiveness due to reflection from the cylinder and the optical components inside it was still a problem for more accurate measurement. To solve this problem, I recently developed a tip-on-fiber EO probe where the EO crystal is connected to the optical components with an optical fiber. A side view of the sensor tip with a CdTe crystal is shown in Fig. 2-14 [2.12], [2.13]. The tip contains the EO crystal with a dielectric mirror, a collimating lens, and a glass ferrule. The diameter of the laser beam in the crystal is 0.4 mm. The cross-sectional dimension of the EO crystal is 1 mm x 1 mm, which is smaller than that of dipole antenna in a MZI-based sensor [2.30], [2.31]. This small sensor tip reduces invasiveness and allows me to miniaturize the special resolution necessary for standardized measurement. Fig. 2-15 illustrates of the whole sensor. The sensor tip and an optical fiber connector are fixed at either end of a glass tube. The diameter and length of the glass tube are 5 and 300 mm, respectively. A single mode fiber that connects the EO crystal and fiber connector is inside of this glass tube. This sensor is directly attached to a polarization control module with the fiber connector.

The sensor employs the EO crystal of CdTe crystal that is an optically isotropic crystal with zinc-blend crystal lattice. Fig. 2-16(a) and (b) illustrate a longitudinal field probe, which detects an electric field parallel to a propagating direction of a laser beam, and a transverse field probe, which detects an electric field orthogonal to the propagating direction. Both sensors exhibit the same sensitivities when the crystal has a cubic structure.

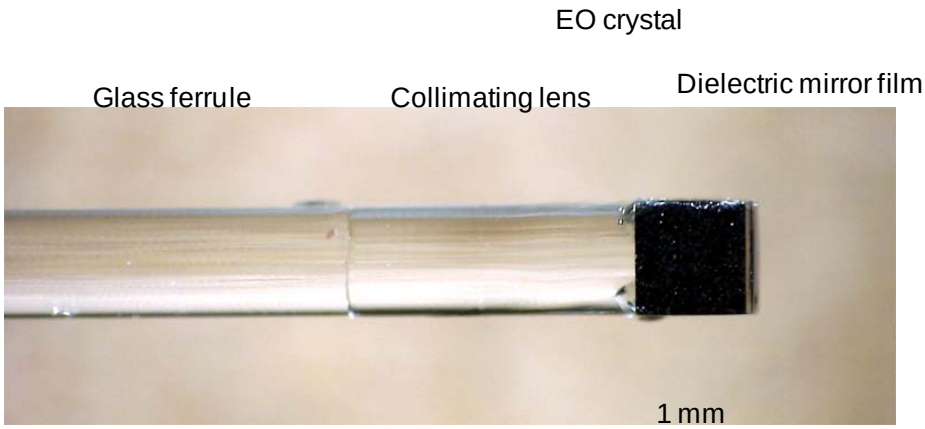

Fig. 2-14. Tip of optical electric-field sensor with EO crystal mounted on optical fiber.

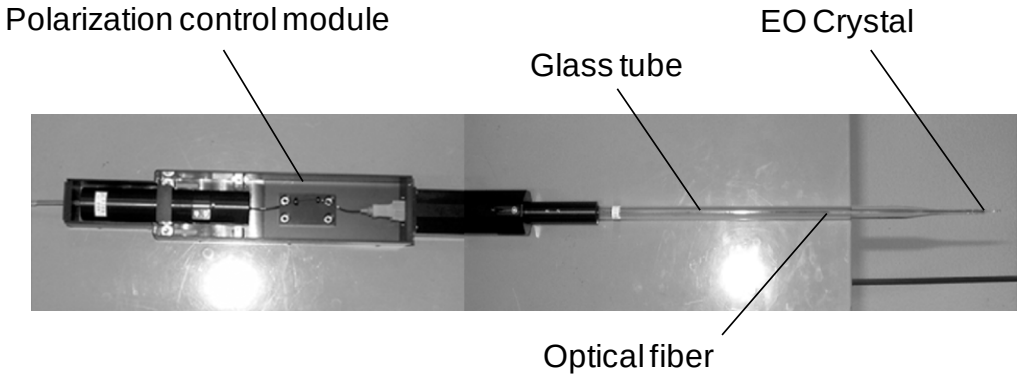

Fig. 2-15. Whole sensor with EO crystal mounted on fiber tip.

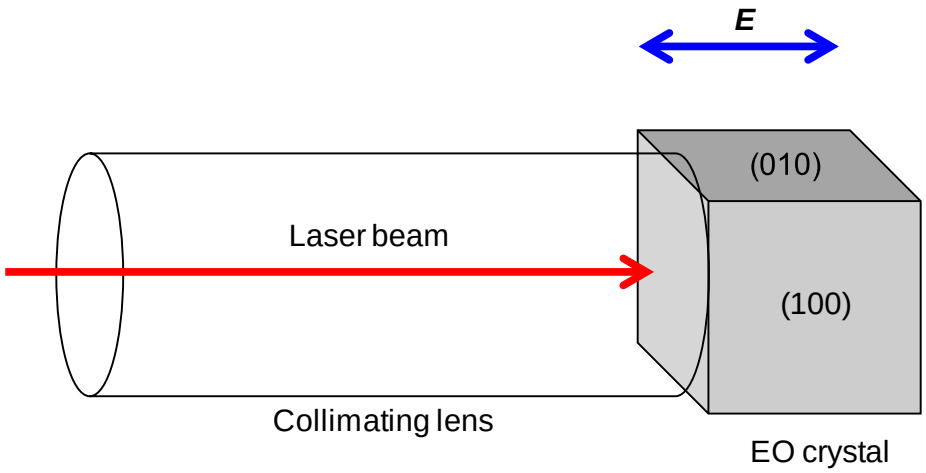

(a) Longitudinal field sensor

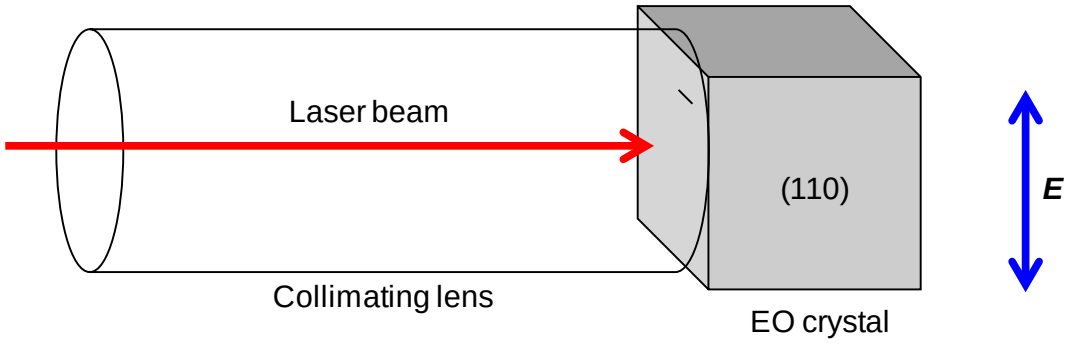

(b) Transverse field sensor

Fig. 2-16. Relationship between orientation of crystal and detectable direction of electric field for longitudinal field sensor (a) and transverse field sensor (b).

A block diagram of an electric field measurement system using the sensor is shown in Fig. 2-17. The system comprises a laser source, the polarization control module, the EO probe, a receiver (Rx), a two-dimensional (2D) scanning stage, signal generators (SGs), and a lock-in amplifier (LIA) or a spectrum analyzer. The laser source emits a linearly polarized light. The linearly polarized light is delivered to the EO probe through the polarization control module with a polarization-maintaining fiber. The delivered light is reflected by the dielectric mirror and returned to the receiver after it is spilt into two lights whose polarizations are orthogonal to each other. The received lights are converted to electrical signal by balanced photodetectors and a differential amplifier. The signal intensity is proportional to the change in polarization. The LIA measures the intensity of the obtained electrical signal, which coincides with that of the applied electric field.

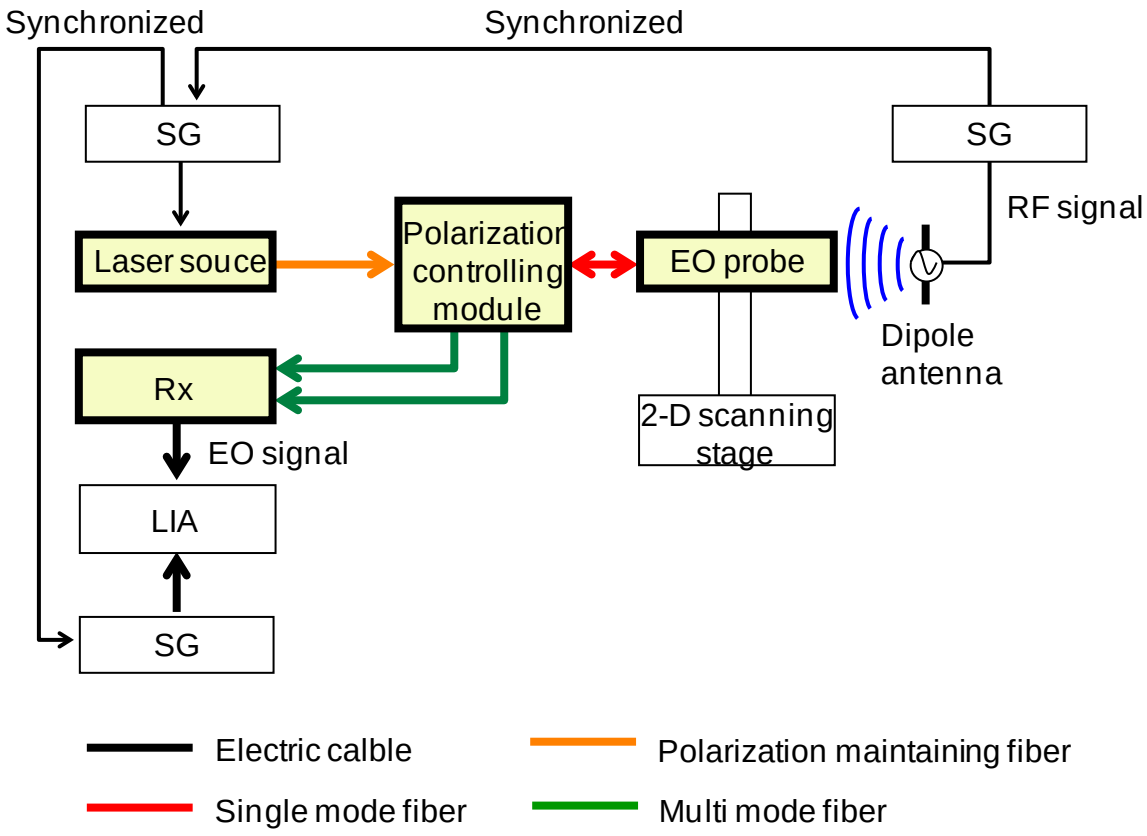

Fig. 2-17. Block diagram of electric-field distribution measurement system with less-invasive sensor.

2.4.2 Basic properties

A. Electric field around the EO probe

I calculated the electric-field intensity around the less-invasive sensor in free space using the finite integration method. The E- and H-planes of electric field with size of 20 mm x 30 mm are shown in Fig. 2-18(a) and (b), respectively. The calculated region was a rectangular parallelepiped with a height and width of 50 mm and a length of 200 mm. The electromagnetic wave was a plane wave oscillated at 1.95 GHz. Periodic boundary conditions and a perfectly matched layer are assigned on planes orthogonal to the propagating direction and on the output plane, respectively. The degree of intensity is represented as a color gradation. In those figures, no disturbance exists outside the region at the distance of 2 mm from the EO probe.

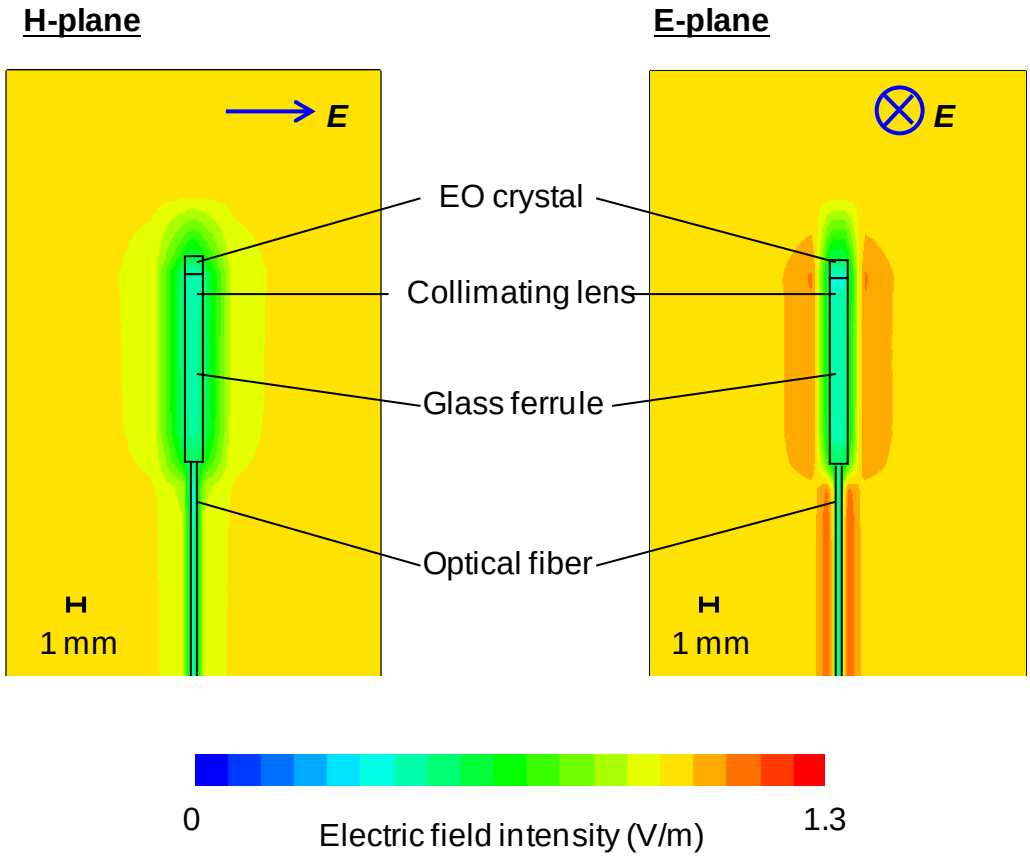

Fig. 2-18. Calculated electric field around less-invasive sensor along H-plan (a) and E-plan (b).

B. Sensitivity

The relationship between the input power of the dipole antenna and the EO signal intensity measured with the longitudinal field sensor is shown in Fig. 2-19. The sensitivity of the sensors was measured using an electric field radiated in free space from a half-wavelength dipole antenna (Anritsu MA5612B4) under the condition mentioned below. The dipole antenna, the sensor, polarization control module, and 2D scanning stage were set inside an RF shield box with dimension of 900 mm x 900 mm x 900 mm, and all other instruments were set outside the shield box. The return loss of walls inside the shield box is larger than 40 dB. The center of the EO crystal is kept at distance of 5 mm from the feeding point of the dipole antenna, while the signal generator inputs a sinusoidal signal with a frequency of 2.45 GHz to the dipole antenna. The dynamic range is over 45 dB. A minimum detectable electric field intensity defined by noise floor is less than 0.6 V/m. For the transverse field probe, the same sensitivity is also achieved.

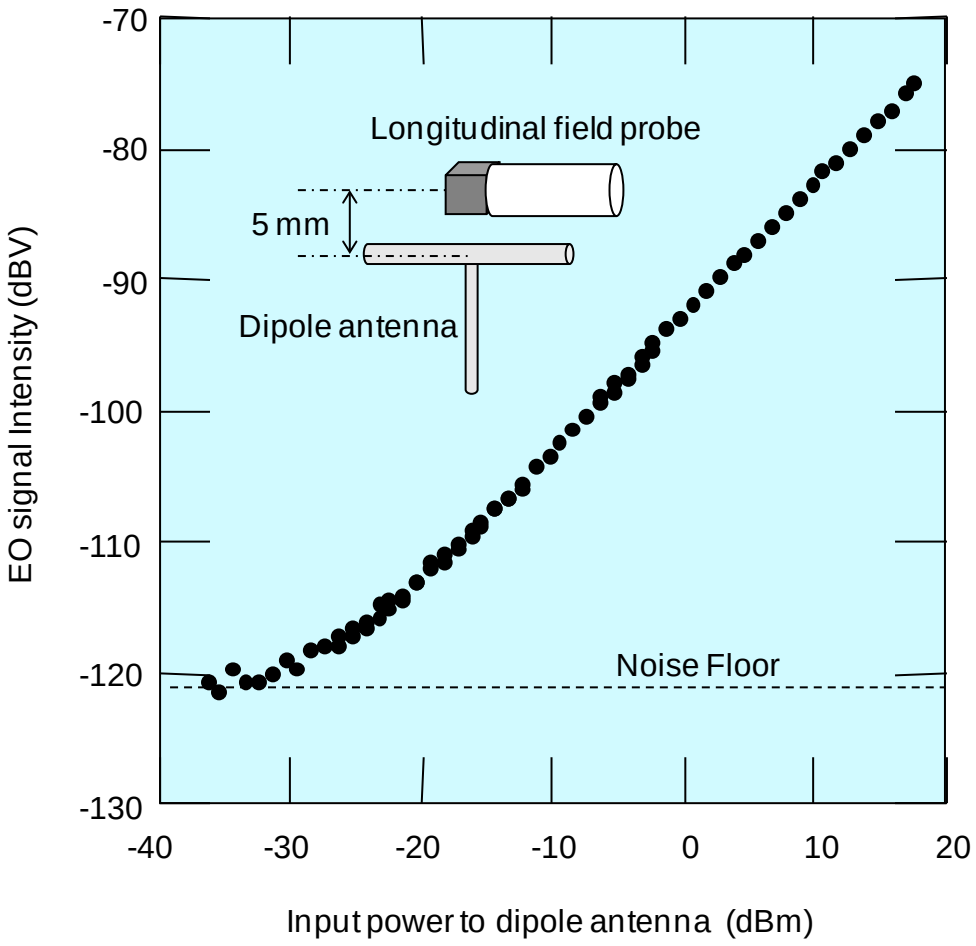

Fig. 2-19. Relationship between input power into dipole antenna and EO signal intensity.

C. Directivity

The directivities of the longitudinal and transverse field sensor are shown in Fig. 2-20 and Fig. 2-21, respectively. In this measurement, the tip of the sensor was positioned 5 mm from the feeding point of a 2.45 GHz-band dipole antenna driven by a sinusoidal signal. For the longitudinal field sensor, the dipole antenna was rotated on planes perpendicular to the (100) or (010) planes of the EO crystal, respectively. For the transverse field sensor, the dipole antenna was rotated on a plane parallel to the (1−10) plane. In Fig. 2-20, closed and open circles represent the directivities on the (100) and the (010) planes. The solid line represents the calculated [001]-direction component of the applied electric field at each rotation angle θ. All data are normalized by their maximum values. On both planes, the measured intensities agree with the calculated ones and the cross-axis isolation ratio is over 45 dB. In Fig. 2-21, closed circles and the solid line represent the measured directivities and the electric field intensities calculated to be projected onto the [110]-direction at angle θ of dipole antenna rotation from the [1−10] direction. They are also normalized with the maximum values. The measured intensities agree with the calculated ones and the cross-axis isolation ratio is over 35 dB, which is large enough value to isolate the sensitivity from the null direction. These results demonstrate that it is possible to measure an electric field vector by aligning the sensors orthogonally.

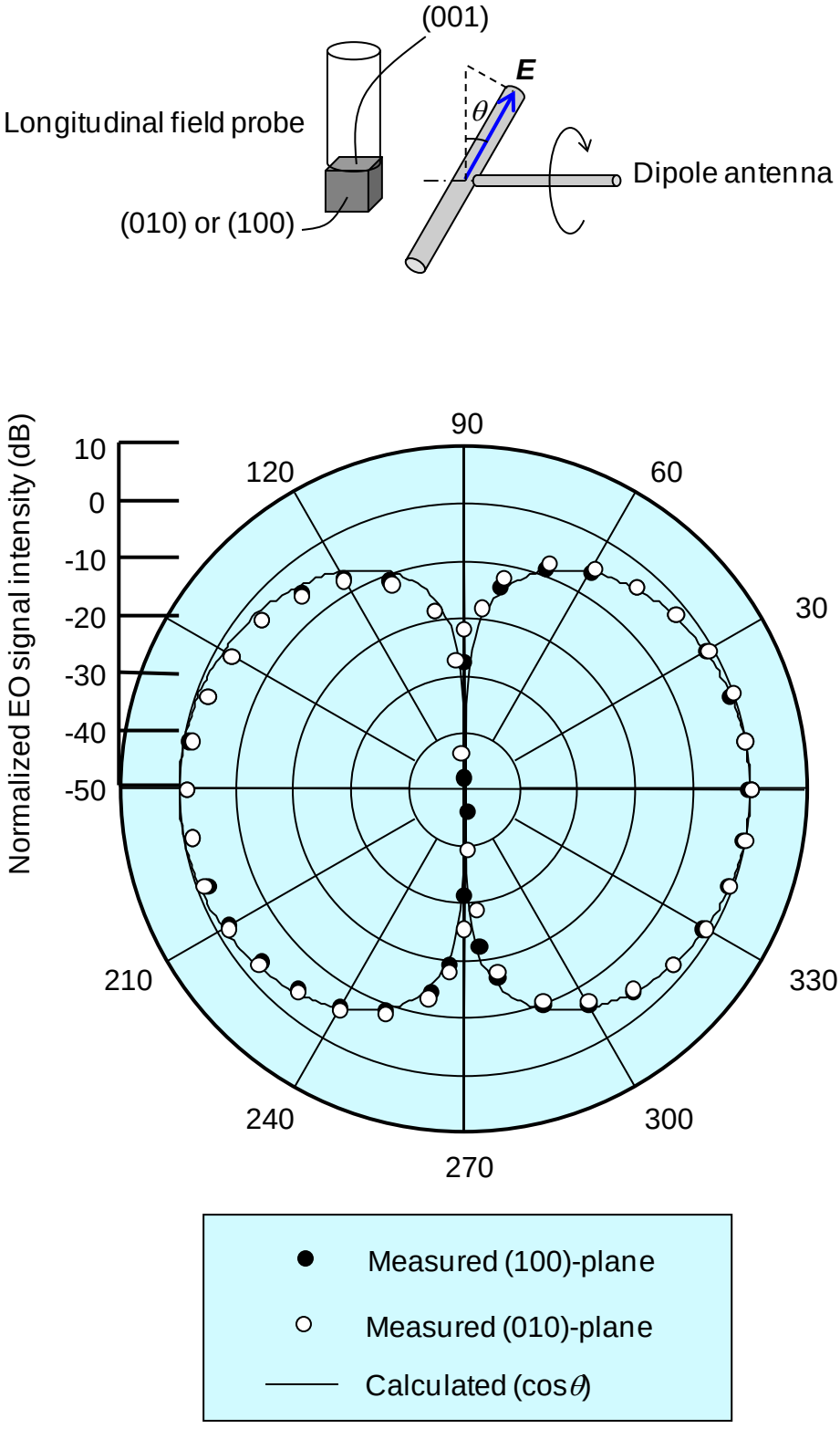

Fig. 2-20. Detectable directivity of longitudinal field sensor.

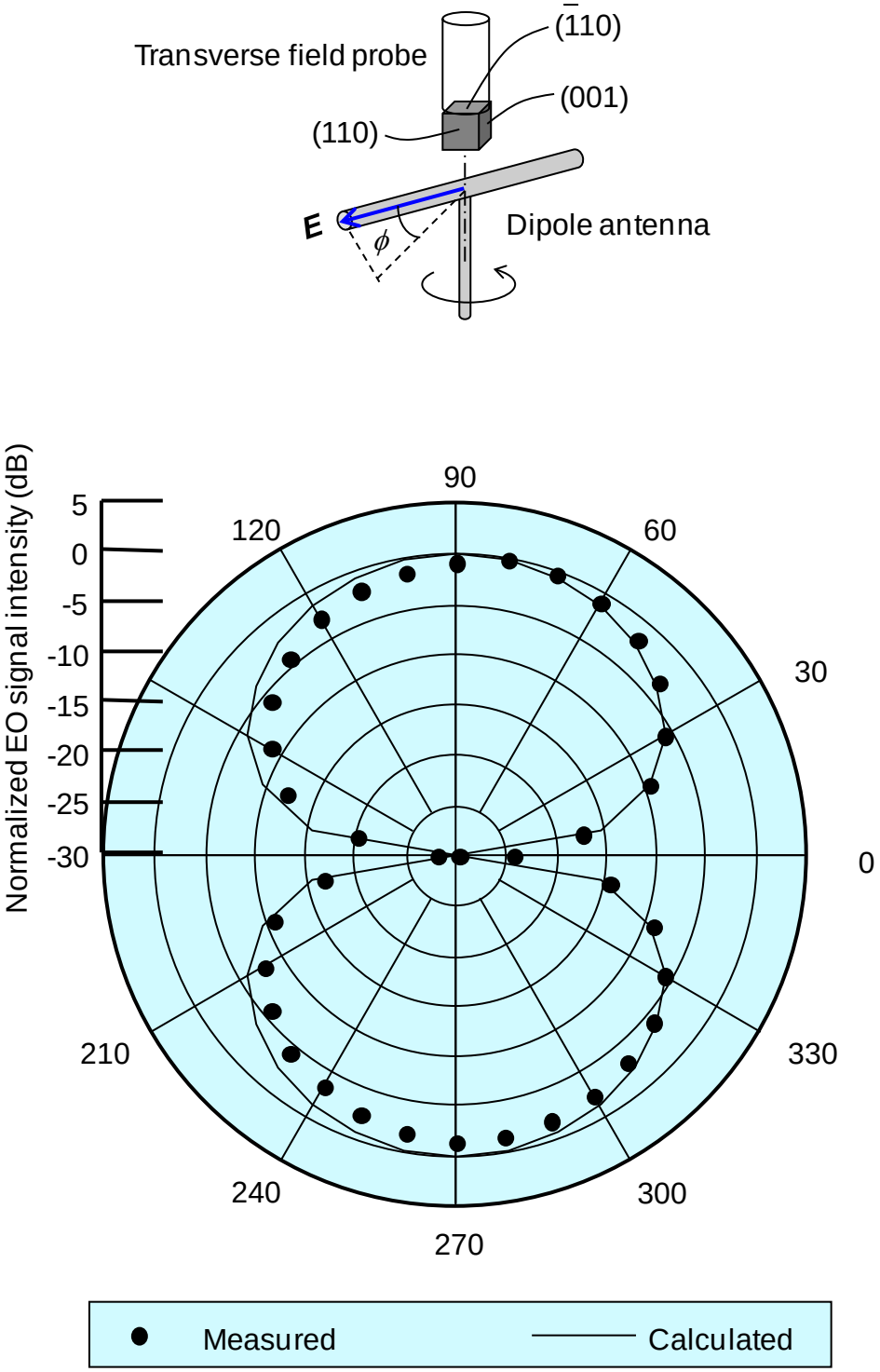

Fig. 2-21. Detectable directivity of transverse field sensor.

D. Frequency response

Fig. 2-22 shows the relationship between the frequency of the applied electric field and the obtained EO signal intensity for the transversal field probe. In this measurement, electric fields were applied to the sensor at frequencies ranging from 1.95 to 6 GHz, and from 16 to 20 GHz using a half-wavelength dipole antenna and a rectangular horn antenna, respectively. The electric field at the EO probe tip was always set to 34 V/m by calibrating the input power to the antennas with a commercially available electric field sensor (NARDA EMC300). The result indicates that the uniformity of the sensitivity is better than ±2 dB from 1.95 to 20 GHz.

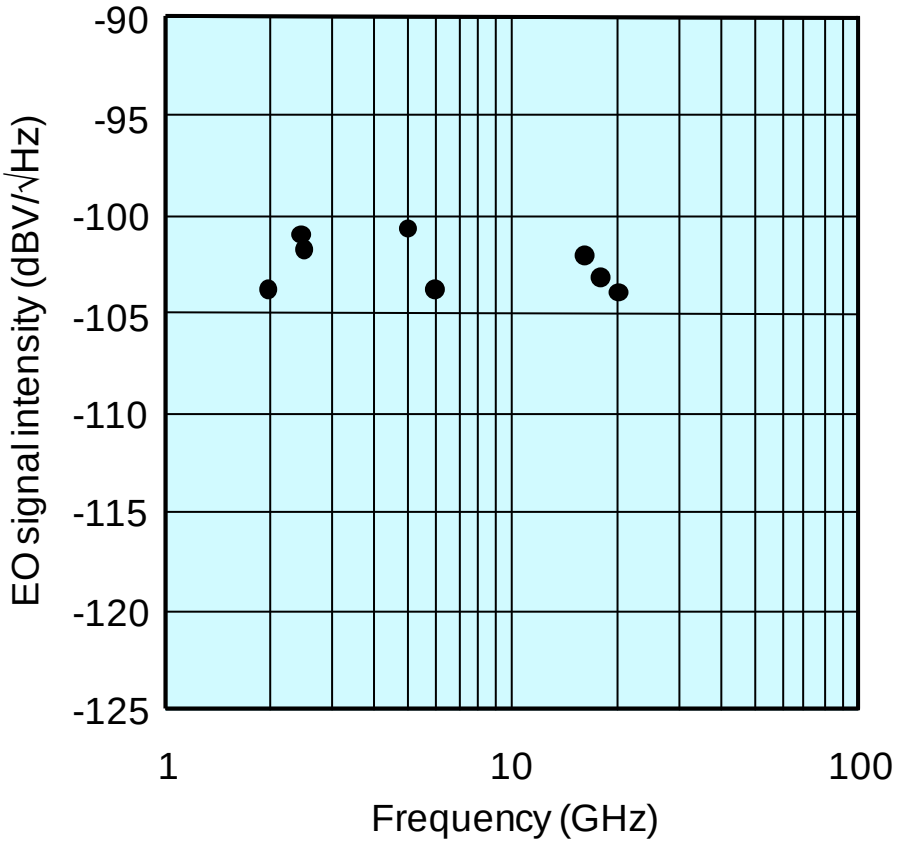

Fig. 2-22. Frequency response of transverse field sensor.

2.4.3 Electric field measurements

A. Near-field measurements around a dipole antenna

The near field was measured around the 2.45 GHz-band dipole antenna using the longitudinal field sensor in the shield box. The sensor was scanned parallel to the radial axis of the dipole antenna while a sinusoidal signal was input from a signal generator to the antenna. The relationship between distance from the dipole antenna and EO signal intensity is shown in Fig. 2-23. Closed circles and a solid line represent measured and calculated intensities normalized by their maximum values. In the near-field region where electro-static and inductive electro-magnetic couplings are dominant, the measured intensities agree with the calculated ones very well. This demonstrates that the sensor can exactly measure a near field around the dipole antenna. In the region over 100 mm from the dipole antenna, the disagreement between the measured and calculated intensities was possibly observed. This is because the computation of the shied box was not included in the calculation. The measured intensities represent a standing wave caused by reflection from the walls of the shield box.

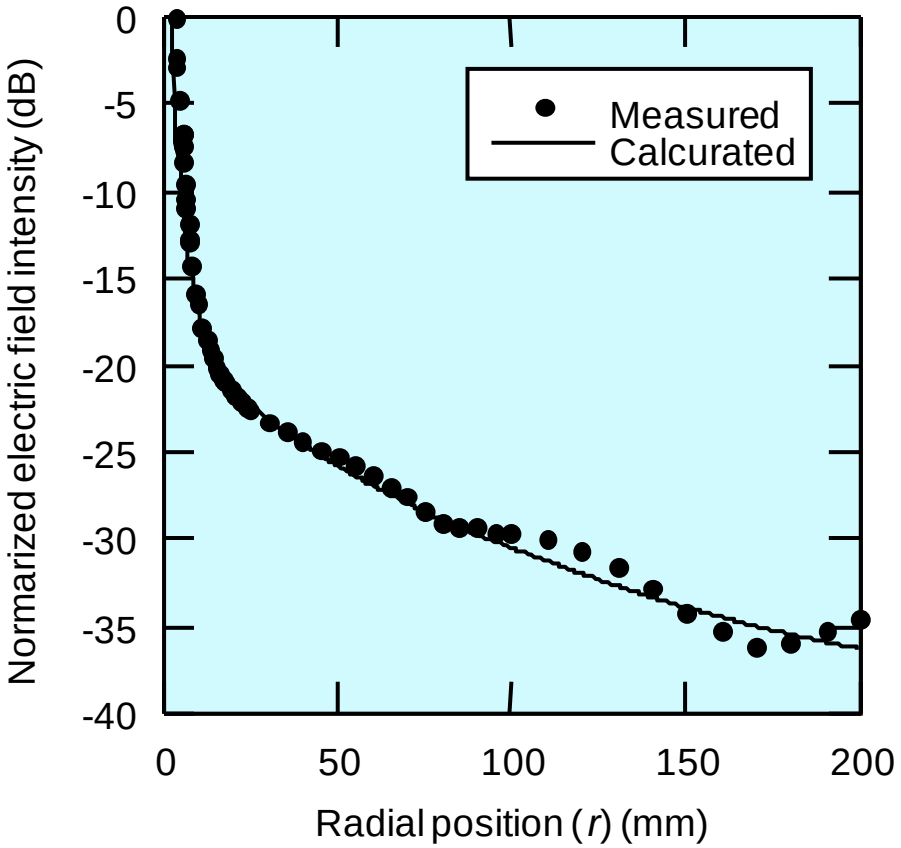

Fig. 2-23. Near field distribution around diploe antenna in free space.

B. Electric-field measurement in tissue-equivalent phantom

A SAR distribution was measured as an example of electric-field measurements using this sensor. The setup for the electric-field measurement in the TEP is shown in Fig. 2-24 [2-32]. A rectangular acrylic case was filled with the TEP and a 2.45 GHz-band dipole antenna was positioned 5 mm below the case. We scanned the transverse field probe parallel and perpendicular to the base of case while RF signal with the power of 17 dBm was fed into the dipole antenna. The intensity and phase of the electric field were obtained using the equivalent sampling method [2-25]. Electric field distributions parallel and perpendicular to the base are shown in Fig. 2-25(a) and (b). Closed and open circles represent the EO signal intensities and phases. The minimum distance from the base is 1 mm, which is less than a fifth of that using a conventional sensor. In a previous experiment using an electric field probe reported by another group, because the electrical coupling between the probe and the base was caused, the differences between the simulated and measured data near the base were obtained [2-33]. To the contrary, the correct data were obtained even when the EO probe was set within 1 mm of the base in this work [Fig. 2-25(b)]. The minimum detectable electric field is less than 0.6 V/m corresponding to the SAR, which satisfies the minimum detection limit [2-34]-[2-36]. These results demonstrate the applicability of the EO probe to SAR measurement.

The phase distribution of the electric field perpendicular to the surface is shown in Fig. 2-25(b). The phase is directly proportional to the distance from the base. From this data, the relative permittivity (ε) and conductivity (σ) of TEP can be calculated. ε and σ calculated to be 41.9 and 1.5 S/m show relatively good agreement with the inherent values of 40.0 and 1.4 S/m at a frequency of 1.95 GHz. When determining SAR, ε and σ of TEP should generally be checked by using specially designed equipment. Figs 7 and 8 indicate that the EO probe can measure SAR, ε, and σ of the TEP at one time, which are very important to obey the regulated rule to measure and improve the qualification of the measurement.

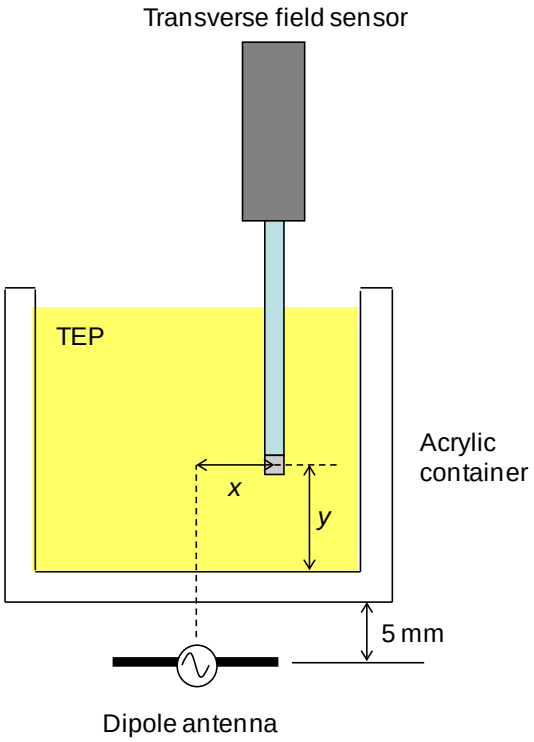

Fig. 2-24. Electric-field measurement system in tissue-equivalent phantom.

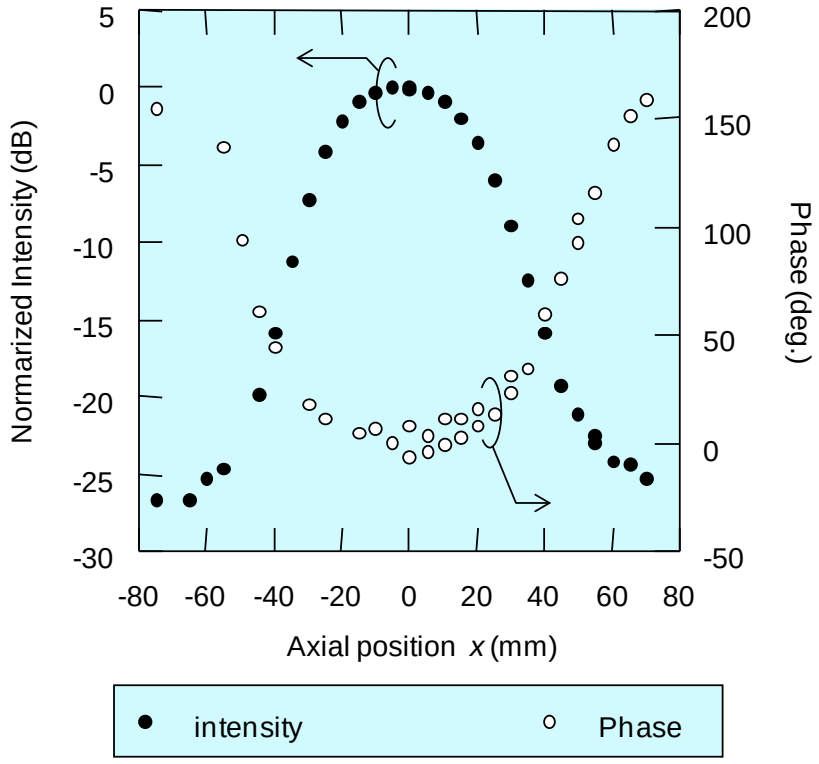

(a)

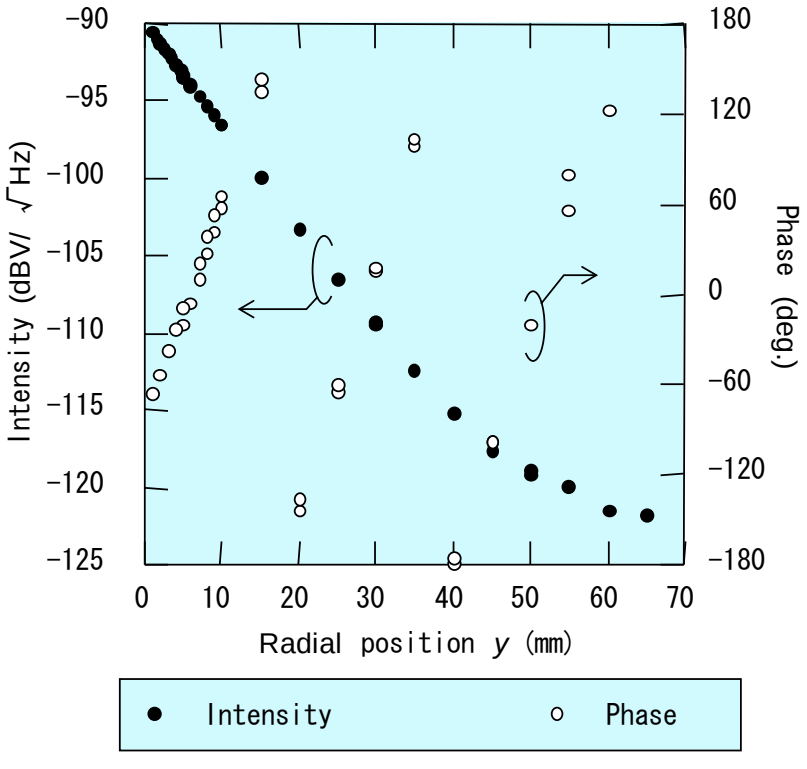

(b)

Fig. 2-25. Electric field distribution in tissue-equivalent phantom parallel (a) and perpendicular (b) to the antenna axis.

2.5 Conclusion

The fiber-mounted sensor contains no metallic components and the EO crystal is fixed on the tip of an optical fiber that connects the crystal to the optical components to eliminate disturbances, such as optical and electrical components, from the near-field range. As a result, electric field measurements can be performed with little invasiveness. I developed longitudinal- and transverse-field probes that detect electric fields orthogonal to each other. The near-field measurement system has a dynamic range of over 45 dB and can detect an electric field of less than 0.6 V/m. The EO probe has excellent directivity with a cross-axis isolation ratio of over 45 dB. A comparison between the measured and calculated near fields around the dipole antenna confirmed that the probe's invasiveness is negligible. As a result, it is possible to conduct SAR measurements with very little invasiveness. The SAR measurement system we developed can detect a SAR of less than 0.5 mW/kg, which satisfies the minimum detection limit stipulated in the regulations. When comparing the SAR measured by the EO probe and a conventional probe, we demonstrated that our system was superior to the conventional probe in determining the SAR near a container's base. This shows that our proposed system has the potential to be used for determining SAR with respect to next generation mobile phones.

References

[2.1] T. Pfeifer, T. Loffler, H. G. Roskos, H. Kurz, M. Singer, and E. M. Biebl, " Electro-optic near-field mapping of planar resonators," IEEE Trans. Antennas Propag., vol.46, no.2, pp.284-291, Feb. 1998.

[2.2] K. Yang, G. David, J. G Yook, I. Papapolymerou, L. P. B. Katehi, and J. F. Whitaker, "Electrooptic mapping and finite-element modeling of the near-field pattern of a microstrip patch antenna," IEEE Trans. Microw. Theory Tech., vol.48, no.2, pp.288-294, Feb. 2002.

[2.3] A. Sasaki and T. Nagatsuma, "Electric-field scanning system using electro-optic sensor," IEICE Trans. Electron., vol.E86-C, no.7, pp.1345-1351, July 2003.

[2.4] K. Sasagawa, A. Kanno, T. Kawanishi, and M. Tsuchiya, "Live electro-optic imaging system based on ultra-parallel photonic heterodyne for microwave near-fields," IEEE Transaction of Microwave Theory and Techniques, vol. 55, pp. 2782-2791, Dec. 2007.

[2.5] M. Shinagawa, T. Nagatsuma, K. Ohono, and Y. Jin, "A real-time electro-optic handy probe using a continuous-wave laser," IEEE Transactions on Instrumentation and Measurement, vol. 50, no. 5, pp. 1076-1080, Oct. 2001.

[2.6] H. Togo, A. Sasaki, A. Hirata, and T. Nagatsuma, “Characterization of millimeter-wave antenna using photonic measurement techniques,” Int. J. RF and Microwave CAS, vol. 14, pp. 290-297, 2004.

[2.7] T. Nagatsuma, N. Sahri, M. Yaita, T. Ishibashi, N. Shimizu, and K. Sato, “All optoelectronic generation and detection of millimeter-wave signals,” in Int. Topical Meeting on Microwave Photon., MB1, Princeton, Oct. 1998.

[2.8] T. Ohara, R. Namiki, K. Igarashi, S. Wakana, and M. Tsuchiya, “Proposal of electro-optic sensor head attached to optical fiber edge,” Technical report of IEICE, MW99-38, pp. 55-60, June 1999.

[2.9] T. Ohara, M. Abe, S. Wakana, M. Kishi, M. Tsuchiya, and S. Kawasaki, “Two-dimensional mapping of microstrip lines with a band pass filter or a photonic bandgap structure by fiber-optic EO spectrum analysis system,” in Int. Topical Meeting on Microwave Photon., WE2. 17, Oxford, Sept. 2000.

[2.10] K. Yang, L. P. B. Katehi, and J. F. Whitaker, “Microwave-field imaging with a fiber-based electro-optic probe,” Proc. Annual Meeting of Laser and Electro-Optics Society, TuFF3, pp.388-389, Puerto Rico, Nov. 2000.

[2.11] S. Wakana, T. Ohara, M. Abe, E. Yamazaki, M. Kishi, and M. Tsuchiya, “Fiber-edge electrooptic/magnetooptic probe for spectral-domain analysis of electromagnetic field,” IEEE Trans. Microwave Theory Tech., vol. 48, pp. 2611-2616, Dec. 2000.

[2.12] H. Togo, T. Onishi, K. Kiminami, N. Shimizu, T. Nagatsuma, S. Uebayashi, "Tip-on-fiber electro-optic probe for specific absorption rate measurement," in Proc. AP-MWP 2006, Kobe, Japan, April, 2006, pp. 238-241.

[2.13] H. Togo, N. Shimizu, and T. Nagatsuma, "Near-field mapping system using fiber-based electro-optic probe for specific absorption rate measurement," IEICE Trans. Electronics , Vol.E90-C, No.2, 2007.

[2.14] F. Pockels, Lehrbuch der Kristalloptik, Leipzig: Teubner, 1906.

[2.15] J. Kerr, Phil. Mag., vol. 3, p. 321, 1877.

[2.16] J. Kerr, Phil. Mag., vol. 5, p. 161, 1878.

[2.17] H. Futama, and R. Pepinsky, “Optical activity in ferroelectric LiH3(SeO3)2,” J. Phys. Soc. Jap., vol. 17, p. 725, 1962.

[2.18] L. V. Keldysh, “Behaviour of Non-Metallic Crystals in Strong Electric Fields,” J. Exptl. Theoret. Phys. (USSR), vol. 33, pp. 994-1003, 1957.

[2.19] Mark Fox, Optical properties of solid, Oxford, New York, 2001.

[2.20] Mansoor Sheik-Bahae, Nonlinear Optics Basics. Kramers–Kronig Relations in Nonlinear Optics, in: Robert D. Guenther (Ed.): Encyclopedia of Modern Optics, Academic Press, 2005.

[2.21] I. P. Kaminow and E. H. Turner, “Elecrooptic light modulators,” Applied Optics, vol. 5, no. 10, pp. 1612-1628, 1966.

[2.22] J. A. Valdmanis and B. Mourou, “Subpicosecond electro-optic sampling: principles and applications,” IEEE J. Quantum Electron., vol. 22, pp. 69-78, 1986.

[2.23] K. J. Weingarten, M. J. W. Rodwell, and D. M. Bloom, “Picosecond optical smapling of GaAs integrated circuits,” IEEE J. Quantum Electron., vol. 24, no. 2, pp. 198-220, 1988.

[2.24] P. Y. Han and X-C. Zhang, “ Coherent, broadband midinfrared terahertz beam sensors,” Appl. Phys. Lett., vol. 73, pp. 3049-3051, 1998.

[2.25] A. Sasaki, and T. Nagatsuma, “Millimeter-wave imaging using an electrooptic detector as a harmonic mixer,” IEEE J. Sel. Top. Quantum Electron., vol. 6, pp. 735- 740, 2000.

[2.26] Q. Wu, and X–C. Zhang, “Design and characterization of traveling-wave electrooptic terahertz sensors,” IEEE J. Sel. Top. Quantum Electron., vol. 2, pp. 693-700, 1996.

[2.27] W. Joseph, and L. Martens, “The influence of the measurement probe on the evaluation of electromagnetic fields,” IEEE Trans. Electromagn. Compat., vol. 43, pp. 339-349, 2003.

[2.28] A. Hirata, H. Ishii, and T. Nagatsuma, “Design and characterization of millimeter-wave antenna for integrated photonic transmitter,” IEEE Trans. Microw. Theory Tech., vol. 49, pp. 2157-2162, 2001.

[2.29] N. Sahri, and T. Nagatsuma, “Application of 1.55-mm photonic technologies to practical millimeter-wave network analyzer,” Photon. Technol. Lett., vol. 12, pp. 1307-1311, 1999.

[2.30] N. Kuwabara, K. Tajima, R. Kobayashi, and F. Amemiya, “Development and analysis of electric field sensor using LiNbO3 optical modulator,” IEEE Trans. Electromagnetic Compatibility, vol. 34, no. 4, pp. 391 – 396, 1992.

[2.31] B. G. Loader, M. J. Alexander, W. Liang, and S Torihata, ”An Optical Electric Field Probe for Specific Absorption Rate Measurements,” 15th International Zurich Symposium on Electromagnetic Compatibility, 12C3, pp.57-60, Zurich, Switzerland, 2003.

[2.32] T. Onishi, H. Togo, N. Shimizu, K. Kiminami, S. Uebayashi, and T. Nagatsuma, “SAR measurement employing electro-optic (EO) probe without using metal,” in A joint meeting BioEM2005, Dublin, Ireland, June 2005.

[2-33] T. Schmid, O. Egger, and N. Kuster, “Automated E-field scanning system for dosimetric assessments,” IEEE Trans. Microwave Theory Technol., vol. 44, no. 1, pp. 105 – 113, January 1996.

[2-34] ICNIRP, “ Guidelines for limiting exposure to time-varying electric, magnetic, and electromagnetic fields (up to 300 GHz),” Health Physics., vol. 74, no. 4, pp. 494 – 522, Apr. 1998.

[2-35] IEEE standard for safety levels with respect to human exposure to radio frequency electromagnetic fields, 3 kHz to 300 GHz, ANSI/IEEE Standard C95.1-1991, Apr. 1992.

[2-36] “Radio-radiation protection guidelines for human exposure to electromagnetic fields,” Telecommunication Technology Council, Ministry Posts Telecommunication, Deliberation Rep. 89, Tokyo, Japan, 1997 (in Japanese).

Chapter 3

Flexibility enhancements

3.1 Introduction

The bulk-crystal-based sensors are used for characterizing antennas and circuits because of their small electro-magnetic invasiveness [3.1]-[3.5]. Since fiber-mounted sensors are free from disturbances created by metal components such cables and antennas around a detection area, the distribution of the near field radiated from a microstrip antenna and a line can be precisely measured [3.3], [3.4]. However, since the polarization plane of light transmitted through an optical fiber changes when the fiber is bent, and because of temperature fluctuation, the sensitivity of the fiber-mounted sensor changes during long-term measurements with large scanning areas. In previous experiments, antennas under test were scanned over the fiber-mounted sensor [3.3], and the scanning area was smaller than 10 mm square even though the fiber-mounted sensor could be scanned over the antennas [3.4]. To stabilize the sensitivity, I have developed a fiber-mounted sensor where the optical fiber is fixed inside a thin glass tube [3.6], [3.7]. I scanned the developed fiber-mounted sensor near a 2-GHz-band dipole antenna, and precisely measured the electric field distributions in an area larger than a 20-cm cube, which is necessary to evaluate the antenna. However, the length of the fixed optical fiber was only several tens of centimeters.

To enhance the flexibility, a highly stable bulk-crystal-based sensor was mounted on the tip of a flexible optical fiber with a length as long as several meters [3.8], [3.9]. the mechanism of the sensitivity degradation was clarified to be caused by fiber bending and temperature fluctuation, and a passive sensitivity-stabilization technique based on compensation of the polarization-mode-dispersion change was introduced in the fiber using a Faraday rotator (FR). This technique is based on the polarization-rotated reflection (PRR) method [3.10]. The PRR method was initially proposed for stabilizing the temperature performance of light intensity modulators by the bidirectional use of an EO crystal for the effective cancellation of its birefringence. Enokihara et al. applied this method to magnetic-field and temperature sensors attached to a fiber tip with free-space optics [3.11]. Here the first application of this method to a fiber-mounted sensor and the integration of PRR optical components on the fiber tip are reported.

This chapter explains the operating mechanism of the fiber-mounted sensor with the PRR method and describes the basic properties.

3.2 Sensitivity stabilization scheme

A side view of the fiber-mounted sensor and a block diagram of the electric field measurement system are shown in Fig. 3-1(a) and (b), respectively. The sensor tip contains an EO crystal with a dielectric mirror, an FR [3.12], a collimating lens, a ferrule and a 5-m-long polarization maintaining fiber (PMF). Since CdTe is used as the EO crystal, there is no static birefringence and the band gap energy is larger than that of the sampling light at a wavelength of 1550 nm. As a result the light passes through the crystal without any polarization change at the state free from electric field. That is, the sensitivity of the crystal does not change with changes in temperature. The crystal axis is set as the crystal probes the electric field in a transverse direction to that of the light transmitted in the crystal. The cross-sectional dimension of the EO crystal is 1 mm x 1 mm. The sensor is attached to a polarization control module through the PMF. The polarization control module comprises a beam splitter (BS), half and quarter-wave plates (WPs), a polarization beam splitter (PBS), a photodiode (PDs), and a lens.

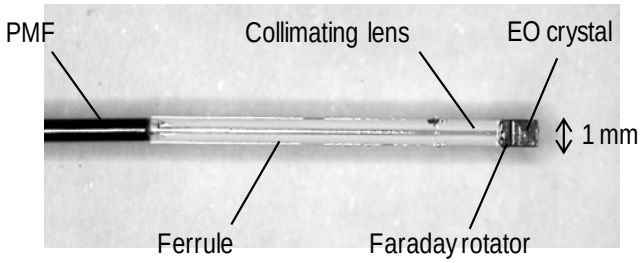

(a)

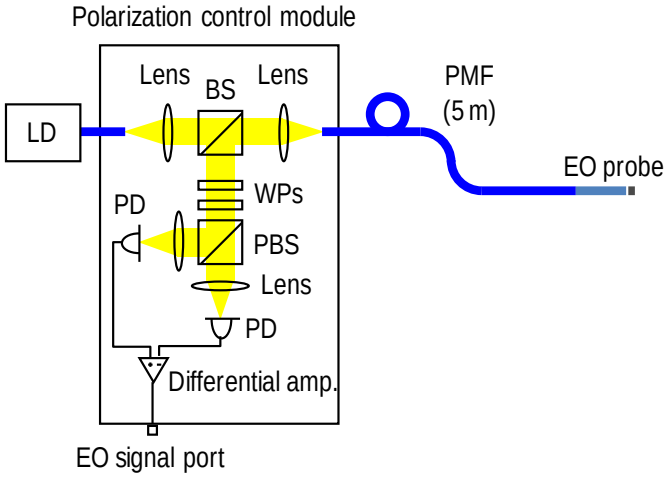

(b)

Fig. 3-1. Tip (a) and system configuration of flexible fiber-mounted sensor (b).

Linearly polarized light emitted from a laser diode (LD) is input into the PMF through the polarization control module. The light is delivered to the EO crystal and reflected by the dielectric mirror. When an electric field is applied to the EO crystal, birefringence is induced and the polarization of the light propagating through the EO crystal is changed. The polarization change is proportional to the electric-field intensity. That is, the light is polarization-modulated at the EO crystal. The polarization-modulated light is returned to the polarization control module and converted to intensity-modulated light with the analyzer. The intensity-modulated light is detected and output as a replica of the electric field by the PD. The output signal I_{out} is expressed as

$$I_{\mathrm{out}} \propto 2\cos\left(\frac{\Gamma_{\mathrm{eo}}}{2}+\Gamma_{\mathrm{f}}+\Gamma_{\mathrm{b}}\right)\sin\left(\frac{\Gamma_{\mathrm{eo}}}{2}\right)\sin(2\phi), \tag{3.1}$$

where Γ_{eo}, is the phase difference induced by the EO effect in the EO crystal, Γ_{f} and Γ_{b} are the phase differences caused by PMF bending and temperature fluctuation during forward transmission to the crystal and backward transmission to the polarization control module, and ϕ is the azimuth of the linearly polarized light inserted into the PMF. Equation (3.1) shows that the output signal changes that result from PMF bending and temperature fluctuation during scanning even if the applied electric field is constant. The phase difference during transmission in the PMF is induced by modal birefringence, which is the static birefringence caused by the differences between the stresses along the slow and fast axes in the PMF. Since the modal birefringence ΔB changes as a result of PMF bending and temperature fluctuation, the phase difference also changes, and is expressed as

$$\Gamma_i = \frac{2\pi l \Delta B}{\lambda}, \tag{3.2}$$

where l and λ are the length of the PMF and the wavelength, and i is f or b. When using PANDA fiber [3.13] as a PMF, the dependence of the modal birefringence in the PMF ΔB_{bend} and ΔB_{temp} on PMF bending and temperature fluctuation are expressed as

$$\Delta B_{\mathrm{bend}} = \frac{a^2}{2R^2} Y(C_2 - C_1), \tag{3.3}$$

$$\Delta B_{\mathrm{temp}} = (C_1 - C_2)\frac{2Y(\alpha_3 - \alpha_2)\Delta T}{(1-\nu)}\left(\frac{d_1}{d_2}\right)^2\left\{1-3\left(\frac{d_2}{a}\right)^4\right\}, \tag{3.4}$$

where a is the radius of the cladding, R is the bending radius as the PMF is bent along a plane parallel to the slow axis and the light transmission direction, Y is Young's modulus, C_1 and C_2 are the photoelastic constants on the slow and fast axes, α_2 and α_3 are the thermal coefficients in normal and stress-applying parts, ΔT is the temperature change, ν is Poisson's ratio, d_1 is the radius of the stress-applying parts, and d_2 is the center position of the stress-applying parts on the slow axis [3.14], [3.15]. The sensitivity dependence on PMF bending and temperature fluctuation is obtained by substituting (3.3) and (3.4) into (3.2), and then substituting (3.2) into (3.1). The output signal dependence on PMF bending in a commercially available PANDA fiber is shown in Fig. 3-2. The EO signal is flat for bending radii larger than 10 mm, and abruptly decreases when the bending radius is less than 6 mm. The output signal dependence on the temperature fluctuation in a 5-m-long PMF is shown in Fig. 3-3. The EO signal decreases to less than -10 dB with a temperature change of 0.2 degrees Celsius.

The stabilization scheme with PRR is as follows. Since the FR rotates the polarization plane orthogonally in a round trip, lights transmitted along the fast and slow axes of the PMF are exchanged at the sensor tip. As the round trip time is negligible compared with the phase change period, the amplitudes of the phase differences Γ_f and Γ_b are the same. Since the signs of the phase differences are opposite ($\Gamma_f = -\Gamma_b$), the phase differences are canceled out. As the intensities of the light transmitted along the fast and the slow axes are the same ($\phi = \pi/4$), the output signal is maximized. The output signal I_{out} is expressed as

$$I_{out} \propto \sin\Gamma_{eo} . \tag{3.5}$$

The output signal is unaffected by either the PMF bending or the temperature fluctuation, and so the sensitivity is stable. In this sensor, a magnetized Faraday Rotator has a coercive force of larger than 32 kA/m (400 Oe) even though MRI uses a static magnetic field of less than 1 kA/m, the sensitivity is stable in general electric-field measurements of the SAR measurement and the antenna measurement for mobile phone and wireless LAN terminals.

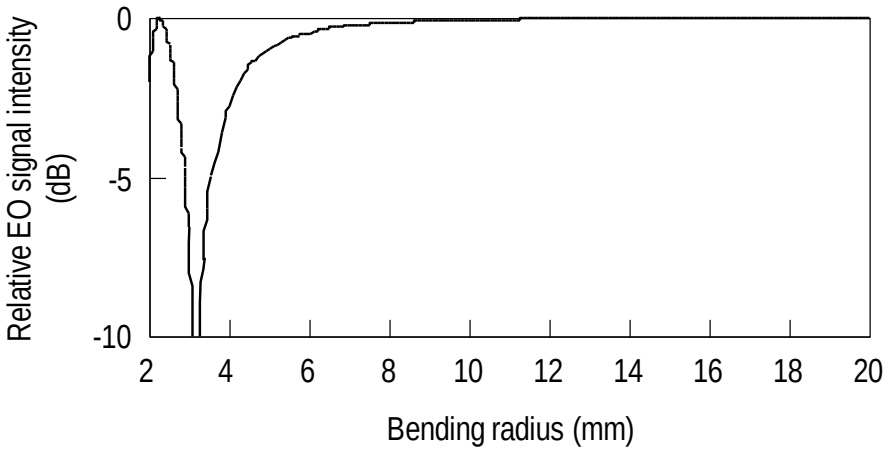

Fig. 3-2. Sensitivity dependence on PMF bending with various radii.

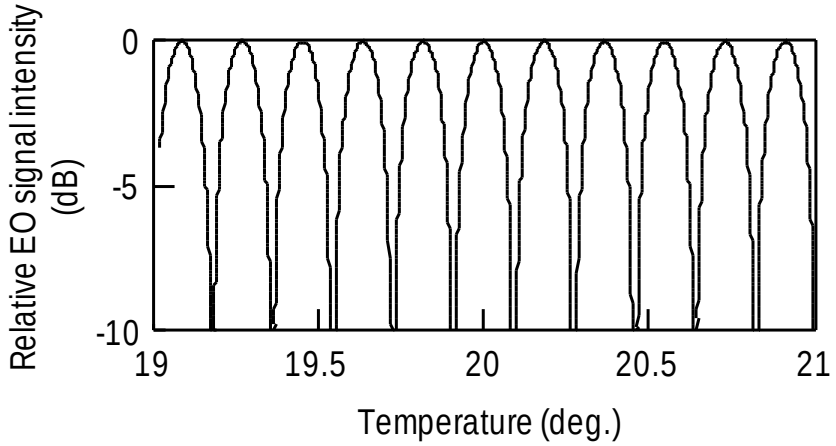

Fig. 3-3. Sensitivity dependence on temperature fluctuation around sensor with 5-m-long PMF

3.3 Basic properties

3.3.1 Sensitivity

We evaluated the detection sensitivity of the fiber-mounted EO probe at 2, 4 and 8 GHz. The sensitivity was measured using an electric field produced over a coplanar waveguide (CPW) under the following conditions: The crystal was positioned to measure the electric field parallel to the surface of the CPW. The center of the crystal was kept at a distance of 0.5 mm from the top surface of the CPW at the center of the gap between the signal and the ground line of the CPW, while the signal generator input a sinusoidal signal into the CPW. The CPW gap is 0.1 mm, which is the same as the diameter of the light beam propagating in the crystal. The electric field intensity was

measured by the equivalent sampling method [3.16], [3.17] using a 20-ps-wide optical pulse generated with a 1.55-μm DFB-LD at a repetition frequency of 2 GHz + 20 kHz. The PD has a frequency bandwidth of up to 2 MHz, which corresponds to the maximum detectable frequency of 100 GHz. The relationship between the CPW input power and the EO signal intensities is shown in Fig. 3-4, where the filled and open circles and crosses represent the EO signal intensity measured at 2, 4 and 8 GHz, respectively. The noise floor is the same in the measurement at each frequency. The sensitivity at each frequency is the same and linearly proportional to the power supplied to the antenna with a dynamic range of over 50 dB.

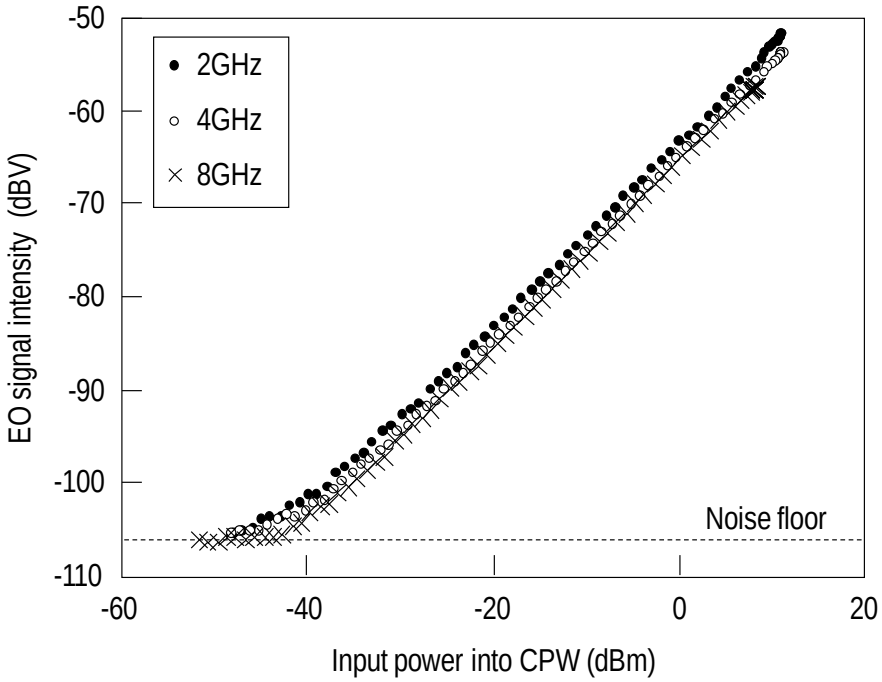

Fig.3-4. Relationship between input power into the CPW and the EO signal intensity at frequencies of 2, 4, and 8 GHz.

3.3.2 Stability

I placed the sensor tip over the gap of the CPW, to which we supplied a sine-wave signal at 2 GHz. I then measured the output signal. The output signal dependence on PMF bending is shown in Fig. 3-5. The filled and open circles and the line represent the output signal of our previous fiber-mounted sensor without the FR, that with the new sensor with the FR, and that without the FR calculated with Equations (3.1), (3.2) and (3.3). The PMF was wound once around a cylinder with various radii. The output signal of our previous sensor without the FR decreases abruptly with a radius of less than 10 mm, which is different from the calculated result. This is because

bending-induced stress is applied to the slow and fast axes in the PMF. In contrast, the signal with the FR is flat and the fluctuation is less than 0.5 dB with radii larger than 4 mm. The temperature dependence of the output signals is shown in Fig. 3-6, where the filled and open circles and the line represent the output signal of our previous sensor without the FR, that of the developed sensor with the FR, and that without an FR calculated with Equations (3.1), (3.2) and (3.4). A 10-cm section of the 5-m-long PMF was heated from 50 to 100 degrees Celsius. The output signal of our previous sensor without the FR follows the temperature change and fluctuates with an amplitude greater than 10 dB. In contrast, the signal with the FR is stable, with a fluctuation of less than 1 dB. Time domain fluctuation at room temperature is shown in Fig. 3-7. Since the PMF is static, the output signal is stable with a fluctuation of less than 0.3 dB. Moreover, in another experiment, the phase of the output signal is stable with a fluctuation of less than 5 degrees for 10 hours.

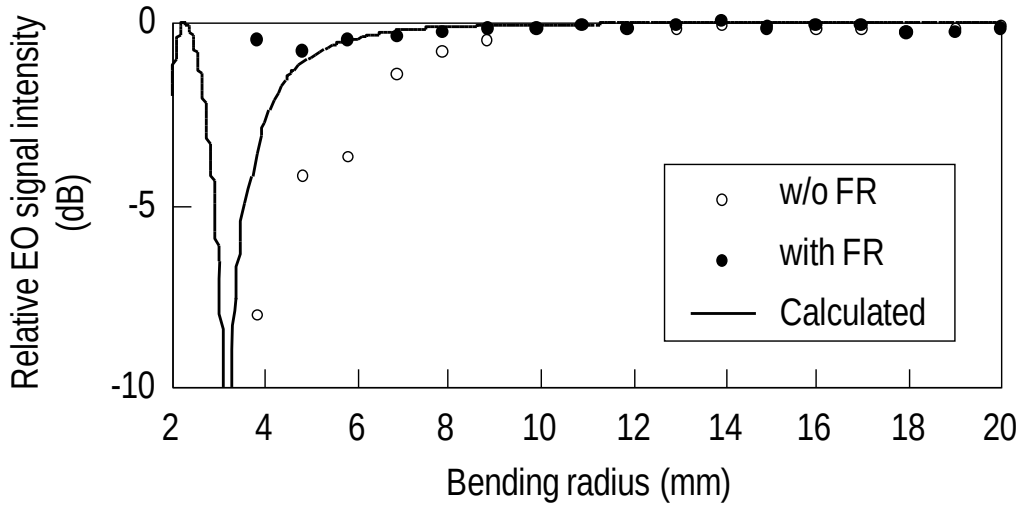

Fig.3-5. Dependence of EO signal on PMF bending with various radii.

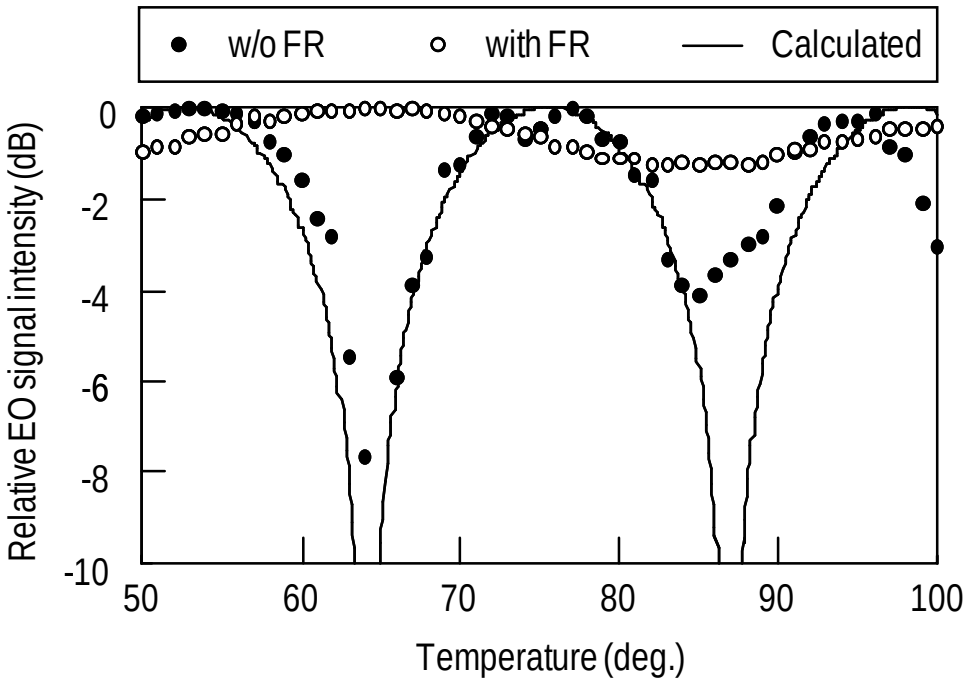

Fig. 3-6. Dependence of EO signal on temperature change.

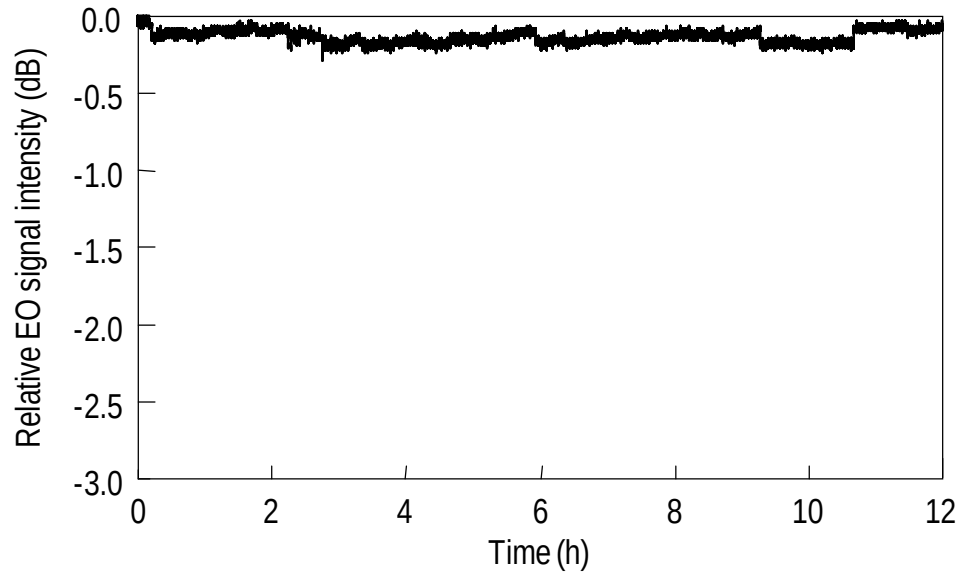

Fig. 3-7. Stability of EO signal without PMF bending at room temperature in 12 hours.

3.3.3 Directivity

In this measurement, the probe tip was positioned 5 mm from the feeding point of a 2-GHz-band dipole antenna driven by a sinusoidal signal. The dipole antenna was rotated on planes parallel and vertical to the light propagation axis in the PMF. The directivity of the developed sensor is shown in Fig. 3-8, where the filled and open circles represent the directivity on the planes parallel and vertical to the light axis, and the line represents the projection of the electric field at each rotation angle θ, which corresponds to the directivity of a small dipole antenna. All values are normalized by their maximum values. The measured and calculated intensities agree well and the cross-axis isolation ratio is over 30 dB, which is large enough to isolate the sensitivity from the null direction. These results indicate that the directivity is not affected by mounting the FR in the PRR method.

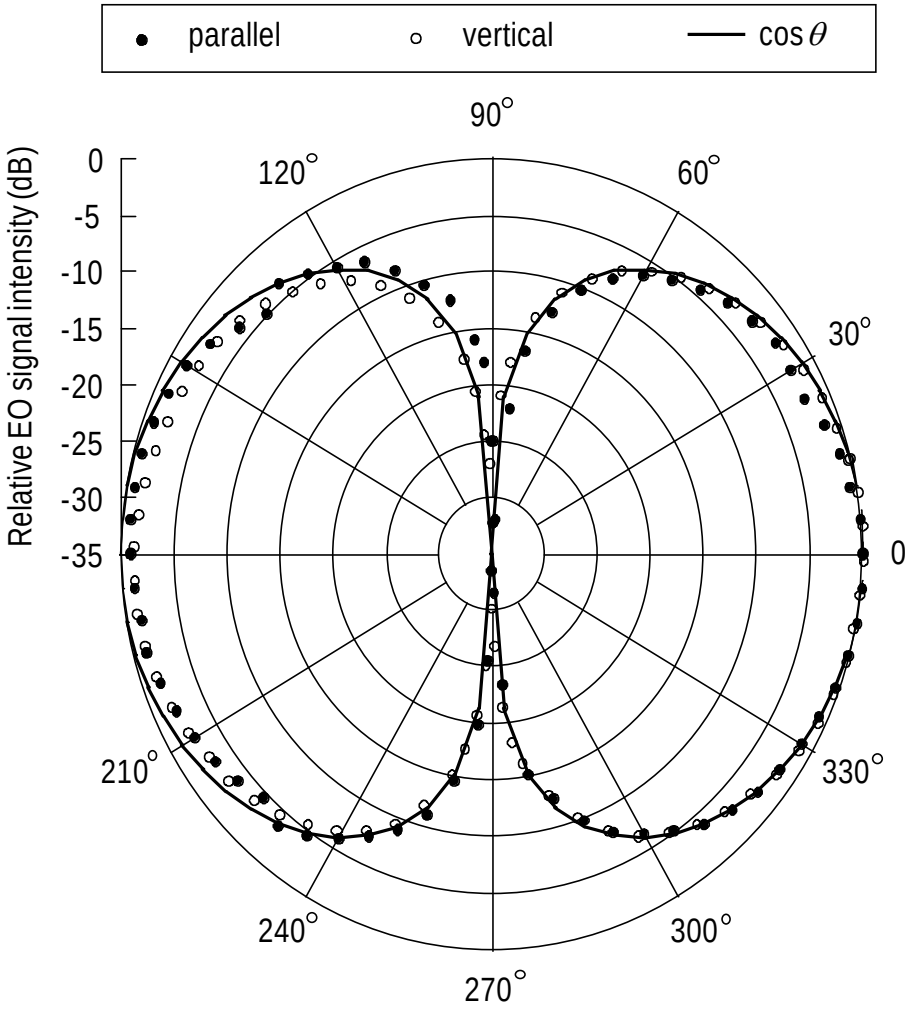

Fig. 3-8. Detectable directivity of developed fiber-mounted sensor with FR.

3.4 Conclusion

An electric-field vector measurement system employs scanning with a sensitivity-stabilized fiber-mounted sensor. In this system, a polarization-rotated reflection method is used to suppress the sensitivity fluctuation caused by fiber bending during scanning, thus enabling large-area measurements. Since the properties (e.g. sensitivity and directivity) of a longitudinal and transverse-detection probe are the same, a combination of the electric fields measured with each probe provides the electric-field vector. The intensity and phase distribution of the electric fields measured on each orthogonal axis represent an asymmetric shape of a planer circuit with a Vivaldi antenna, which cannot be calculated by the simulation with an ideal model. The vector spatial field calculated from the measured electric field shows the electric-field dynamics above and around the planar circuit. Consequently, the visualization of the vector spatial field based on measurements obtained with the fiber-mounted sensor provides intuitive analyses and diagnoses of circuit and antenna performance.

References

[3.1] K. Kamogawa, I. Toyoda, K. Nishikawa, and T. Tokumitsu, “Characterization of a monolithic slot antenna using an electro-optic sampling technique,” IEEE Microwave and Guided Wave Lett., vol. 4, pp. 414–416, Dec. 1994.

[3.2] T. Pfeifer, T. Loffler, H. G. Roskos, H. Kurz, M. Singer, and E. M. Biebl, “Electro-optic near-field mapping of planar resonators,” IEEE Trans. Antennas Propag., vol. 46, no. 2, pp. 284–291, Feb. 1998.

[3.3] K. Yang, G. David, J. G. Yook, I. Papapolymerou, L. P. B. Katehi, and J. F. Whitaker, “Electrooptic mapping and finite-element modeling of the near-field pattern of a microstrip patch antenna,” IEEE Trans. Microw. Theory Tech., vol. 48, no. 2, pp. 288–294, Feb. 2002.

[3.4] S. Wakana, T. Ohara, M. Abe, E. Yamazaki, M. Kishi, and M. Tsuchiya, “Fiber-edge electrooptic/magnetooptic probe for spectral-domain analysis of electromagnetic field,” IEEE Trans. Microw. Theory Tech., vol. 48, no. 12, pp. 2611–2616, Dec. 2000.

[3.5] N. Hidaka, K. Kobayashi, H. Sugama, R. Usui, Y. Tanabe, and O. Hashimoto, “Log-periodic dipole antenna array-type optical electric field sensor,” IEICE Trans. Electron., vol. E88-C, no. 1, pp. 98–104, Jan. 2005.

[3.6] H. Togo, T. Onishi, K. Kiminami, N. Shimizu, T. Nagatsuma, and S. Uebayashi, “Tip-on-fiber electro-optic probe for specific absorption rate measurement,” in

Proc. AP-MWP 2006, pp. 238–241, April 2006.

[3.7] H. Togo, N. Shimizu, and T. Nagatsuma, "Near-field mapping system using fiber-based electro-optic probe for specific absorption rate measurement," IEICE Trans. Electron., vol. E90-C, no. 2, pp. 436–442, Feb. 2007.

[3.8] H. Togo, N. Shimizu, and T. Nagatsuma, "Fiber-Mounted Electro-Optic Probe with Highly Stable Sensitivity," in 19th IEEE LEOS Annual Meeting Conference, Octorber, 2006, pp. 414-415.

[3.9] H. Togo, N. Kukutsu, N. Shimizu, and T. Nagatsuma, "Sensitivity-stabilized fiber-mounted electrooptic probe for electric field mapping," Journal of Lightwave Technology , Vol.26, No.15, pp.2700-2705, 2008.

[3.10] K. Goto, T. Sueta, and T. Makimoto, "Traveling-wave light-intensity modulators using the method of polarization-rotated reflection," IEEE. J. Quantum Electron., vol. QE-8, no. 6, pp. 486–493, Jun. 1972.

[3.10] A. Enokihara, M. Isutsu, and T. Sueta, "Optical fiber sensors using the method of polarization-rotated reflection," Journal of Lightwave Technology, vol. LT-5, no. 11, pp. 1584–1590, Nov. 1987.

[3.11] D. N. Payne, A. J. Barlow, and J. J. R. Hansen, "Development of low- and high-birefringence optical fibers," IEEE J. Quantum Electron., vol. QE-18, no. 4, pp. 477–488, 1982.

[3.12] T. Hosaka, K. Okamoto, T. Miya, Y. Sasaki, and T. Edahiro, "Low-loss single-polarization fibers with asymmetrical strain birefringence," Electron. Lett., vol. 17, no. 15, pp. 530–531, 1981.

[3.13] V. J. Fratello, S. J. Licht, C. D. Brandle, and R. G. O'Connor, "Nucleation induced coercivity in Faraday rotator garnets," Proceedings of International Symposium on Laser and Nonlinear Optical Material, 1997, T. Sasaki, editor, pp. 59–66.

[3.14] T. Hosaka, Y. Sasaki, and K. Okamoto, "3 km-long single-polarization single mode fiber," Electron. Lett., vol. 21, no. 22, pp. 1023–1024, Oct. 1985.

[3.15] J. Noda, K. Okamoto, and Y. Sasaki, "Polarization-maintaining fibers and their applications," Journal of Lightwave Technology, vol. LT-.4, no. 8, pp. 1071–1089, Aug. 1986.

[3.16] A. Sasaki and T. Nagatsuma, "Millimeter-wave imaging using an Electrooptic detector as a harmonic mixer," IEEE J. Sel. Top. Quantum Electron. vol. 6, pp. 735–740, 2000.

[3.17] H. Togo, A. Sasaki, A. Hirata, and T. Nagatsuma, "Characterization of millimeter-wave antenna using photonic measurement techniques," Int. J. RF and Microwave CAS, vol. 14, pp. 290–297, 2004.

Chapter 4

Sensitivity enhancements

4.1 Introduction

The potential of the optical sensor was demonstrated in the SAR measurements using a tissue equivalent phantom in the chapter 2 [4.1]. In the demonstration, I used CdTe, which has the highest sensitivity coefficient among inorganic EO crystals. However, it takes several hours to map the electric-field distribution in a human head and a full-body phantom for the SAR measurement. Since the measurement time is reduced in inverse proportion to the detection sensitivity, a highly sensitive sensor is required in order to improve the throughput of the SAR measurement. Moreover, the power density radiated from 3G mobile phone is lower than that from 2G phone which was used in the above demonstrations. Therefore, higher sensitivity enhancement has to be satisfy the requirements in the regulation for SAR measurement of 3G or more next generation mobile telecommunication techniques.

A promising material for improving the detection sensitivity is 4-dimethylamino-N-methylstilbazolium tosylate (DAST) because of its large electrical contribution to the EO effects and low dielectric constant [4.2], [4.3]. Recently, Adachi et al. have achieved the growth of large-aperture DAST crystal with high quality and reproducibility [4.4]. DAST has been proposed for fast EO applications, such as picosecond pulse and terahertz detections [4.5]. Moreover, DAST is a good insulator, so that it is promising for electric-field detection at an extremely low frequency (ELF) band. However, the birefringence induced by the optical biaxiality of DAST may affect the directivity and stability of the sensor.

This chapter theoretically explains the principle of the electric-field detection with DAST and the fiber-mounted optical sensor with the DAST crystal [4.6], [4.7] and describes the configuration of the fiber-mounted sensor with the DAST crystal fabricated with specified techniques, and presents the sensitivity enhancement in free-space electric-field detection.

4.2 DAST sensor

DAST is an extremely promising material with excellent characteristics summarized in Table 1 [4.2], [4.3]. DAST is an optical biaxial crystal that belongs to the space group of Cc. Its EO coefficient is 10 times larger than that of CdTe, which has the largest coefficient among inorganic crystals [4.8]. DAST is not only less invasiveness than CdTe but also highly efficient to apply the electric field to its inside because of the small reflection and diffraction due to its small permittivity. This means that DAST is good for detecting the electric field in free space. Its sensitivity factor is 3 times higher than that of CdTe. Moreover, DAST is a good insulator. And it should be possible to improve the low-frequency response by preventing screen-out due to the contribution from electrical carriers.

Table. 4-1. Characteristics of DAST at the wavelength of 1535 nm and CdTe at the wavelength of 1000 nm.

Material	**DAST**	**CdTe**
Optical feature	Biaxial	Isotropic
EO coefficient (pm/ V)	$r_{11} = 47, \quad r_{21} = 21, r_{21} << 1$	$r_{41} = 4.5$
Refractive index	$n_1 = 2.13, \quad n_2 = 1.60, n_3 \sim 1.00$	$n = 2.84$
Relative Permittivity	$\varepsilon = 5.2$	$\varepsilon = 9.4$
Sensitivity factor	$\lvert r_{11}n_{13} - r_{21}n_{23} \rvert / \varepsilon = 71$	$2r_{41}n_3 / \varepsilon = 22$
Resistivity (Ω/m)	$10^{12} - 10^{13}$	$\sim 10^{9}$

A side view of the fiber-mounted sensor with the DAST crystal is shown in Fig. 4-1. The sensor tip contains the DAST crystal, a reflector, a collimating lens, a ferrule, and an optical fiber. The cross-sectional dimension of the crystal is 1 x 1 mm, which is as small as that of the CdTe crystal integrated in the previous sensor [4.1]. The sensor tip is covered with a thin resin with alkaline and acid durability to be degraded with the TEP during SAR measurements.

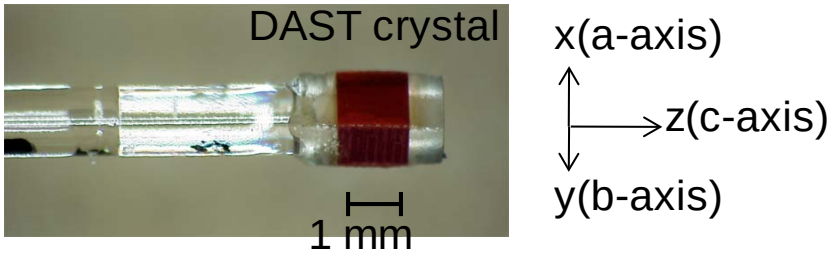

Fig. 4-1. Tip of fiber-mounted sensor with the DAST crystal.

To provide the maximum sensitivity, linearly polarized light is injected at an angle of 45 degrees with respect to the a- and b-axes, which are shown as the x- and y-axes in Fig. 4-1. As electric field E_1, E_2 and E_3 are applied to the a-, b- and c-axes respectively, the retardation Γ induced by the EO effect is expressed as

$$\Gamma = \Gamma_1 + \Gamma_2 + \Gamma_3 \tag{5.1}$$

$$\Gamma_1 = \frac{2\pi L}{\lambda}\left(n_1 - n_2 - {n_1}^2 + {n_2}^2\right) \tag{5.2}$$

$$\Gamma_2 = \frac{\pi L}{\lambda}\left(r_{11}{n_1}^3 - r_{22}{n_2}^3\right)E_1 \tag{5.3}$$

$$\Gamma_3 = \frac{2\pi L}{\lambda}\left(\frac{{n_1}^2{n_2}^2\left({n_1}^2 - {n_2}^2\right){r_{62}}^2 E_2}{1 - {n_1}^2{n_2}^2{r_{62}}^2 E_2}\right) \tag{5.4}$$

$$n_i \propto \Delta T \quad (i=1, 2), \tag{5.5}$$

where L is the crystal length, λ is the wavelength, n_1 and n_2 are the refractive indexes along the a- and b-axes, r_{11}, r_{21}, r_{62} are the EO tensor elements at position 11, 21, and 62, and ΔT is the temperature change, respectively. The Γ_1 is the static retardation of the crystal, and Γ_2 and Γ_3 are the EO contributions induced with electric field E_1 and E_2. Since ${r_{62}}^2 << 1$, Γ_3 is negligible, which means that the optical electric-field sensor detects only the electric field along the a-axes. Since the refractive index is proportion to the temperature, the retardation changes due to the temperature change, which can degrade the stability of the sensitivity.

4.3 Basic properties

4.3.1 Invasiveness

The electric field was calculated around the fiber-mounted sensor with DAST and a typical small dipole antenna for the SAR measurement in the TEP using the finite integration method. The calculated region was a rectangular parallelepiped 50-mm high and 200-mm long. The electromagnetic wave was a plane wave oscillated at 1.95 GHz and propagated in the +z direction. Periodic boundary conditions were assigned on planes orthogonal to the propagation direction and a perfectly matched layer was assigned on the output plane. The E-planes of the electric field (each

10 mm × 10 mm) around the optical sensor and the dipole antenna are shown in Figs. 4-2(a) and (b). The degree of intensity is displayed as a grayscale image. The disturbance around the sensor is much smaller than that around the dipole antenna. The electric-field distribution on the line A-A' in Fig. 4-2(a) is shown in Fig. 4-3. There is little disturbance in the region more than 1-mm away from the optical sensor. This shows that the optical sensor can precisely measure the electric field adjacent to the antenna of the device under test for the SAR measurement, which is difficult with the small dipole antenna.

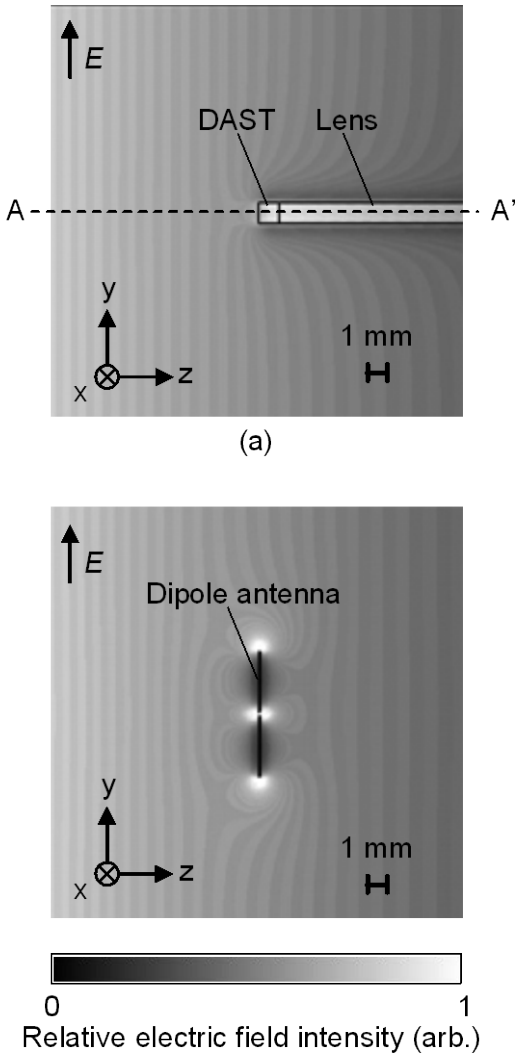

Fig. 4-2. Calculated electric-field distribution around the optical electric-field sensor with DAST (a) and small dipole antenna (b) in tissue-equivalent phantom.

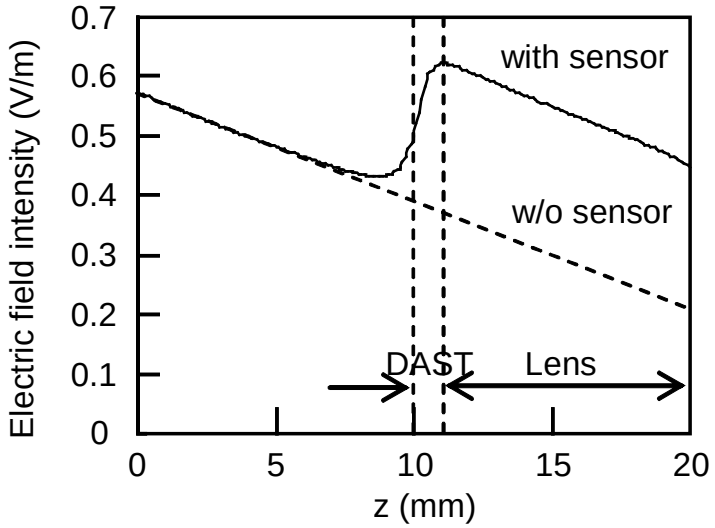

Fig. 4-3. Electric-field distribution along the propagating direction (A-A' in Fig. 4-2(a)).

4.3.2 Sensitivity

The detection sensitivity of the DAST-based sensor and compared the results was evaluated comparing with the previous CdTe-based one. The sensitivity of the sensors was measured using an electric field radiated in free space from a half-wavelength dipole antenna (Anritsu MA5612B4). The center of DAST was kept at a distance of 5 mm from the feeding point of the dipole antenna, while the signal generator input a sinusoidal signal with a frequency of 2.45 GHz to the dipole antenna. The relationship between the antenna input power and the EO signal intensities is shown in Fig. 4-4, where the circles and squares respectively represent the EO signal intensity measured with the DAST- and CdTe-based sensors. The noise floor was the same in the measurement system with both sensors. The sensitivity of the DAST-based sensor is 6-dB higher than that of the CdTe-based one. The difference of the sensitivities is smaller than that calculated from the theoretical comparison of the sensitivity factors, because the sensitivity of the CdTe-based sensor is much higher than that calculated theoretically, as we experimentally know. Moreover, the sensitivities are linearly proportional to the antenna input power with the dynamic range of over 35 dB.

The sensitivity of the DAST-based sensor in the ELF band is shown in Fig. 4-5. The uniformity of the sensitivity is better than 3 dB at frequency ranging from 40 Hz to 10 kHz, where the CdTe-based sensor cannot detect the electric field. The response of electric devices, such as photodiodes and amplifiers, with cut-off frequency of 40 Hz affects the sensitivity of the sensor at a few ten hertz.

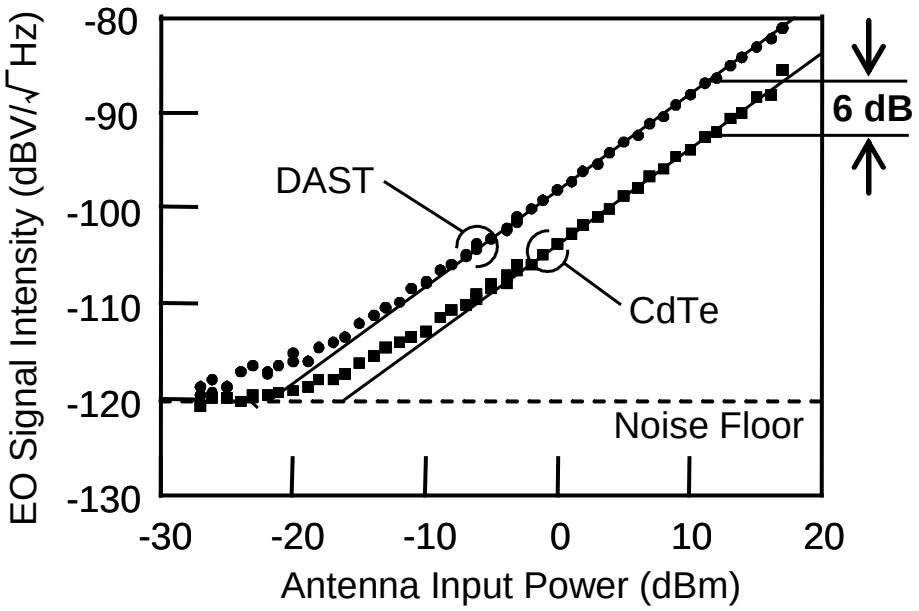

Fig. 4-4. Relationship between antenna input power and EO signal intensity in DAST- and CdTe-based sensors.

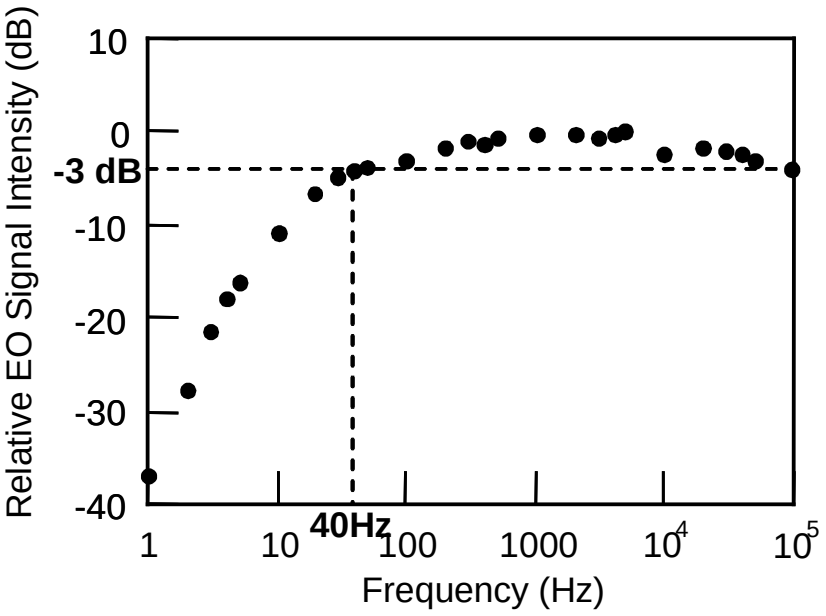

Fig. 4-5. Sensitivity of the DAST-based sensor in the ELF band.

4.3.3 Stability

The stability of the sensitivity at 2.45 GHz is shown in Fig. 4-6. The stability of the sensitivity at 2.45 GHz is shown in Fig. 4-6. In the graph, the sensitivity of the DAST-based sensor monotonically keeps decreasing with the fluctuation of less than 0.5 dB for one hour. This is due to the change of the birefringence of the DAST crystal, which is induced by the surrounding temperature change of about 2 °C. Since the surrounding temperature is controlled within the fluctuation smaller than ±2 °C in the standardized SAR measurement, the sensitivity fluctuation is calculated to be less than ±0.5 dB which is as small as the conventional electrical sensor.

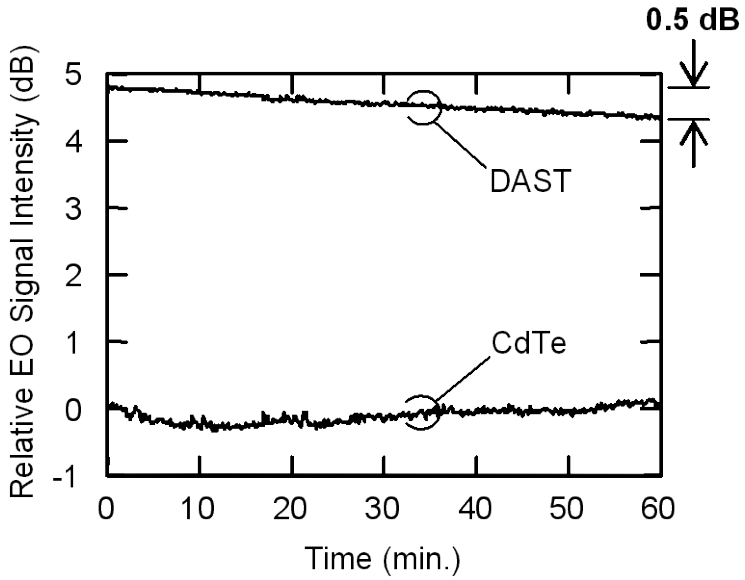

Fig. 4-6. Sensitivity stability for one hour at room temperature.

4.3.4 Directivity

In this measurement, the sensor tip was positioned 5 mm from the feeding point of a 2.45-GHz-band dipole antenna driven by a sinusoidal signal. The dipole antenna was rotated on planes perpendicular to the c and b-axes of the DAST crystal. The directivity of the DAST-based sensor is shown in Fig. 4-7, where the circles and squares represent the directivities on the plane perpendicular to the c and b-axes, respectively. The solid line represents the calculated a-axial direction component of the applied electric field at each rotation angle θ. All data are normalized by their maximum values. On both planes, the measured intensities agree with the calculated ones and the cross-polarization discrimination ratio is over 30 dB, which is high enough to isolate sensitivity from the null direction.

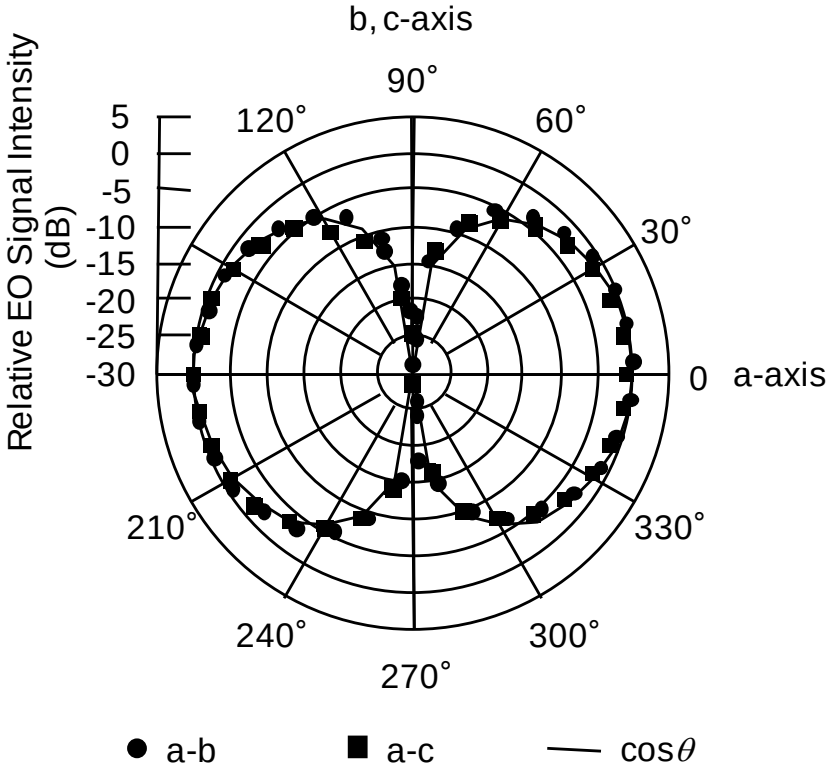

Fig. 4-7. Directivity of the DAST-based sensor.

4.4 Conclusion

A fiber-mounted sensor containing a 1-cubic-millimeter DAST crystal was developed for improving the sensitivity and a detectable bandwidth in ELF band. The sensitivity is much higher than that of our previous CdTe-based probe, even though CdTe provides the highest sensitivity among inorganic crystals. This means that the measurement time can be greatly decreased. The stability and directivity are good enough for practical SAR measurements. Moreover, the sensitivity is very high in the ELF band, which the CdTe-based sensor does not cover. Those results demonstrate that the DAST-based probe is a promising tool for SAR measure-ments and electromagnetic compatibility tests in the ELF band.

References

[4.1] T. Onishi, H. Togo, N. Shimizu, K. Kiminami, S. Uebayashi, and T. Nagatsuma, “SAR measurement employing electro-optic (EO) probe without using metal,” in A joint meeting BioEM2005, Dublin, Ireland, June 2005.

[4.2] J. W. Perry, S. R. Marder, K. J. Perry, and E. T. Sleva, “Organic salts with large electro-optic coefficients,” in Nonlinear Optical Properties of Organic Materials IV, K. Singer, ed., Proc. Soc. Photo-Opt. Instrum. Eng., vol. 1560, p. 302, 1991.

[4.3] F. Pan, G. Knopfle, C. Bosshard, S. Follonier, R. Spreiter, M. Wong, and P. Gunter, “Electro-optic properties of the organic salt 4-N, N- dimethylamino-4’-N’-methyl -stilbazolium tosylate,” Appl. Phys. Lett., vol. 69, p. 13, 1996.

[4.4] H. Adachi, K. Nagaoka, F. Tsunesada, M. Yoshimura, Y. Mori, T. Sasaki, A. Sasaki, T. Nagatsuma, Y. Ochiai, and N. Fukasaku, “High-quality organic 4-dimethylamino-N-metyl-4-stibazolium tosylate (DAST) crystal for electro-optic measurement applications,” Tech. Dig. MWP 2002, pp. 85-88, Nov. 2002.

[4.5] P. Y. Han, M. Tani, F. Pan, and X. C. Zhang, “Use of the organic crystal DAST for terahertz beam applications,” Opt. Lett., vol. 25, p. 675, 2000.

[4.6] H. Togo, H. Uchida, H. Yokota, A. Izumi, S. Fukasaku, T. Nagatsuma, and N. Fukasaku, "Highly sensitive optical electric-field sensor using DAST," in 2007 Asia Pacific Mi- crowave Photonics Conference, Jeju Island, 2007.

[4.7] H. Togo, H. Uchida, H. Yokota, A. Izumi, T. Nagatsuma, and N. Fukasaku, "Highly Sensitive Optical Electric-Field Sensor Using DAST and Its Applications," Proceeding of European Microwave Association, , vol. 4, no. 4, 2008.

[4.8] C. S. Namba, “Electro-optical effect of zincblende,” J. Opt. Soc. Am. B, vol. 51, p. 76, 1961.

Chapter 5

Antenna measurements

5.1 Introduction

Chapters 3 and 4 describe the configurations and the basic properties of the flexible fiber-mounted sensor based on PRR method and the highly sensitive fiber-mounted sensor with the DAST crystal. The flexible fiber-mounted sensor can precisely measure electric field without invasiveness and stably remote-access measuring points with the optical fiber with a length over 1 km. Therefore, the flexible fiber-mounted sensor is promising for the ideal antenna measurement as shown in chapter 1. The sensitivity of the DAST-based sensor is 6-dB higher than that of the CdTe-based sensor at a microwave band. The DAST-based sensor has the potential to decrease the measuring time considered in chapter 1. This chapter describes an application of the flexible and highly sensitive fiber-mounted sensor described in chapters 3 and 4 to electric-field measurements. The flexible sensor is applied to near-field measurements which most highly require less invasiveness into electric field and the sensitivity stability of the sensor, and accomplishes the 2-dimentional measurement with 3-axis electric-field components which is agree well with simulations. Moreover, this chapter presents higher performances of the highly sensitive sensor in an SAR measurement for a mobile phone than those of the CdTe-based sensor. The highly sensitive sensor also represents the potential of practical use in EMC measurements at ELF band where the CdTe-based sensor cannot detect any electric field.

5.2 Near-field measurement with flexible fiber-mounted sensor

5.2.1 Measurement system

The flexible fiber-mounted sensor tip and the setup of an antenna measurement system are shown in Fig. 5-1 (a) and (b). The sensor tip is connected to the polarization controller with 5-m-long PMF. A linearly polarized light is input from the DFB-LD with PMF and the intensity-modulated lights are output into the differential amplifier with SMFs. Fig. 5-2(a) and (b) show the whole setup and 2-dimentinal (2D) stage of the antenna measurement system. The antenna measurement system comprises the 2D stage mounted on an optical instrument rack and stage controller. The optical instrument stores the polarization controller, the DFB-LD, the PDs,

and the differential amplifier. The sensor tip is attached to the arm mounted on 2D stage. The scanning area of the sensor is 20 x 20 cm with 200 μm-spatial resolution. The inside wall of the system is covered with electromagnetic absorbers to reduce the reflection from the wall. The manual manipulator vertically positions the sensor tip with a 10 μm-spatial resolution.

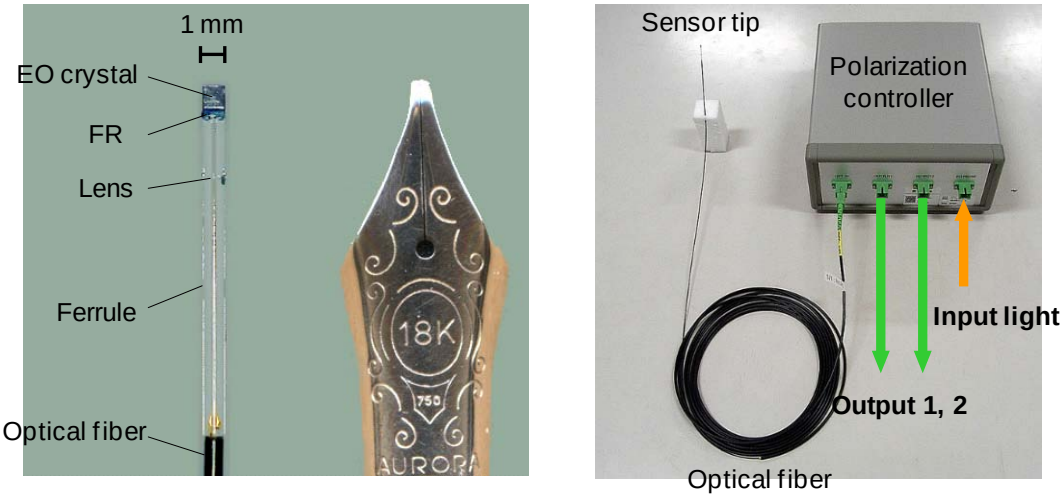

(a) (b)

Fig. 5-1. Flexible fiber-mounted sensor tip (a) and setup of electric-field measurement system.

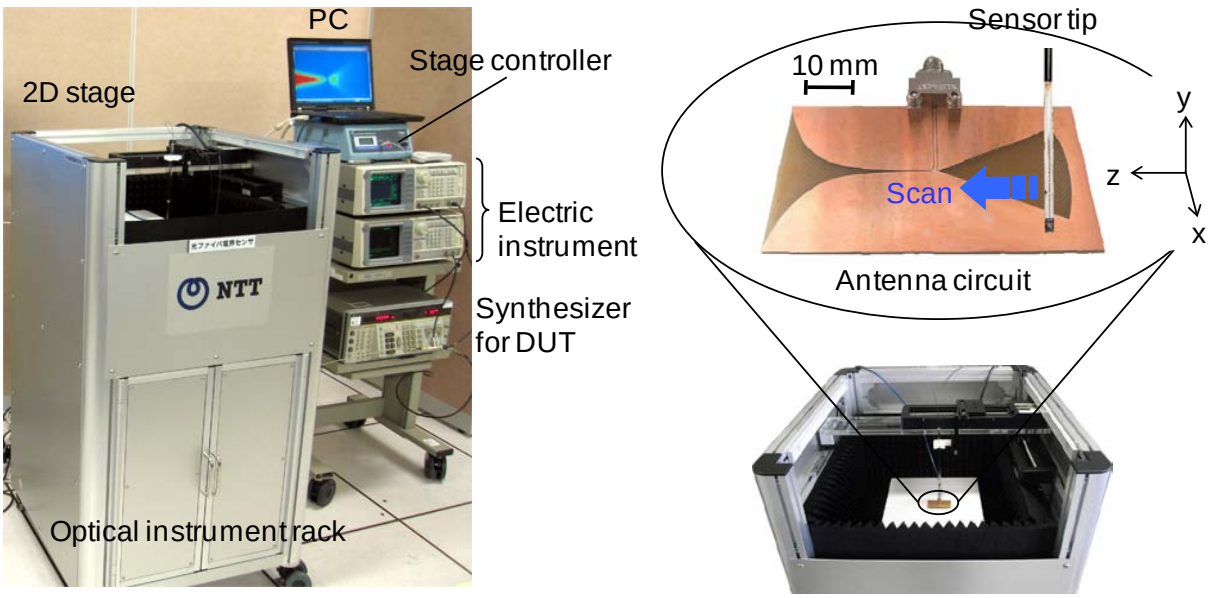

(a) (b)

Fig. 5-2. Whole setup (a) and 2-dimentional stage of antenna measurement system (b).

5.2.2 2D mapping of electric field

The sensor was scanned in the area of 150 mm x 50 mm at a distance of 1 mm above a planar circuit with a CPW, a radial balun and a Vivaldi antenna as shown in Fig. 5-3(a) [5.1]. The CPW and the radial balun were fabricated with a 20-μm-thick Cu film on a 0.8-mm-thick glass-epoxy wafer. The planar circuit was attached to the adapter transiting the CPW from a coaxial cable to which the sine-wave signal was supplied at 8 GHz. For comparison, a commercially available electromagnetic simulator (MW-Studio/ CST GmbH) calculated the electric field with the model shown in Fig. 5-3(b). The measured and calculated near-field intensity and phase distributions are shown in Figs. 5-4 and 5-5, respectively. The electric-field components parallel to the x, y and z-axes are shown in (a), (b) and (c) of both figures, respectively. The intensity and phase distributions measured with the EO probe agreed with the calculated distributions very well, except for the intensity distribution of the electric field parallel to the z-axis and the phase distribution of the electric field parallel to the y-axis. In the intensity of the electric field parallel to the z-axis, asymmetric distributions were measured over the Vivaldi antenna and the radial balun, which was not observed in the simulation. The phase parallel to the y-axis could not be measured out of the circuit because the intensity of the electric-field radiating for the -x direction is too small to be detected with the EO probe.

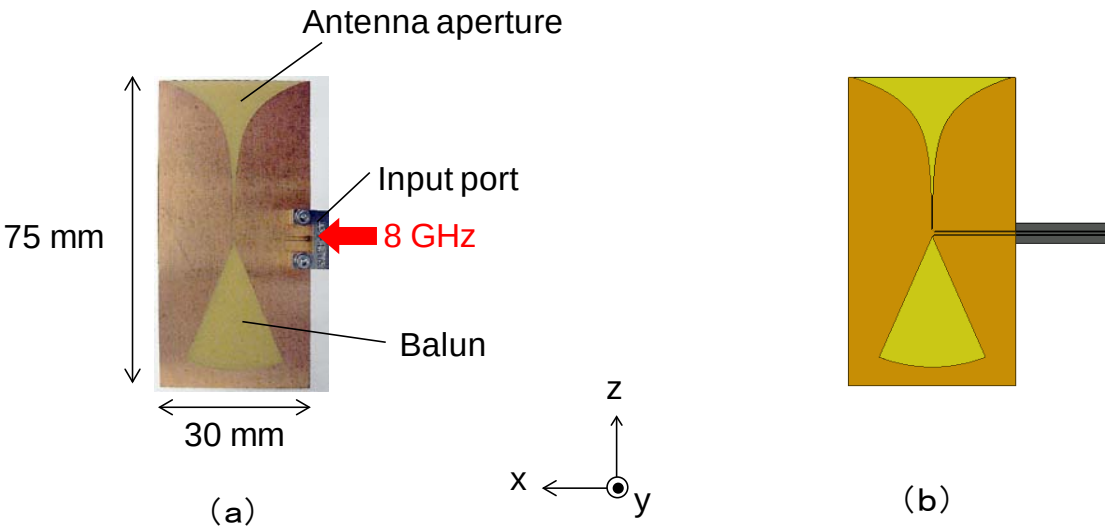

Fig. 5-3. Measured planar antenna circuit (a) and model for simulation.

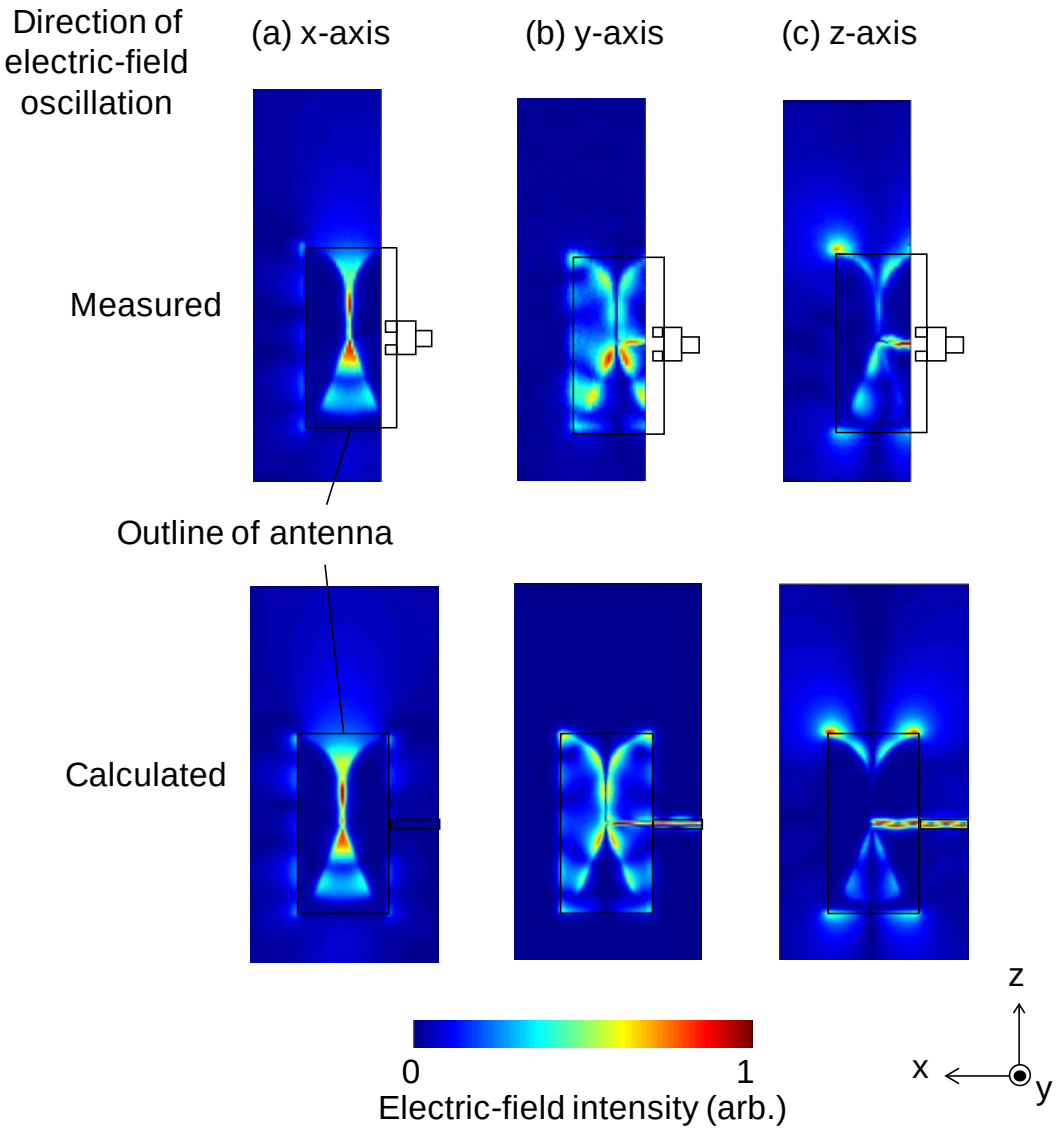

Fig. 5-4. Near-field intensity distributions above and around the planar antenna circuit (a) with E_x, (b) with E_y, and (c) E_z components.

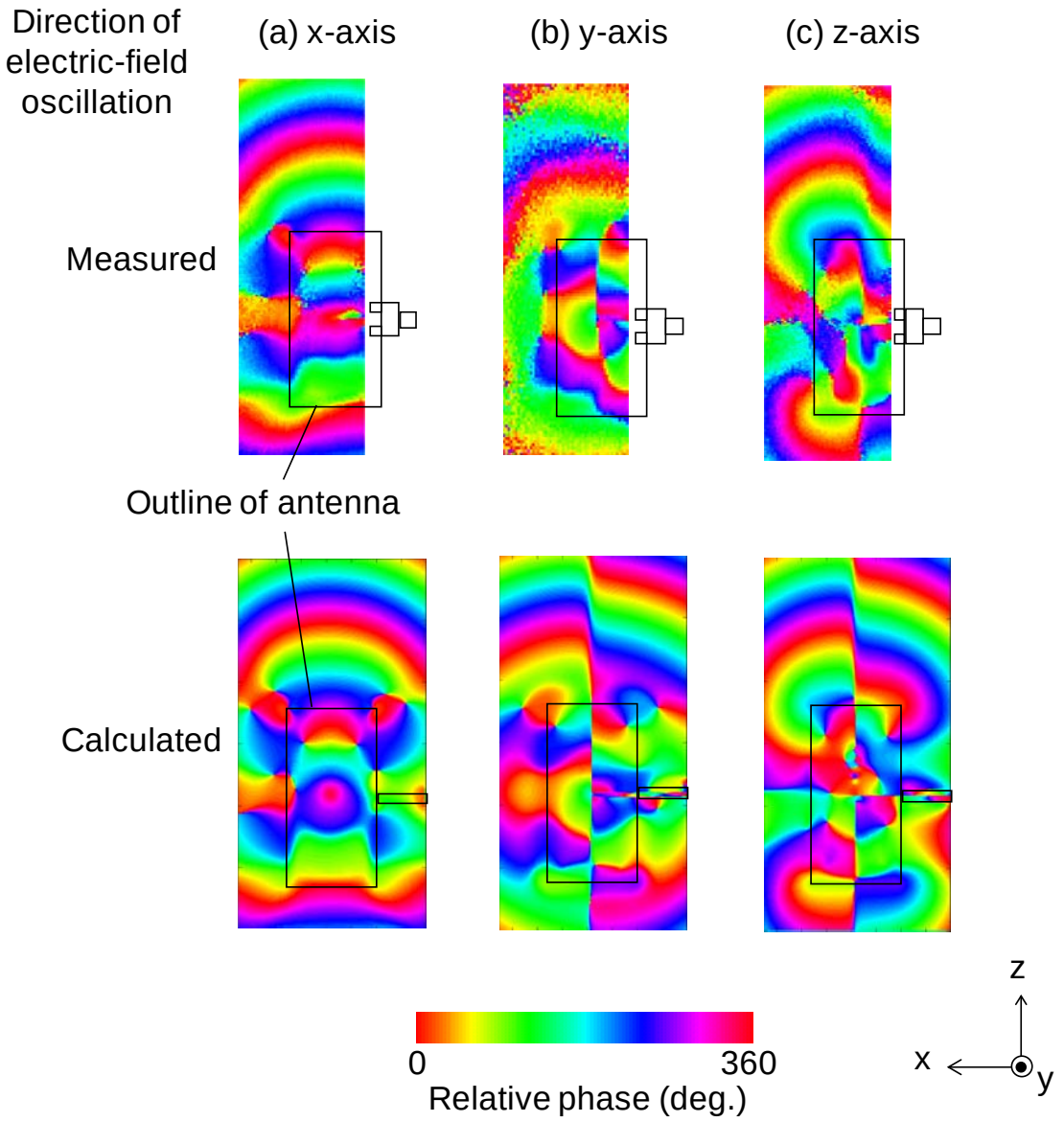

Fig. 5-5. Near-field phase distributions above the planar antenna circuit (a) with E_x, (b) with E_y, and (c) E_z components.

5.2.3 Electric-field vector calculation

The vector spatial field calculated with the electric-field components parallel to the x, y and z-axes is visualized. The vector spatial fields at a certain phase in measured area and in the area outlined by the red line are shown in Fig. 5-6. In the figure, the direction and the size of arrows show the direction and amplitude of the electric-field vector. The electric field curves around a wafer edge into the side of the wafer, which degrades the directivity in the E-plane. The vector spatial field in the yz-plane on the A-A' line is shown in the right side of the figure. The electric field radiates in a direction vertical to the wafer, which degrades the directivity in the H-plane. These results indicate that electric-field vector measurement using the fiber-mounted sensor is useful for intuitively diagnosing the radiation performance when designing antenna circuits.

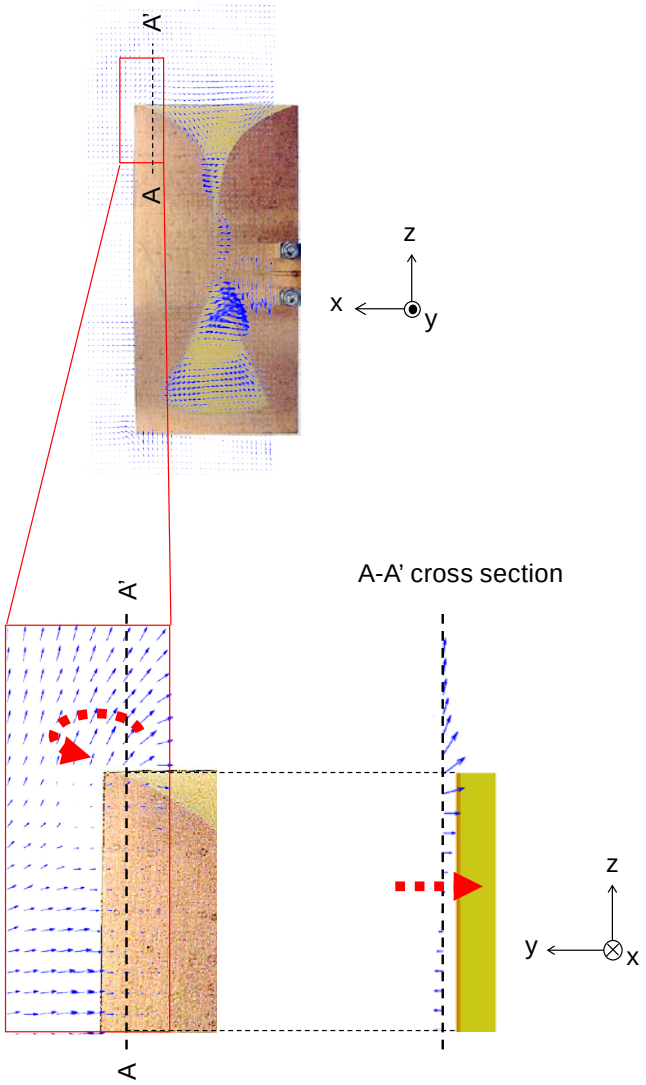

Fig. 5-6. Electric-field vector distribution in xz-plane and cross section on A-A' line in yz-plane.

5.3 Electric-field measurement with DAST-based sensor

5.3.1 SAR measurement system

A block diagram of an electric-field measurement system using the DAST-based sensor is shown in Fig. 5-7. The system consists of a laser source, a polarization control module, the optical electric-field sensor, a receiver (Rx), a 2D scanning stage, and a signal generator (SG). The optical fiber that connects the DAST crystal is inside the glass tube. The diameter and length of the glass tube are 5 and 350 mm. The glass tube is directly attached to a polarization control module with a fiber connector. The laser source emits a linearly polarized light. This is delivered to the sensor through the polarization control module by using a polarization-maintaining fiber (PMF). The delivered light is reflected by the reflector and returned to the receiver with multi-mode fibers (MMF) after it is spilt into two lights, whose polarizations are orthogonal to each other. The received lights are then converted to an electrical signal by balanced photodetectors and a differential amplifier. The signal intensity is proportional to the change in polarization. A measuring instrument such as a lock-in-amplifier, measures the intensity of the obtained electrical signal, which is proportional to that of the applied electric field. For the SAR measurement, the optical sensor is scanned in the tissue-equivalent phantom potted in the acrylic con-tainer whose size is 200 mm x 200 mm x 200 mm regulated in standardized drafts [5.2]-[5.6]. Electric field is radiated from a standardized dipole antenna positioned 5 mm below the container base.

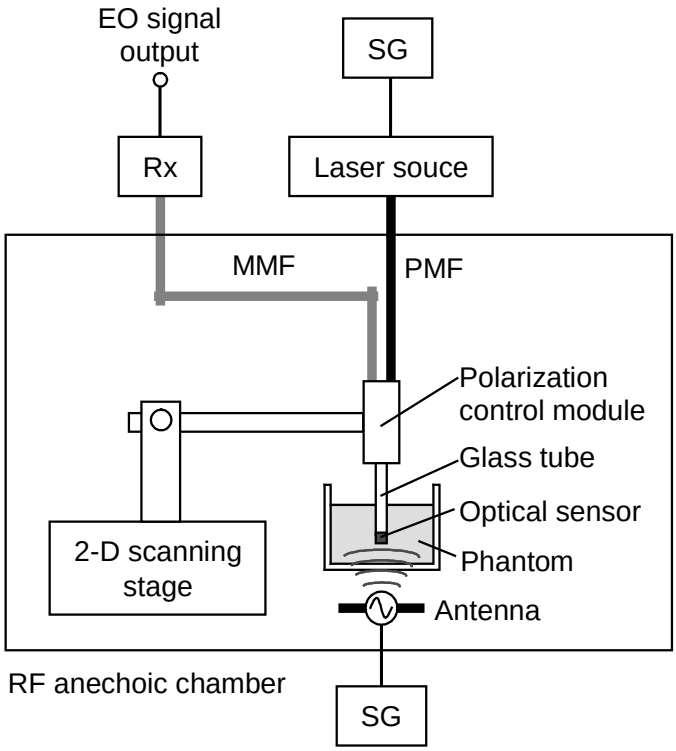

Fig. 5-8. SAR measurement system with DAST-based sensor.

5.3.2 Electric-field mapping in phantom

The DAST-based sensor was scanned in the TEP that was applied to demonstrate the potential of the SAR measurement using our previous CdTe-based sensor [5.7]. The 2D distribution of the electric field parallel to the container base above a dipole antenna and the distribution on the axis parallel to the longitudinal direction of the dipole antenna are respectively shown in Figs. 5-9(a) and (b). The electric field is normalized using the maximum value. In panel (b), the open, closed circles, and solid line represent the electric field measured with the DAST- and CdTe-based sensor, and calculated. The electric field measured with the DAST-based sensor shows good agreement with the calculated one. This demonstrates that the DAST-based sensor can precisely measure the electric field in the phantom with stable sensitivity. The sensitivity of the DAST-based sensor is 2-dB higher than that of the CdTe-based sensor. The difference of the sensitivities in the tissue-equivalent phantom is smaller than that in free space due to the large difference between the permittivity of DAST and the phantom.

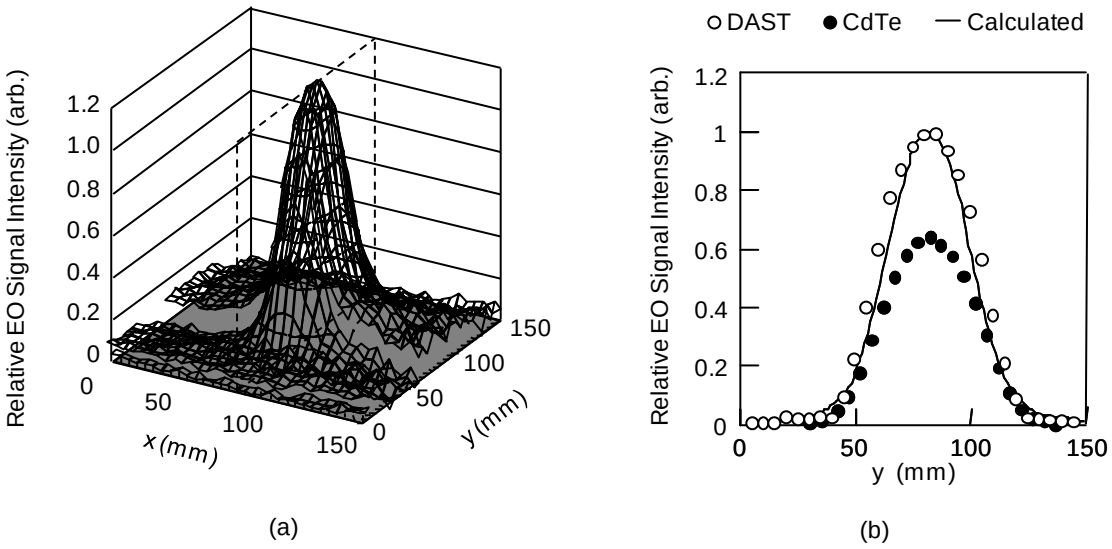

Fig. 5-9. 2D electric-field distribution in the TEP using the DAST-based sensor (a) and electric-field distribution on y-axis along dot line in 2D distribution (b).

5.3.3 ELF-band measurement

We measured the electric field at some points around a commercially available microwave oven that was manufactured in 1995. The electric-field intensities measured at the frequency of 50 Hz are shown in Fig. 5-10(a), where the circles represent the measured points positioned 20 cm from the oven and the electric field calculated from the EO signal intensity is shown be-low each point. The minimum detectable electric field is less than 1 V/m. The electric-field intensity near the

door is larger than that near the power source, and that near the gap of the door is largest. The frequency spectrum of the detectable electric field is less than 1 V/m. The frequency spectrum of the electric field at the position near the gap is shown in Fig. 5-10(b). The frequency spectrum shows that the harmonic compo-nents are from the oven's power source. This result indicates that the DAST-based sensor can specify the precise position of the emitting source and leaks for electromagnetic environment tests in the ELF band.

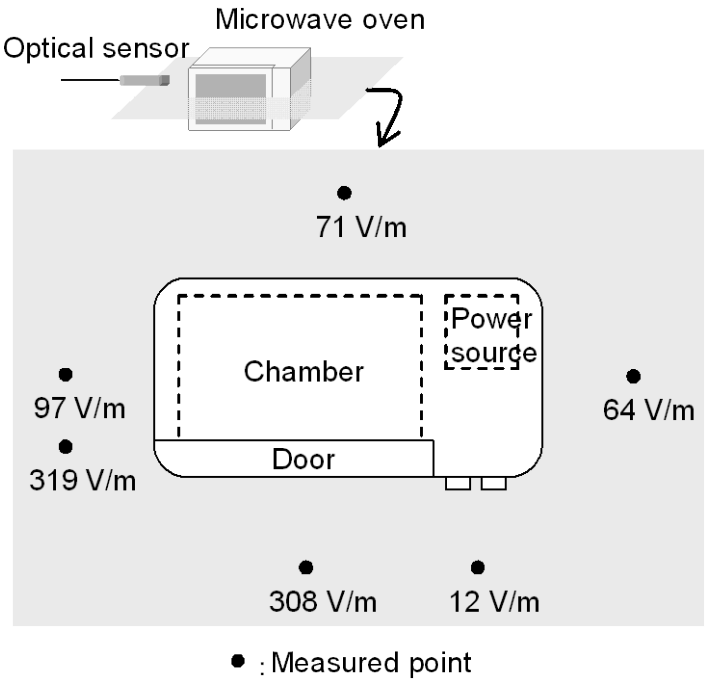

(a)

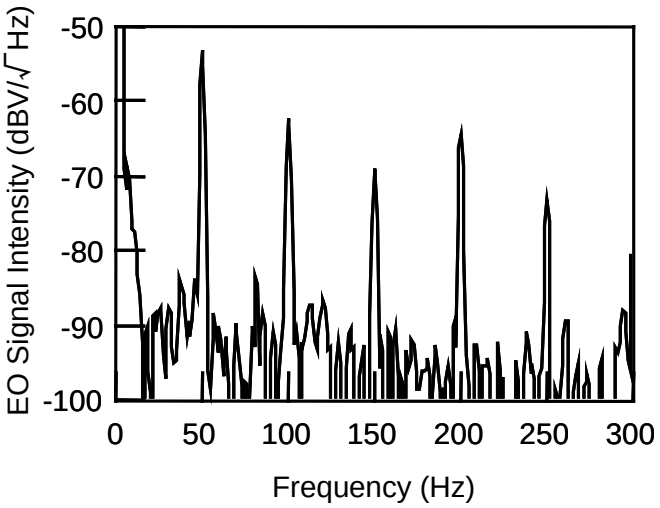

(b)

Fig. 5-10. Measured electric-field distribution around the electric oven at 50 Hz (a) and frequency spectrum near the gap of the door.

5.4 Conclusion

An electric-field vector measurement system employs scanning with a sensitivity-stabilized fiber-mounted sensor based on the PRR method. A combination of the electric fields measured with a longitudinal and transverse-detection probe provides the electric-field vector. The intensity and phase distribution of the electric fields measured on each orthogonal axis represent an asymmetric shape of a planer circuit with a Vivaldi antenna, which cannot be calculated by the simulation with an ideal model. The vector spatial field calculated from the measured electric field shows the electric-field dynamics above and around the planar circuit. Consequently, the visualization of the vector spatial field based on measurements obtained with the fiber-mounted sensor provides intuitive analyses and diagnoses of circuit and antenna performance.

A fiber-mounted sensor containing a 1-cubic-millimeter DAST crystal was applied to SAR measurement for demonstrating its feasibility. Measured electric field agrees very well with calculated one and the sensitivity of the DAST-based sensor is 3-dB higher than that of the previous CdTe-based probe in the TEP, which is different from in a free space. This is because the reflection on the crystal in the TEP is different from that in the free space. This result demonstrates the potential of the DAST-based sensor for reducing the measuring time. Moreover, the DAST-base sensor can precisely measure the electric field at the ELF band, which the CdTe-based sensor does not cover. This result demonstrates that the DAST-based probe is a promising tool for electromagnetic compatibility tests in the ELF band.

References

[5.1] S. Mochizuki, H. Togo, N. Kukutsu, and T. Nagatusma, "High-resolution SAR imaging system using taperd sloted antenna with orthogonally anisotropic directivity," in Asia-Pacific Conference on Applied Electromagnetics 2007, Dec. 2007.

[5.2] Kuster, N.; Balzano, Q.; Lin, J. C.: Mobile communications safety, Telecommunications technology and applications series 4. Chapman & Hall, 1997.

[5.3] EUROPEAN STANDARD EN50961: Basic standard for the measurement of specific absorption rate related to human exposure to electromagnetic fields from mobile phones (300 MHz – 3 GHz). July 2001.

[5.4] IEEE Recommended practice for determining the peak spatial-average specific absorption rate (SAR) in the human head from wireless communications devices: measurement techniques. IEEE Standard (2003), 1528.

[5.5] ARIBE STD-T56: Specific absorption rate (SAR) estimation for cellular. 2.0, Jan.

2002. (in Japanese)

[5.6] IEC 62209-1: Procedure to determine the specific absorption rate (SAR) for hand-held devices used in close proximity to the ear (frequency range of 300 MHz to 3 GHz). Feb. 2005.

[5.7] T. Onishi, H. Togo, N. Shimizu, K. Kiminami, S. Uebayashi, and T. Nagatsuma, “SAR measurement employing electro-optic (EO) probe without using metal,” in A joint meeting BioEM2005, Dublin, Ireland, June 2005.

Chapter 6

Conclusions and Future Vision

6.1 Conclusions

A series of studies on flexibility and sensitivity enhancements of a fiber-mounted sensor were undertaken with respect to ideal electric-field measurements. Key accomplishments were theoretically design techniques based on the optics of crystal and micro-fabrication specified for mounting the crystal on the fiber tip. This dissertation focused on the passive sensitivity stabilization modified for the bulk-EO based sensor and the application of the organic crystal with the highest sensitivity. The major results and findings of this study are as follows:

Chapter 2 described the fiber-mounted sensor that contains no metallic components and with the EO crystal fixed on the tip of an optical fiber that connects the crystal to the optical components to eliminate disturbances, such as those from optical and electrical components, in the near-field range. As a result, electric-field measurements could be performed with little invasiveness. Longitudinal- and transverse-field probes detected electric fields orthogonal to each other. The near-field measurement system has a dynamic range of over 45 dB and can detect an electric field of less than 0.6 V/m. The EO probe has excellent directivity with a cross-axis isolation ratio of over 45 dB. A comparison between the measured and calculated near fields around the dipole antenna confirmed that the probe's invasiveness is negligible. As a result, it is possible to conduct SAR measurements with very little invasiveness. The developed SAR measurement system can detect a SAR of less than 0.5 mW/kg, which satisfies the minimum detection limit stipulated in the regulations. A comparison of the SAR measured with the EO probe and a conventional probe demonstrated that our system is superior to the conventional one in determining the SAR near a container's base. This shows that our proposed system has the potential to be used for determining SAR for the next generation of mobile phones.

Chapter 3 described an electric-field vector measurement system that involves scanning with a sensitivity-stabilized fiber-mounted sensor. In this system, a polarization-rotated reflection method was used to suppress the sensitivity fluctuation caused by fiber bending during scanning, thus enabling large-area measurements. Since the properties (e.g. sensitivity and directivity) of a longitudinal and transverse-detection probe were the same, a combination of the electric fields

measured with each probe provided the electric-field vector. The intensity and phase distribution of the electric fields measured on each orthogonal axis represent an asymmetric shape of a planer circuit with a Vivaldi antenna, which could not be calculated by the simulation with an ideal model. The vector spatial field calculated from the measured electric field showed the electric-field dynamics above and around the planar circuit. Consequently, the visualization of the vector spatial field based on measurements obtained with the fiber-mounted sensor provides intuitive analyses and diagnoses of circuit and antenna performance.

Chapter 4 described a fiber-mounted sensor containing a one-cubic-millimeter DAST crystal developed for improving the sensitivity and detectable bandwidth in the ELF band. The sensitivity is much higher than that of our previous CdTe-based probe, even though CdTe offers the highest sensitivity among inorganic crystals. This means that the measurement time can be greatly decreased. The stability and directivity are good enough for practical SAR measurements. Moreover, the sensitivity is very high in the ELF band, which the CdTe-based sensor does not cover. The results demonstrated that the DAST-based probe is a promising tool for SAR measurements and EMC tests in the ELF band.

Chapter 5 described an electric-field vector measurement system with a sensitivity-stabilized fiber-mounted sensor based on the PRR method. A combination of the electric fields measured with a longitudinal and transverse-detection probe provided the electric-field vector. The intensity and phase distribution of the electric fields measured on each orthogonal axis represent an asymmetric shape of a planer circuit with a Vivaldi antenna, which could not be calculated by simulation with an ideal model. The vector spatial field calculated from the measured electric field shows the electric-field dynamics above and around the planar circuit. Consequently, the visualization of the vector spatial field based on measurements obtained with the fiber-mounted sensor provides intuitive analyses and diagnoses of circuit and antenna performance. A fiber-mounted sensor containing a one-cubic-millimeter DAST crystal was applied to SAR measurement to demonstrate its feasibility. The measured electric field agrees very well with calculated one and the sensitivity of the DAST-based sensor is 3 dB higher than that of the previous CdTe-based probe in the TEP, which is different from the value in a free space. This is because the reflection on the crystal in the TEP is different from that in the free space. This result demonstrated the potential of the DAST-based sensor for reducing the measurement time. Moreover, the DAST-base sensor can precisely measure the electric field in the ELF band, which the CdTe-based sensor does not cover. This result demonstrated that the DAST-based probe is a promising tool for EMC c tests in the ELF band.

6.2 Future vision

This dissertation showed the flexible and highly sensitive fiber-mounted sensor satisfy the requirements for practical electric-field measurements and demonstrated it effectiveness in intuitive antenna characterization and its potential to reduce measuring time. However, some issues still remain in the commercialization of the fiber-mounted sensor. Technical and strategical issues are summarized as follows.

From the technical point of view, further enhancement of sensitivity is the most important issue. In the next generation of mobile telecommunications, the occupied bandwidth and frequency are predicted to broaden and increase for ultrahigh-speed communications. A 3G system will occupy a bandwidth 50 dB broader than the previous 2G system. In this study, the application of the DAST crystal improved the sensitivity 6 dB, but sensitivity enhancement of more than 40 dB is required for full-bandwidth measurement. Since an optical differential detection with a MZI is effective for reducing noise over an occupied frequency range, techniques for stably controlling the MZI will be developed.

The 20-dB sensitivity enhancement with a Faby-Perot interferometer in an EO crystal has been reported. In practical use in enclosed environments, the feedback control of the output power and the wavelength of the input light are necessary to compensate for the sensitivity fluctuation due to temperature changes. The total design for a whole system remains a future issue.

Moreover, for enhancing the sensitivity of the fiber-mounted sensor, a promising material oxide $KTa_{1-x}Nb_xO_3$ (KTN) crystal , whose EO coefficient is 3 dB higher than that of CdTe crystal. However, the dielectric constant of KTN crystal is also larger than that of the CdTe crystal, which means that KTN reflects radio waves as a metal does. To reduce the reflection and induce electric field into the inside of the crystal, a new scheme based metamaterial techniques has to be introduced.

A large-scale array system with at least 10 x 10 sensors is necessary for vastly reducing the measuring cost with the algorithm for estimating two- to three-dimensional-distribution. The whole system designing will be investigated to see whether the polarization controlling techniques for the fiber-mounted sensor and the optical communication techniques can be combined without affecting each other.

The cost reduction of the system is important for viability in the market, but was not considered in this study. The manufacturing process for forming a miniature crystal and the integration process for mounting the crystal and other optical components on a fiber tip should be improved before product release.

From the strategic point of view, the developing schedule and product will be matched with the standardized requirements. The collaboration and corporation with the committee members of standardization groups will be enhanced with frequent communication.

Moreover, the fiber-mounted electric-field sensor developed in this study can be applied to high-power testing and terahertz-wave sensing. The handy sensor has already been investigated for monitoring electric power lines and assessing electromagnetic immunity (EMI) of electric circuit boards. As developments in those applications will be accelerated, the expansion of the market for the optical sensor should yield the cost reduction.

Acknowledgement

I especially thank Associate Professor Naoto Wakatsuki of the University of Tsukuba for his continuing guidance and encouragement. It has been a great honor and a great experience to study under his instruction.

I thank Professor Koichi Mizutani of the University of Tsukuba for his valuable comments and reviews of many of my papers. I also thank Professor Yuichi Ohta, Professor Masahide Itoh and Associate Professor Hiroki Koga for their valuable guidance and many helpful discussions.

I sincerely appreciate the fruitful lectures provided by Professor emeritus Shojiro Nemoto of the University of Tsukuba.

I greatly appreciate the helpful support and encouragement I received from Dr. Yuichi Kado and Dr. Naoya Kukutsu of Nippon Telegraph and Telephone Corporation) for thier helpful discussions on my research.

I am indebted to Professor Tadao Nagatsuma of Osaka University (Formerly of Nippon Telegraph and Telephone Corporation) for his helpful discussion and comments on my research.

I appreciate the valuable discussions and support provided by Dr. Naofumi Shimizu, Dr. Akihiko Hirata, Dr. Aiichiro Sasaki, Dr. Soichi Oka, and Dr. Shoji Mochizuki, who are members of the Smart Devices Laboratory and Microsystem Integration Laboratories, Nippon Telegraph and Telephone Corporation.

I also express my sincere thanks to Dr. Teruo Onishi, Dr. Shinji Uebayashi, Mr. Takanori Iyama, and Mr. Katsuki Kiminami, members of the RF Technology Research Group, Research Laboratories, NTT DoCoMo Inc., for their helpful discussions and cooperation during my research.

I express my heart-felt appreciation to Mr. Pai- Chi Peggy Sah of Agilent Technologies Canada Inc. (formerly of the University of Alberta) and Mr. David Moreno Domingez of the Max Planck Institute of Biochemistry (formerly of the University of Valladolid) for their indispensable cooperation during their international internship program.

I express my deep appreciation to Professor Niels Kuster of the Swiss Federal Institute of

Technology, Dr. Fin Bomholt of Schmid & Partner Engineering AG, Dr. Sze Yun Set, Mr. Kunio Miyaji, Mr. Makoto Tojo, and Mr. Kenji Furuki of Alnair Laboratories Corporation.

I thank helpful comments and discussions to Dr. Takeshi Ogaki, Dr. Kojiro Nishinomiya, Dr. Noboru Ebihara, Mr. Yasushi Kitahara, Mr. Hideto Mitsui, Mr. Tsutomu Fujita, Mr. Takamitsu Kuroyama, members of Acoustic Laboratory in the University of Tsukuba.

I acknowledge all the other people who have contributed to the completion of this dissertation.

At last, I express gratitude to all the members of my family, who have given me encouragement and willingness to study.

Publication list

Papers included in the dissertation

[P-1] **H. Togo** and M. Sato, “A low-temperature lamination technique for assembling polymer-base thermo-capillary optical switch,” Journal of Photopolymer Science and Technology, vol. 11, no. 1, pp. 143-146, 1998.

[P-2] **H. Togo**, A. Sasaki, A. Hirata, and T. Nagatsuma, “Characterization of millimeter-wave antenna using photonic measurement techniques,” International Journal of RF Microwave Computer-aided Engineering, vol. 14, pp. 290-297, 2004.

[P-3] **H. Togo**, N. Shimizu, and T. Nagatusma, “Near-field mapping system using fiber-based electro-optic probe for antenna characterization,” IEICE Trans. Electron., vol.E-90-C, no. 2, pp. 436-442, 2007.

[P-4] **H. Togo**, H. Uchida, H. Yokota, A. Izumi, T. Nagatsuma, and N. Fukasaku, “Highly sensitive optical electric-field sensor using DAST and its applications,” Proceedings of the European Microwave Association Special Issue on Microwave Photonics, vol. 4, no. 4, pp. 294-301, 2008.

[P- 5] **H. Togo**, N. Kukutsu, N. Shimizu, T. Nagatsuma, “Fiber-mounted electro-optic probe with highly stable sensitivity,” Journal of Lightwave Technology & the IEEE Transactions on Microwave Theory and Technique on Microwave Photonics, Vol. 26, No. 15, pp. 2700-2705, 2008.

International conferences

[C-1] **H. Togo**, M. Sato, and F. Shimokawa, “Multi-element thermo-capillary optical switch and sub-nanoliter oil injecton for its fabrication,” in *Proceedings on IEEE International Conference on Micro Electro Mechanical Systems (MEMS'99)*, pp. 418-423, Florida, 1999.

[C-2] T. Nagatsuma, **H. Togo**, K. Narahara, N. Shimizu, and A. Sasaki, “Recent progress in optical measurement of radio-wave signals from gigahertz to terahertz,” in *Proceedings on International Topical Meeting on Microwave Photonics (MWP'04)*, pp. 20-23, Maine, 2004.

[C-3] **H. Togo**, P.-C. P. Sah, N. Shimizu, and T. Nagatsuma, “Gigabit impulse radio link using photonic signal-generation techniques,” in *Proceedings on 35th European Microwave Conference*, Paris, 2005.

[C-4] **H. Togo**, T. Onishi, K. Kiminami, N. Shimizu, T. Nagatsuma, and S. Uebayashi,

"Tip-on-fiber electro-optic probe for specific absorption rate measurement," in *Proceedings on 2006 Asia-Pacific Microwave Photonics* Conference, Kobe, 2006.

[C-5] **H. Togo**, N. Shimizu, T. Nagatsuma, "Fiber-mounted electro-optic probe with highly stable sensitivity," in *Proceedings on IEEE LEOS Annual Meeting 2006*, Vancouver, 2006.

[C-6] **H. Togo**, H. Uchida, H. Yokota, A. Izumi, S. Fukasaku, T. Nagatsuma and N. Fukasaku, "Highly sensitive optical electric-field sensor using DAST," *in Proceedings on 2007 Asia-Pacific Microwave Photonics Conference*, Jeju Island, 2007.

[C-7] S. Mochizuki, **H. Togo**, N. Kukutsu, and T. Nagatsuma, "High-Resolution SAR Imaging System Using Tapered Slot Antenna with Orthogonally Anisotropic Directivity," *Asia-Pacific Conference On Applied Electromagnetics 2007 (APACE2007)*, Melaka, 2007.

[C-8] S. Oka, **H. Togo**, N. Kukutsu, and T. Nagatsuma, "Latest Trends in Millimeter-wave Imaging Technology," in P*roceedings on Progress In Electromagnetics Research Symposium (PIERS) 2008*, Hangzhou, 2008.

[C-9] **H. Togo**, S. Mochizuki, and N. Kukutsu, "Electric-field Vector Measurement with Fiber-mounted Electro-optic Probe," *in Proceedings on The 20th International Zurich Symposium on Electromagnetic Compatibility*, Zurich, 2009.

[C-10] **(Invited) H. Togo**, S. Mochizuki, S. Oka, I. Toyoda, N. Kukutsu, and Y. Kado, "Optical measurement of millimeter-wave antenna for concealed cracks on concrete surace," in *Proceedings on European Conference on Antenna and Propagation (EuCAP) 2010*, Barcelona (2010).

Technical reports

[R-1] **H. Togo**, T. Onishi, K. Kiminami, N. Shimizu, T. Nagatsuma, and S. Uebayashi, "Electric Field Measurement in a Tissue-Equivalent Phantom Using EO Probe," IEICE EMCJ2005-79, pp. 121-126, Sep. 2005 (in Japanese).

[R-2] **H. Togo**, N. Shimizu, and T. Nagatsuma, "Tip-on-fiber Electro-optic Probe for Near-field Measurement," NTT Technical Review, vol.4, no.1, pp. 12-20, 2006.

[R-3] **H. Togo**, S. Mochizuki, and N. Kukutsu, "Optical fiber electric field sensor for antenna measurement," NTT Technical Review, vol.7, no.3, 2009.

Domestic conferences

[S-1] **H. Togo**, A. Hirata, A. Sasaki, T. Nagatsuma, "Gigabit impulse radio transmitter using photonic techniques," in Proceedings of the Society Conference of IEICE 2003, C-14-14, 2003 (in Japanese).

[S-2] T. Onishi, **H. Togo**, N. Shimizu, K. Kiminami, S. Uebayashi, and T. Nagatsuma, "SAR measurement employing small electro-optic (EO) probe without using metal," in Proceedings of IEICE General Conference 2005, C-4-24, 2005.

[S-3] **H. Togo**, T. Onishi, K. Kiminami, N. Shimizu, T. Nagatsuma, and S. Uebayashi, "Electric field measurement in tissue-equivalent liquid using EO probe directly connected with optical fiber," in Proceedings of the IEICE General Conference 2005, C-14-2, 2005 (in Japanese).

[S-4] **H. Togo**, H. Yokota, A. Izumi, S. Kurosawa, N. Fukasaku, H. Uchida, T. Komatsu, T. Takizawa, T. Sugeta, N. Shimizu, and T. Nagatusma, "Electro-optic probe using 4-dimethylamino-N-methyl-4-stilbazolium tosylate (DAST) crystal," in Proceedings of the Society Conference of IEICE 2005, C-14-13, 2005.

[S-5] **H. Togo**, H. Yokota, A. Izumi, S. Kurosawa, N. Fukasaku, H. Uchida, T. Komatsu, T. Takizawa, T. Sugeta, N. Shimizu, and T. Nagatusma, "Measurement of extremely low frequency (ELF) electric field using electro-optic probe comprised of 4-dimethylamino-N-methyl-4-stilbazolium tosylate (DAST) crystal," in Proceedings of the IEICE General Conference 2005, C-14-5, 2005 (in Japanese).

[S-6] **(Invited) H. Togo,** and T. Nagatusma, "Terahertz wave detection techniques using electro-optic effect," n Proceedings of the Society Conference of IEICE 2006, CS-10-5, 2006.

[S-6] **H. Togo**, N. Shimizu, and T. Nagatsuma, "Fiber-mounted electro-optic probe with highly stable sensitivity," in Proceedings of the IEICE General Conference 2007, C-14-10, 2007.

[S-7] (Invited) T. Onishi, **H. Togo**, K. Kiminami, N. Shimizu, T. Nagatsuma, and S. Uebayashi, "SAR measurement employing small electro-optic (EO) probe, " in Proceedings of the IEICE General Conference 2007, CS-10-4, 2007.

[S-8] Y. Fujimoto, **H. Togo**, N, Kukutsu, and T. Nagatsuma, "Sensitivity enhancement in fiber-mounted electro-optic using small dipole antenna," in Proceedings of the IEICE General Conference 2008, C-14-18, 2008.

[S-9] S. Mochizuki, **H. Togo**, N. Kukutsu, and T. Nagatsuma, "Application of highly sensitive SAR to NDT for RC structures," in Proceedings of the IEICE General Conference 2008, B-1-20, 2008.

[S-10] (Invited) S. Oka, S. Mochizuki, **H. Togo**, and N. Kukutsu, "Nondestructive

inspection of concrete structures using millimeter-wave imaging," in Proceedings of the IEICE General Conference 2009, CS-4-2, 2009.